OPTICAL CAVITY-BASED CONTINUOUS-WAVE RAMAN GENERATION

by

Jonathan Tyler Haldiman Green

A dissertation submitted in partial fulfillment of

the requirements for the degree of

Doctor of Philosophy

(Physics)

at the

UNIVERSITY OF WISCONSIN–MADISON

2010

In memory of my mother, Judith Green.

ACKNOWLEDGMENTS

This thesis would not have been possible without the support and friendship of many people here in Madison over the past six years.

I would like to begin by thanking my advisor, Deniz Yavuz, for all of his help and support over the years. I am extremely fortunate that I was able to work in Deniz' research group; it is hard to imagine a better advisor than Deniz. Deniz has an enthusiasm and passion for physics that is inspiring and it has been a joy to have the opportunity to work in his laboratory putting his ideas into practice. He looks past merely getting results in lab and puts a lot of effort into preparing his graduate students to be well-rounded scientists and encourages them to pursue what interests them. He is very approachable and has, very patiently, helped me understand the main ideas described in this thesis; I certainly would not have accomplished much without Deniz' great advice and assistance on all areas of the experiment. I am looking forward to seeing the exciting experiments and results that will come out of the Yavuz labs in the years to come.

I would like to thank Mark Saffman and Thad Walker for introducing me to experimental atomic physics in their quantum computing lab during my first summer here at Wisconsin. I am very grateful that I had the opportunity to work with such a bright and fun group of people. I learned a lot in that short time and was sure that I wanted to continue in atomic physics after that summer.

I would also like to thank Professor Chun Lin and Professor Luke Mawst for being a part of my dissertation committee. I had the opportunity to take an optoelectronics course from Professor Mawst which was one of the most interesting and useful courses I've had here at Wisconsin. This course inspired me to continue taking higher level courses in the Electrical Engineering department, resulting in an ECE minor.

Many thanks to my colleagues Nick Proite, Josh Weber, and Daniel Sikes. Nick was one of the original members of the research group and works in the lab next door to mine. While we have almost always worked on separate projects I feel that the progress in my lab would not have been possible without his help and the many helpful discussions we've had. He is the first person I go to when I'm unsure about anything from some detail in an experimental setup to some fundamental concept in nonlinear optics; our discussions are always very beneficial and enlightening for me. Daniel is the theorist of the group and he was also instrumental in setting up the our Raman scattering lab; he built the seed lasers for our lab and designed the experimental chamber we used in all of our room temperature experiments. Josh is new to the group and very quickly mastering all the details of our experiment. He's played a key role in the progress we've made this year and I regret that we did not have more time to work together; I am confident he will make many improvements to our experiment and push our research much further.

I would also like to thank Todd Johnson for his help during my first few years. Todd is a master of all things electronic and taught me everything I know about feedback circuits. It is hard to imagine getting the experiment to where it is today without Todd's knowledge and assistance.

Thanks to the guys in the instrument shop, most notably Bill Foster, Steve Schumacher, Mike Gerber, and Doug Dummer. Bill was the machinist who machined the cryogenic chamber used in our experiments. Discussions with Bill were very useful when designing the chamber and his hard work and attention to detail were very evident in the final product. I am very grateful to Steve for teaching me how to use the machines in the shop. The ability to make a useful part for our experiment from a piece of scrap metal or stock was extremely useful and also quite enjoyable.

It is difficult to imagine the six years I've had here without my fellow graduate students and happy hour cohorts: Brian Yencho, Mat McCaskey, Ian Lewis, Kyle Caspary, Aongus O'Murchadha, Jake King, Zane Taylor, and David Hover. I know at least one of them will be famous one day (probably not Brian) so I want record their full names as proof that I knew them from the beginning. It has been a lot of fun working through the physics coursework together, teaching together, and going out together. I think it is also reasonable to assert that I am the best darts player of the group and certainly the most gracious winner.

I'd like to thank my family in Washington state for their support. My father, Ben, and step-mother, Carol, have been very supportive of me and my family throughout all of our time here in Madison. They have been frequent visitors and have been a constant source of love and support for me, my wife, and my daughter. I thank my sister, Tirza, and my sister-in-law, Colleen for all the wine, board games, and late night conversations through the years. My friend, Brandon, who is family to me, has been the best friend anyone could ask for over the many years we've known each other. He's always been there for me and has had a large impact on who I am today. I don't think there could be better parents than my dad and my mom, Judy. My father has the most patient and most loving soul that a person could have. He has a perpetual curiosity about the world and the energy to explore it. He has been and always will be my biggest role-model. My mother always seemed to know how to push me without being overbearing and how to demand that I be the best person I could be without ever wanting me to be somebody I am not. She wanted my sister and me to be happy in whatever we chose to do and, once we chose the path for ourselves, she made sure we had everything we needed for the journey. Without the support of my mother, I don't think I would be here finishing graduate school today.

Most of all I'd like to thank the two girls in my life; my wife, Zuzana, and my daughter, Sofie. Six years ago I met Zuzana in a language school in Prague and we've been together ever since. Zuzana has been a source of love and support during my time here and has worked very hard to support our family while I was in the laboratory. Our daughter, Sofie, is almost two years old and is our greatest joy. My girls are the most important part of my life and everything I do and everything I work for is for them.

DISCARD THIS PAGE

TABLE OF CONTENTS

DISCARD THIS PAGE

LIST OF FIGURES

Appendix
Figure   Page

Appendix
Figure   Page

Abstract

OPTICAL CAVITY-BASED CONTINUOUS-WAVE RAMAN GENERATION

Jonathan T. H. Green

Under the supervision of Assistant Professor Deniz D. Yavuz

At the University of Wisconsin-Madison

This thesis explores the theory and design of a continuous-wave molecular modulator. A large amount of research has been devoted to molecular modulation using pulsed lasers and this technique has been used to synthesize the shortest ever optical pulses. The work described in this thesis is our effort to extend molecular modulation into the continuous-wave regime. In order to produce an efficient molecular modulator we must drive the molecules in a gas with two very intense laser beams tuned to a Raman transition; this causes the molecules to coherently oscillate in unison. To achieve the high intensities required for this coherent oscillation, we resonate the two driving fields in a gas-filled high-finesse-cavity.

We demonstrate the highest ever Stokes power (over 300 mW of rotational Stokes light) generated using an optical cavity-based Raman scattering scheme. This thesis describes the design and construction of a liquid nitrogen-cooled high-finesse-cavity which is used to produce the most rotational sidebands ever generated at a pressure over two orders of magnitude lower than any previous cavity-based experiment. Vibrational Raman generation will also be discussed; we used a vibrational transition in deuterium gas to create a 90 THz light modulator, which generated a coherent spectrum of 3 beams spanning from 807 nm to 1.56 μm. With full control over these coherent beams we infer the ability to generate 1.5 cycle pulses.

Chapter 1

Introduction

1.1 Previous Work

Over the past three decades, scientists and researchers have devoted a great deal of effort to the generation of very short optical pulses. The development of the Ti:Sapphire laser [2] and subsequent techniques of compressing Ti:Sapphire pulses [3, 4] has made ultrashort (< 10 fs) optical pulses quite common in research institutions and laboratories. An ultrashort pulse's extremely short pulse duration, small spatial extent ($< 1~\mu$m for a 10 fs pulse), large bandwidth, and it's high intensity make it an extremely useful tool in a wide variety of fields.

If we interpret an ultrashort pulse as a type of camera flash, we can begin to see how such a pulse would be useful. If the duration of a camera flash is longer than the timescale of the motion of the object being imaged, the final image will be blurred; if it is much shorter than that timescale, a very sharp, well-resolved image will be produced. To resolve ever faster processes, faster pulses are required. Processes that take place on the order of the duration of a femtosecond pulse include protein folding, electronic motion, and lattice vibrations [5]. By using ultrashort pulses as "camera flashes" these processes can be investigated and even, as in the case of laser-controlled chemistry [6], controlled.

The broad spectrum of ultrafast lasers is an extremely important tool in time-resolved spectroscopy [5]. In time-resolved spectroscopy, some optical property of a medium is excited with an ultrashort pump pulse and, after some delay τ, a probe pulse propagates through the medium and is subsequently measured. By varying the delay time, τ, one can essentially map out the temporal

response of the medium to an impulse excitation. This can be used to accurately measure electronic relaxation rates, reorientation rates of molecules in materials, and crystal lattice vibrations. Measuring the spectral dispersion of an ultrashort probe pulse through some material sample can also aid in investigating the electronic spectra of atoms and molecules.

Ultrashort pulses are also put to use in materials processing, laser surgery, optical frequency metrology, and communications. Because of the high demand for ever-shorter pulses, many schemes for ultrashort pulse generation have been developed and are currently being explored.

One very effective technique for generating femtosecond pulses is Raman molecular modulation. This technique has actually produced the shortest pulses ever in the optical region of the spectrum [7]. The basis of this technique is to establish coherence between vibrational or rotational states of a molecular ensemble (forcing the molecules to rotate or vibrate in unison) and use this coherence to broaden the spectrum of an input pulse. The broadened spectrum of the pulse allows it to be compressed further in time. This technique was first suggested by Imasaka [8] and Kaplan [9]. Two methods for establishing the molecular coherence required for Raman molecular modulation have been explored: impulsive Raman generation and adiabatic Raman generation.

Impulsive Raman modulation establishes the molecular coherence with a short pulse, the duration of which is shorter than the vibrational or rotational period of the molecule ($<$ 100 fs). Another pulse immediately follows and its spectrum is broadened by the modulation from the coherent molecules. Pulse durations below 4 fs have been achieved through impulsive Raman modulation [10]. This method of ultrashort pulse generation via Raman modulation is ultimately limited by the the low coherence it is able to achieve.

The adiabatic Raman modulation approach establishes molecular coherence by driving the Raman transition with two very intense lasers, termed pump and Stokes, whose frequency difference is that of the vibrational or rotational states of the molecules. The clear place to begin was with pulsed lasers, which readily achieve the intensities needed to generate such a spectrum. Imasaka began by using pulsed lasers and high gas pressures [11] to generate the spectra necessary to produce pulses in the femtosecond regime and Hakuta explored Raman generation in solid hydrogen

[12]. The Harris group at Stanford used Q-switched driving lasers to produce 17 vibrational side-bands spanning from 195 nm to 2.94 μm with low pressure D_2 [13]. Yavuz *et al.* explored a mixture of molecular species and generated over 200 rovibrational sidebands with a D_2 and H_2 mixture [14]. The Harris group was also the first to use this technique to generate single-cycle pulses [7], the shortest optical pulses ever generated, again using Q-switched driving lasers. Recently, Kung has generated a constant carrier envelope phase sub-single-cycle pulse train [15, 16], paving the way for the production of arbitrary optical waveforms.

The following figures show some examples of the spectra the Harris group was able to generate at Stanford. A molecular gas is driven by two copropagating pulses, pump and Stokes. As the pump and Stokes beams propagate through the medium they drive the molecules to vibrate or rotate in unison, diverting pump and Stokes power into frequency sidebands. Figure 1.1 shows the modulated output after being dispersed by a prism. In this figure we see efficient Raman generation from 3 μm to 190 nm using the vibrational transition in D_2 gas [13]. The molecules in these experiments are in a near maximally coherent state, which means, semi-classically, that all the molecules are vibrating in unison and diverting power from the pump and Stokes beams into the broad spectrum shown in 1.1.
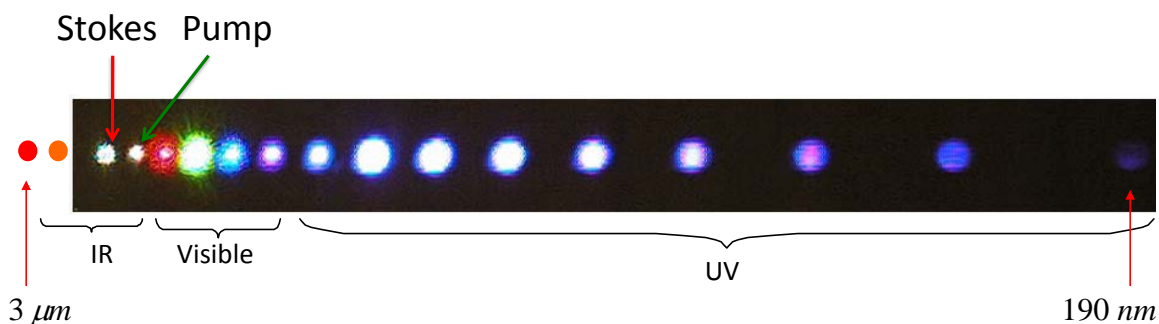
Figure 1.1 Vibrational Raman generation in D_2 gas with pulsed pump and Stokes lasers.

Figure 1.2 shows the spectrum generated by driving a rotational transition in H_2 [17]. The rotational frequency of molecules is significantly lower than the vibrational frequency so the generated frequency sidebands are more closely spaced and span a smaller spectrum than the vibrational system shown in 1.1.
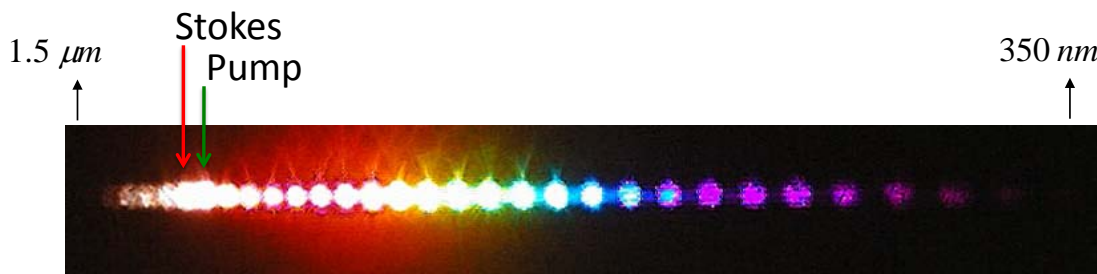
Figure 1.2 Rotational Raman generation in H_2 gas with pulsed pump and Stokes lasers.

The work described above uses pulsed lasers to drive the stimulated Raman scattering process used in ultra-short pulse generation. Following the work of Yavuz [18], we are working to extend the Raman molecular modulation technique to the continuous-wave (CW) regime. Imasaka has been active in this field, developing a high-finesse cavity-based CW molecular-optic modulator using ortho-hydrogen [19]. The principle is to use an optical resonator filled with gas to achieve the intensities required to generate a broad Raman spectrum. Imasaka has also investigated the temporal coherence of CW Raman generated beams [20], and has recently generated three Raman frequency sidebands in a dispersion-compensated high finesse cavity [21].

Calsten is the pioneer of cavity-based Raman generation and developed the first high-finesse cavity-based Raman laser in H_2 [22]. The principle of the Raman laser is to lock a single pump laser to a gas-filled high-finesse cavity which can resonate at both pump and Stokes frequencies. A Stokes beam begins from noise and builds up in the cavity. Using the vibrational transition of H_2, they developed a Raman laser to shift a pump at 532 nm to 683 nm. Their primary motivation for this research was to use stimulated Raman scattering to generate continuous wave radiation in the frequency range 1 - 4 μm. They have also observed anti-Stokes generation on the order of 50 nW in such an optical cavity-based Raman laser scheme [23]. Carlsten's group has done extensive work exploring the theory of cavity-based stimulated Raman scattering. They have explored thermo-optic properties of Raman lasers [24, 25], and investigated the efficiency of cavity-based CW Raman lasers [26, 27]. Repasky and Carlsten have developed a formalism for describing cavity based Raman lasers [28].

While our research focuses on optical cavity-based CW stimulated Raman scattering techniques, another prominent method of stimulated Raman scattering uses a gas-filled hollow-core photonic crystal fiber to generate Raman beams. Benabid and Couny have been active in this area producing very efficient fiber-based pulsed Raman lasers [29, 30] and also fiber-based CW Raman lasers [31]. The focus of their experiments is on very efficient pure rotational Raman generation from a single pump frequency at gas pressures as low as 1 atm. By combining their hollow-core fibers with fiber Bragg gratings they are able to form a cavity within the fiber, lowering the Raman laser threshold to ~ 600 mW of pump power. They have also investigated the coherence of multi-octave fiber-based Raman frequency combs [32] driven by a pulsed pump.

Our work builds on the achievements in cavity-based stimulated Raman scattering and lays the foundation for the development of a molecular modulator capable of modulating an arbitrary optical beam at 90 THz. The usefulness of such a modulator will be described in the following sections.

1.2　Beam modulation

The goal of our research is to produce an efficient, high frequency modulator which can be used to generate ultrashort pulses. Beam modulation is a process through which additional spectral components are added to an input light beam by a medium with a time-varying refractive index. Figure 1.3 shows a basic diagram of this process. When monochromatic light beam with some frequency ω_0 propagates through a medium with a refractive index varying at some modulation frequency, ω_m, power is diverted into frequency components (sidebands) spaced ω_m from the incident beam.

The key requirement for a light modulator is an oscillating index of refraction, $n(t) = n_0 + (\delta n)\sin(\omega_m t)$, where n_0 is the refractive index of the medium with no oscillation and δn corresponds to how strongly the modulator is driven. This index variation can be achieved through many methods. Common modulators include acousto-optic modulators (AOMs) and electro-optic modulators (EOMs).

Acousto-optic modulators use the photoelastic effect to modulate radiation. When sound waves propagate through a crystal lattice, the crystal is periodically strained; this periodic variation in the
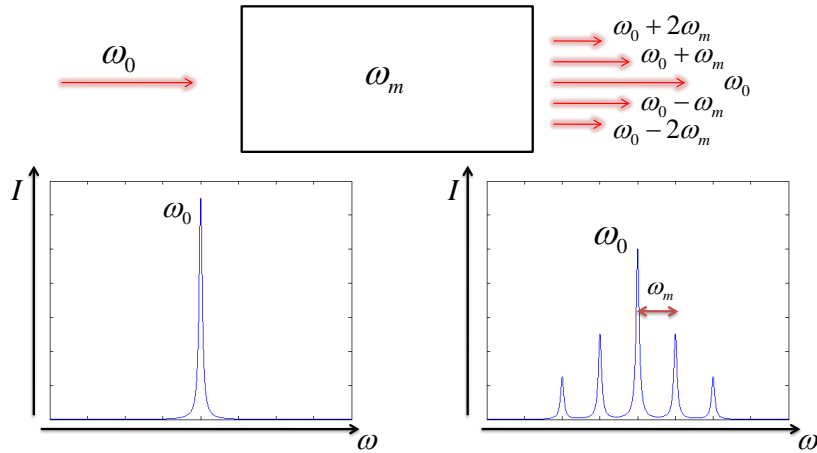
Figure 1.3 General idea of beam modulation.

crystal density produces a periodic variation of the refractive index which, in turn, modulates an input beam. An AOM functions by vibrating a crystal at the modulation frequency with a small transducer. The sound waves from the transducer travel through the crystal and produce a refractive index variation that modulates a beam passing through the crystal. A new beam, shifted by the modulation frequency ω_m is emitted from the crystal, as shown in figure 1.4. AOMs are often used in schemes to shift a laser frequency by frequencies between 10's of MHz and 10's of GHz [33].
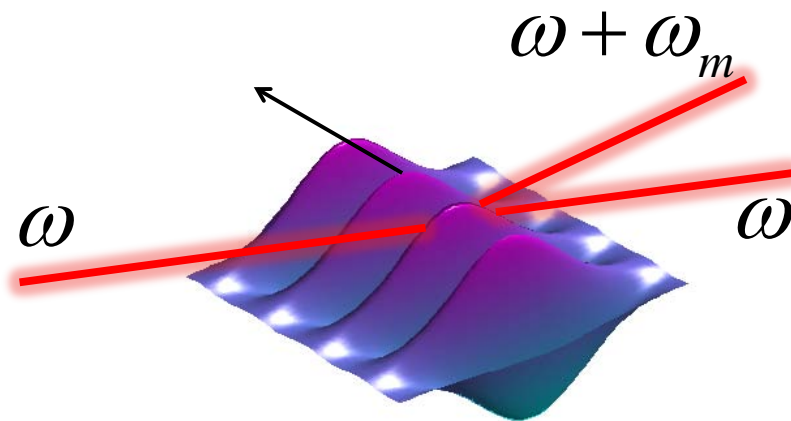
Figure 1.4 Sound waves propagating through the crystal cause periodic density variations that propagate through the crystal. A fraction of the power in the input beam (at frequency ω) is diverted into a new beam with a shifted frequency $\omega + \omega_m$.

EOMs use the electro-optic effect to modulate an input beam. Applying a high voltage to a non-linear crystal such as $LiNbO_3$ or KTP causes a change in the refractive index along one axis of the crystal. By driving a voltage across such a crystal at some frequency ω_m the refractive index is varied at ω_m as well, and the crystal becomes an optical modulator. When the polarization of the beam passing through the crystal is lined up with the crystal axis with the oscillating refractive index, pure frequency sidebands are imparted on the input beam. Unlike the AOM, the frequency shifted sidebands propagate colinearly with the carrier, as shown in figure 1.5. Because it is driven by an electrical signal, the modulation frequency, in this case, is limited by the bandwidth of RF signal generators, amplifiers, and the resonant tank circuit on the crystal. Currently, the best electro-optic modulators achieve modulation frequencies on the order of 100 GHz, while commercially available EOMs operate at frequencies in the 10's of GHz.
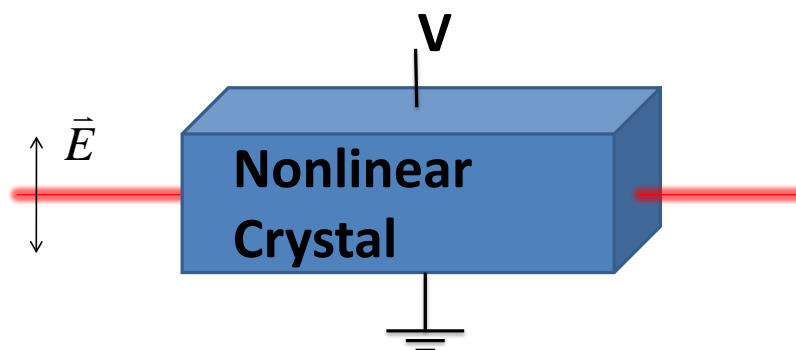
Figure 1.5 An applied sinusoidal voltage across the nonlinear crystal causes a sinusoidal index variation along one axis of the crystal. When the beam polarization is lined up with the variation, it is frequency modulated at the modulation frequency.

1.3   Molecular Modulation

The focus of our research is to use a fundamentally different modulation technique to achieve a modulation frequency of 90 THz. In the scheme, rather than using sound waves or the electro-optic effect, we use the vibration and rotation of the molecules of the medium themselves to achieve refractive index variations. First proposed by Imasaka [8] and Kaplan [9], this type of modulation is referred to as molecular modulation and has been explored by many research groups [34, 10, 35,

15]. Before discussing this system in detail, it is instructive to consider a semi-classical picture of our modulator.
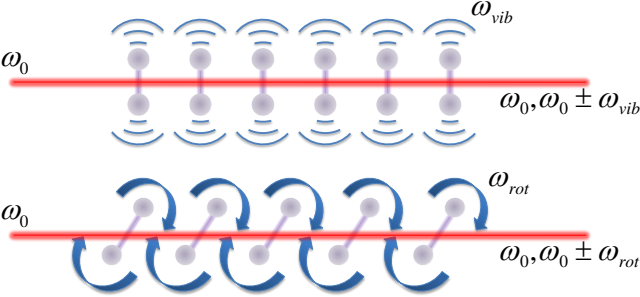
Figure 1.6 Semi-classical depiction of a molecular modulator. The refractive index of the medium varies at the vibrational or rotational frequency of the molecules as they vibrate or rotate in unison.

The key idea of the molecular modulator is to drive the molecules at their natural vibrational or rotational frequency such that they oscillate or rotate in unison (figure 1.6). Looking at the vibrational case specifically, this collective oscillation means that the internuclear separation for all molecules will vary in unison at the oscillation frequency, causing the beam to see refractive index variations at that frequency [36].

An efficient molecular modulator drives the molecules to the point that an appreciable fraction of the population is rotating or vibrating coherently. An ideal modulator consists of all the molecules rotating or vibrating in unison. The molecules are driven by two intense lasers tuned to a Raman transition between vibrational or rotational states of the molecule. The degree to which the molecules vibrate or rotate in unison is given by the coherence between the vibrational or rotational states. The connection between beam modulation and molecular coherence will be discussed in chapter 2.

In D_2 gas, the natural vibrational frequency of the molecules is 90 THz. The benefit of having an efficient 90 THz modulator becomes clear when considering the following example. Let us consider a 90 THz modulator that is efficient enough to impart 1st and 2nd order sidebands on a carrier frequency at $f_0 = 1064$ nm. The output of such a modulator is 5 sinusoidal waves spanning a very broad spectrum. By phase matching the beams (lining up the peaks of each wave at some

point in time) and setting their amplitudes to be equal to one another, we are left with a temporal waveform which consists of a train of very short pulses. In this specific example, we would have a train of half-cycle pulses spaced 11 fs from one another, as shown in figure 1.7. An efficient 90 THz modulator would allow us to synthesize ultrashort pulses from a single monochromatic input beam.
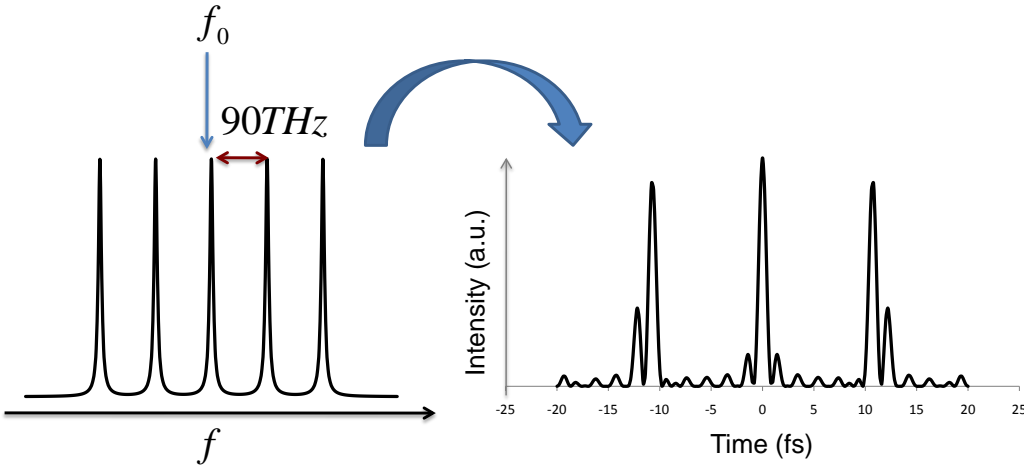
Figure 1.7 Five coherent spectral components spaced by 90 THz are capable of producing ultra-short optical pulses when properly phase-matched.

The work described in this thesis should be interpreted as laying the foundation for such a high speed modulator. By modulating the powerful driving pump beam we have demonstrated that our modulator is capable of generating 1.5 cycle optical pulses. This is the first step in developing the engine for high frequency modulation of an arbitrary input frequency, as shown in figure 1.7.

1.4   Outline

Chapter 2 provides the theoretical foundation for the rest of the thesis. The continuous-wave molecular modulator explored in this thesis is based on driving a Raman transition in deuterium gas with two beams which resonate in a high-finesse cavity. This chapter develops the formalism used to describe stimulated Raman scattering and applies it to an optical cavity-based driving laser scheme. The hope is to motivate the use of an optical cavity as a method of molecular modulation.

Chapter 3 gives a detailed description of the methods used to lock the pump laser to the gas-filled high-finesse cavity. This chapter provides a broad overview of the Pound-Drever-Hall locking technique and the origin of the locking signal. After a general description of the locking scheme, specific considerations in the feedback circuit design and implementation are given.

Chapter 4 details a room temperature rotational Raman experiment using a pump wavelength of 1552 nm and generating up to 300 mW of Stokes power at 1630 nm. It introduces the overall experimental structure which is, for the most part, repeated in subsequent experiments.

Chapter 5 extends room temperature Raman generation to the vibrational states of deuterium. Here, the pump is centered at 1064 nm and the generated vibrational Stokes beam frequency is 90 THz lower, with a wavelength of 1560 nm. The pump and Stokes beams are both resonant with the cavity and the molecular coherence is sufficient to produce an anti-Stokes beam at 807 nm as well. The beams are shown to be coherent and the capability to produce 1.5 cycle pulses is inferred.

Cooling deuterium gas to 77 K with liquid nitrogen significantly improves the Raman generation process we are exploring. Chapter 6 describes the benefits of cooling deuterium gas and outlines the development of, to our knowledge, the first cryogenically cooled high finesse optical resonator. Solutions to obstacles such as condensation, steel deformation, and instabilities introduced by liquid nitrogen boil off are detailed.

Chapter 7 discusses the first experiments with deuterium at 77 K in an optical cavity. We observe the generation of up to 5 rotational Stokes beams and two anti-Stokes beams at pressures as low as .04 atm (measured at room temperature), a pressure over 2 orders of magnitude lower than other cavity-based Raman experiments [22, 37, 21].

Chapter 2

Driven Raman System

The system we work with is a Raman system, shown in figure 2.1. A Raman system can be described as an atomic or molecular system coupling at least two optical fields whose frequency difference is near the transition frequency of low-lying atomic or molecular states. Figure 2.1 show an example of such a system. Dipole transitions between states $|a\rangle$ and $|b\rangle$ can be forbidden, but transitions between the two lower states and the upper electronic states, $|i\rangle$, must be dipole allowed. While the upper levels, $|i\rangle$, are associated with the transition, they are virtually unpopulated because, in the regime we will explore, the detuning, Δ, of the lasers from these $|i\rangle$ states is well outside the linewidth of the transition. In our experiment, for example, the laser frequency is $\sim$ 10 % of the dipole transition frequency itself; a strong non-linear effect is still possible with very intense beams, despite the very large single photon detuning.

Systems that the formalism outlined in this chapter applies to include atomic systems, where the lower states a and b could correspond to hyperfine levels of the same ground state and i are the states in some higher energy orbital to whom dipole transitions are allowed. In a molecular system, the lower levels may correspond to vibrational or rotational states in the ground electronic state of a homonuclear molecule (single photon transitions between rotational or vibrational states in the same electronic state are dipole forbidden in homonuclear molecules); the i states, in this case, would be rovibrational levels in higher energy electronic states.

As mentioned in chapter 1, the goal of our experiments is to drive the molecules in such a way as to, semi-classically speaking, force them to oscillate or rotate in unison. In a quantum mechanical picture, our goal is to build up an appreciable coherence between the states $|a\rangle$ and $|b\rangle$. Our molecular system can be completely described by a 2×2 density matrix ρ.
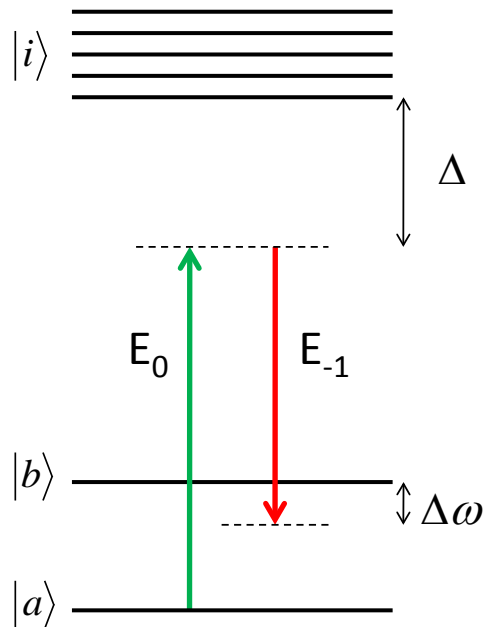
Figure 2.1 Driven Raman system. E_0 is termed the pump beam and E_{-1} is termed the Stokes beam.

$$\rho = \begin{bmatrix} \rho_{aa} & \rho_{ab} \\ \rho_{ab}^* & \rho_{bb} \end{bmatrix} \tag{2.1}$$

The diagonal elements ρ_{aa} and ρ_{bb} give the populations in states a and b, respectively, and the coherence, ρ_{ab}, tells us the degree to which the molecules in the ensemble are in a quantum superposition of states a and b. A maximum coherence of $1/2$ corresponds to all the molecules vibrating or rotating in unison in the semi-classical picture. For sufficiently intense driving laser beams E_0 and E_{-1}, the populations in a and b will equalize and the coherence will approach $1/2$. For clarity, the fields E_0 and E_{-1} will often be referred to as the pump and Stokes beams, respectively. $\Delta\omega$ refers to the two photon detuning of the beams.

To describe beam propagation in a Raman medium we follow closely the formalism developed by Harris and colleagues [38, 34, 14]. The system Hamiltonian which describes the evolution of the molecular states is derived in appendix A and is reproduced in equation 2.2. In the derivation of this Hamiltonian we consider an arbitrary number of beams whose frequency difference is that

of the Raman transition, $\omega_{q+1} - \omega_q = \omega_b - \omega_a - \Delta\omega$. Despite the fact that there are arbitrarily many upper states $|i\rangle$, because the beams are so far detuned from these states, virtually none of the population is transferred to them and we have a two level system described by the following 2×2 matrix.

$$
H_{eff} = -\frac{\hbar}{2} \begin{bmatrix} \sum_q a_q |E_q|^2 & \sum_q b_q E_q E_{q-1}^\star \\ \sum_q b_q^\star E_q^\star E_{q-1} & \sum_q d_q |E_q|^2 - 2\Delta\omega \end{bmatrix}
$$
$$
\equiv -\frac{\hbar}{2} \begin{bmatrix} A & B \\ B^* & D - 2\Delta\omega \end{bmatrix} \tag{2.2}
$$

where a_q, d_q, and b_q, derived in appendix A, determine the coupling between the states of the system and are shown below. Again, $\Delta\omega$ is the two photon detuning. From the effective Hamiltonian shown in 2.2 it is clear that the channel through which the molecules cycle between states a and b depends on the dipole matrix elements with the upper i states; in this way the upper states are critical to the process even though the system Hamiltonian need not describe the evolution of these states.

$$
a_q = \frac{1}{2\hbar^2} \sum_i \left(\frac{|\mu_{ai}|^2}{(\omega_i - \omega_a) - \omega_q} + \frac{|\mu_{ai}|^2}{(\omega_i - \omega_a) + \omega_q} \right)
$$
$$
d_q = \frac{1}{2\hbar^2} \sum_i \left(\frac{|\mu_{bi}|^2}{(\omega_i - \omega_b) - \omega_q} + \frac{|\mu_{bi}|^2}{(\omega_i - \omega_b) + \omega_q} \right)
$$
$$
b_q = \frac{1}{2\hbar^2} \sum_i \left(\frac{\mu_{ai}\mu_{bi}^\star}{(\omega_i - \omega_a) - \omega_q} + \frac{\mu_{ai}\mu_{bi}^\star}{(\omega_i - \omega_b) + \omega_q} \right)
$$

The terms A, D, and B, defined in the matrix 2.2, have a physical interpretation; $A/2$ and $D/2$ are the AC Stark shifts of the states $|a\rangle$ and $|b\rangle$ while B is the frequency of the two-photon drive. In the presence of the light fields, the eigenstates of the system change. To describe the system we find the new eigenstates in the unperturbed eigenvector basis. We find the new eigensystem and take the lower energy state to be smoothly connected to the unperturbed ground state. We know the states are smoothly connected because the characteristic frequency of the molecular system (the

energy level difference) is much faster than the perturbations to the system (which would be on the order of the two photon detuning) [39]. The eigenvector for this lower energy state is

$$|a'\rangle = \left(A - D + 2\Delta\omega + \sqrt{4|B|^2 + (A - D + 2\Delta\omega)} \right) |a\rangle + 2B^* |b\rangle \qquad (2.3)$$

By demanding this fit into a more standard form

$$|\psi\rangle = \cos\left(\frac{\theta}{2}\right) e^{i\frac{\phi}{2}} |a\rangle + \sin\left(\frac{\theta}{2}\right) e^{-i\frac{\phi}{2}} |a\rangle \qquad (2.4)$$

we have the following relations

$$\tan(\theta) = \frac{|B|}{\frac{A}{2} - \frac{D}{2} + \Delta\omega} \qquad (2.5)$$

$$B = |B| e^{i\phi} \qquad (2.6)$$

The terms in the density matrix relate to the coefficients of the new ground state vector as follows $\rho_{aa} = |c_a|^2$, $\rho_{aa} = |c_b|^2$, and $\rho_{ab} = c_a^* c_b$. This gives us a convenient way to related the density matrix elements to the parameters θ and ϕ in equations 2.5 and 2.6. At this point we also account for the lifetime of the metastable state by including the Raman linewidth as a dephasing term in our final expression for the coherence. A Raman linewidth of γ corresponds to a decay rate $\gamma/2$ from the metastable state $|b\rangle$. We will also work in the regime of low coherence, which means $\tan(\theta) \sim \theta$ and yields the following expressions for the density matrix elements.

$$\rho_{aa} = 1 - |\rho_{ab}|^2 \qquad (2.7)$$

$$\rho_{bb} = |\rho_{ab}|^2 \qquad (2.8)$$

$$\rho_{ab} = \frac{B}{A - D + 2\Delta\omega + i\gamma} \qquad (2.9)$$

With these expressions for the density matrix elements, we now have all the parameters needed to model beam propagation through a molecular medium of the type shown in figure 2.1. The propagation equation, 2.10, is derived in appendix A.

$$\nabla_\perp^2 E_q - 2ik\frac{\partial E_q}{\partial z} = -2\hbar N\mu_0\omega^2 \left(a_q\rho_{aa}E_q + d_q\rho_{bb}E_q + b_{q+1}\rho_{ab}^*E_{q+1} + b_q\rho_{ab}E_{q-1}\right) \qquad (2.10)$$

where N is the density of the molecules or atoms. This equation gives a three dimensional description of beam propagation through a Raman medium of an arbitrary number of laser beams with frequencies $\omega_q = \omega_0 + q(\omega_b - \omega_a - \Delta\omega)$ where q is an integer. It assumes field variations in z are much slower than in x and y.

Inspection of equation 2.10 reveals it to be the paraxial equation with a driving nonlinear polarization. It is important to note the coupling of E_q to its neighboring frequency components, E_{q+1} and E_{q-1}. These states are coupled through the coherence, ρ_{ab}, of the molecules. This is the key to molecular modulation and the connection between the coherence of the ensemble and the semi-classical picture of molecules vibrating or rotating in unison. In the quantum formalism, the sidebands are produced through the coherence of the molecules.

2.1 Motivation for cavity-based approach to Raman generation

The key to producing an efficient molecular modulator is driving the molecular coherence, ρ_{ab}, as close to its maximum value of $\rho_{ab} = 1/2$ as possible. To generate coherence on the order of $1/2$, pump and Stokes powers on the order of 1 GW/cm^2 are required. This level of intensity is readily achievable with Q-switched pulsed lasers [13, 35], but the focus of our research is to extend molecular modulation into the continuous-wave regime [18].

The two primary methods for achieving these high intensities and extending molecular modulation into the continuous-wave domain are to use a gas-filled high-finesse cavity [40, 37] and to use a gas-filled hollow core photonic crystal fiber [29, 30, 31]. In our research we choose to investigate optical cavity based Raman generation for reasons described below.

One advantage a cavity-based continuous-wave modulator has over Q-switched schemes is the linewidth of the frequency sidebands. In Q-switched schemes the minimum linewidth of the sidebands is limited by the pulse duration; for typical experiments this pulse duration is roughly 10 ns, giving a minimum sideband frequency linewidth of 100 MHz. If both the pump and Stokes

beams are resonant with a high finesse cavity, however, the generated sideband linewidth will be on the order of the cavity linewidth; in our case this is ~ 10 kHz. The large Q-switched pulse linewidth severely limits their usefulness in such applications as precision spectroscopy.

By forcing emission into modes of the cavity we are assured generated Stokes and anti-Stokes radiation with gaussian spatial profiles, avoiding the conical properties sometimes imparted on the beams by pulsed laser experiments [41] due to phase matching requirements.

Narrow-linewidth, single spatial mode, continuous-wave sidebands could have many uses in precision spectroscopy. If the sidebands are phase matched to produce short pulses, the narrow linewidth of the sidebands allows a train of nearly identical pulses which maintains its structure for the inverse of the linewidth. For our cavity this duration would be roughly 100 μs. In addition to the superior linewidth of the sidebands, the cavity-based approach is not susceptible to the low repetition rate and pulse-to-pulse intensity and timing jitter present in the Q-switched techniques.

While hollow-core photonic crystal fiber methods of stimulated Raman scattering produce large generated Stokes powers, have very high conversion efficiencies, and eliminate the need for a carefully designed cavity locking system, we choose to use a cavity based approach because the generated Stokes beams have a very clean TEM_{00} spatial mode and the linewidth of the generated beams is the linewidth of the high finesse cavity (~ 10 kHz), while, in the hollow-core fiber scheme, this linewidth is Doppler broadened Raman linewidth, which, for vibrational Raman generation, is 530 MHz.

The focus of most previous work with photonic crystal fibers has been on rotational Raman generation. Indeed, by using a narrow photonic transmission band, Benabid and colleagues were able to generate exclusively rotational Raman radiation with no vibrational generation [29]. Such photonic bands and fiber absorption may limit the capability of photonic crystal fiber-based schemes to produce broad Raman spectra.

While there are many advantages to a CW approach to molecular modulation, achieving the required intensities for efficient modulation is much more difficult than with pulsed laser techniques. In order to motivate extending molecular modulation to optical cavity-based setups it is

necessary to show that the intensities which can be achieved within an optical cavity are adequate for producing a large molecular coherence.

In an investigation of the damage threshold of highly-reflective dielectric-coated cavity mirrors, Meng and colleagues achieved intra-cavity intensities of $\sim 100 \text{ MW/cm}^2$ [1] in a high-finesse cavity. These experiments were carried out in a 1.5 cm evacuated cavity, but we can use these intensities as a benchmark for an ideal cavity-based molecular modulator. To evaluate the potential effectiveness of a cavity-based molecular modulator we use the intensities achieved by Meng with our own experimental parameters and numerically integrate the propagation equations.

2.2   Numerical integration of propagation equations

In numerically calculating quantities such as molecular coherence, generated sideband power, or Raman lasing threshold (see section 2.3) we can significantly decrease the processing time by ignoring the transverse spatial variations of the beams. This eliminates the 2-D Laplacian term in equation 2.10. This term describes third-order spatial effects, such as Raman self-focusing [42, 43] which could have an effect on the coupling to the spatial mode of the cavity; for these preliminary calculations these effects will be ignored and, for calculations involving very small coherence, such as finding the Raman lasing threshold, they are negligible.

We assume a homogeneous linewidth equal to the pressure-broadened linewidth [44, 45] and account for Doppler broadening by a convolution integral of the susceptibility and a Gaussian molecular velocity distribution. Equation 2.11 shows the general form of this convolution [46].

$$\chi'(\omega) = \int_{-\infty}^{\infty} \chi(\omega, \omega_a) g(\omega_a, \omega_{a0}) \mathrm{d}\omega_a \tag{2.11}$$

where ω_{a0} is the center frequency of the transition. For a Gaussian Doppler distribution, the function $g(\omega_a, \omega_{a0})$ is given by equation 2.12

$$g(\omega_a, \omega_{a0}) = \sqrt{\frac{4\ln(2)}{\pi\omega_d^2}} \exp\left(-4\ln(2)\left(\frac{\omega_{a0} - \omega_a}{\Delta\omega_d}\right)^2\right) \tag{2.12}$$

where the Doppler linewidth, $\Delta\omega_d$ is given by

$$\Delta\omega_d = \sqrt{\frac{8\ln(2)\kappa T}{mc^2}} w_{a0} \tag{2.13}$$

The frequency dependence of the Raman susceptibility is determined by the density matrix elements, as can be seen in equation 2.10, so each density matrix element is convolved with the Doppler line at each numerical integration step. Figure 2.2 shows the effect of Doppler broadening on the Raman linewidth. Here, the $\nu = 0 \to \nu = 1$ vibrational Raman linewidth is significantly broadened at room temperature and the peak of $\mathrm{Im}\,[\rho_{ab}]$ is reduced significantly; this reduction in the peak coherence corresponds to a reduction in the gain experienced by the Raman sidebands.
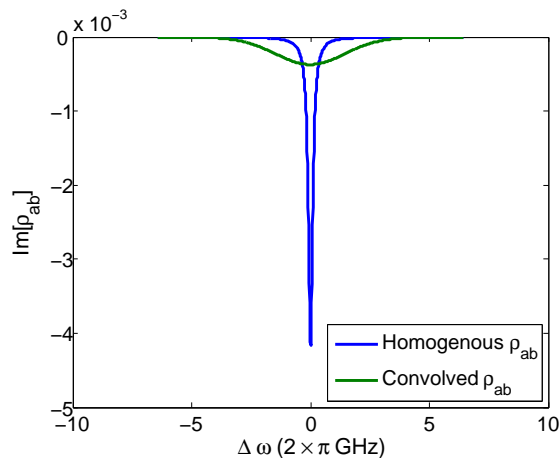
Figure 2.2 Comparison of the homogenous Raman linewidth and the Doppler-broadened linewidth for the $|\nu = 0, J = 0\rangle \to |\nu = 1, J = 0\rangle$ Raman transition in D_2 at room temperature.

The a_q, d_q, and b_q coefficients are calculated using the method outlined in appendix B

We model the single-pass generation of vibrational Stokes sidebands with all the parameters of our cryogenic optical cavity (see chapter 6). The numerical simulations, the results of which are shown in figure 2.3, are meant to motivate the use of an optical cavity to generate Raman sidebands by taking the initial pump and Stokes intensities to be $\sim 100\ \mathrm{MW/cm^2}$ (the peak intra-cavity intensities achieved by Meng) and propagating the fields over the length of the optical cavity. The simulation results, depicted in figure 2.3, assume the molecules, with a pressure of .1 atm at room temperature, are at 77 K and that there is no two-photon detuning. From the simulations it

is clear that we should expect significant Raman generation with intensities that can be achieved in a resonant cavity. It must be emphasized that the effects of the cavity are neglected completely and the steady state generation will be significantly different from the powers shown in figure 2.3; clearly, for an input pump and Stokes power of 30 W each, we cannot generate 17 kW of continuous-wave sideband power. This simulation is meant only to show that the intensities we are able to produce in an optical cavity are sufficient to produce coherence high enough to generate Raman sidebands.
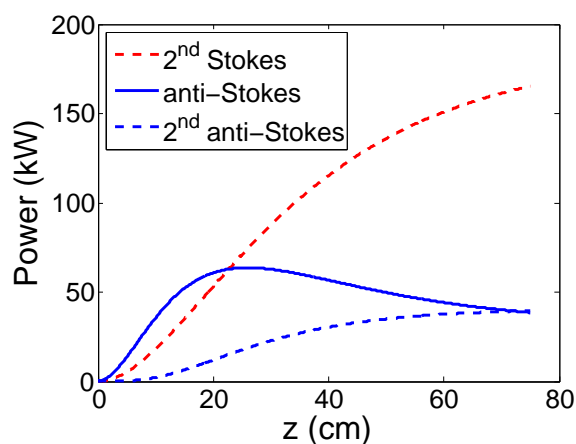
Figure 2.3 Raman sideband generation over the length of the optical cavity using $\sim 100\mathrm{MW/cm^2}$ (achieved by Meng [1]) as the initial pump and Stokes intensities. In these simulations the molecules are at 77 K and there is no two-photon detuning. Stokes beams are have frequencies lower than the pump, while anti-Stokes beams have higher frequencies.

The peak coherence achieved for this system is $\rho_{ab} = .09$. This simulation shows that we can expect to generate appreciable coherence in an optical resonator with reasonable parameters, making an optical-cavity based molecular modulator a viable experimental option.

2.3 Raman laser threshold

By using an optical cavity to generate the high intensities needed for molecular modulation, we put restrictions on the relationship between the pump and Stokes wavelengths. For both the pump and Stokes to have high intensities they must each have a frequency that resonates with the

cavity and a frequency difference close to the Raman transition frequency. In our experiments we lock just one pump laser beam to the cavity and a Stokes photon is radiated from noise. Stokes photons emitted into a cavity mode that are close to, or within, the Raman transition linewidth will then lase (see figure 2.4). The cavity lines shown in figure 2.4 are typically much narrower than the Raman linewidth, although the free spectral range of the cavity (the spacing between the cavity lines in the figure) is not necessarily smaller. We have the freedom to tune the two photon detuning across the Raman resonance, allowing us to maximize the Stokes generation.
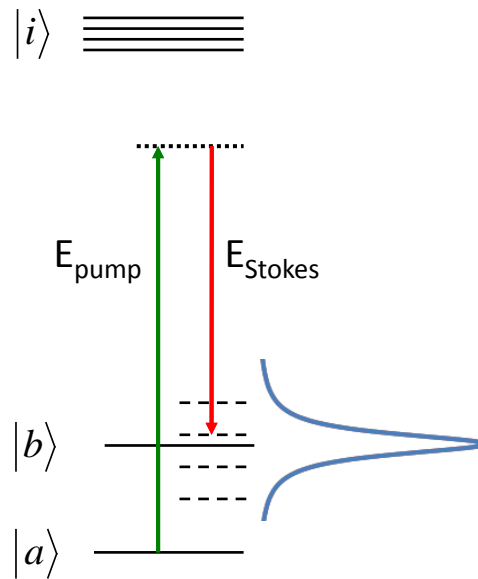
Figure 2.4 The Raman linewidth acts as the gain profile for the Stokes beams. The dashed lines indicate cavity modes. The Stokes beam emitted into the cavity mode closest to the Raman gain peak will tend to lase.

Using the propagation equation (equation 2.10) and, for computational simplicity, dropping the transverse field terms, we can estimate what pump powers are required to reach the lasing threshold. Treating this as a one dimensional problem and only focusing on the term that describes the amplification of the Stokes beam due to a strong pump we can use equation 2.14 to describe the gain experienced by the Stokes beam.

$$\frac{\partial E_s}{\partial z} = -i\eta\hbar\omega_s N b_p \rho_{ab}^* E_p \tag{2.14}$$

Near the lasing threshold it is reasonable to assume that the pump beam is not depleted and that the coherence, ρ_{ab}, is small. Making these assumptions we have

$$\begin{aligned}\frac{\partial E_s}{\partial z} &= -i\frac{\eta\hbar\omega_s N b_p^2}{2}\frac{|E_p|^2}{A/2 - D/2 + \Delta\omega - i\gamma/2}E_s \\ &\equiv -iXE_s\end{aligned} \tag{2.15}$$

By assuming constant pump power, equation 2.16 has a very simple exponential solution. In equation 2.14, γ is the homogeneous linewidth of the molecules; we must also consider effects of Doppler broadening. To find the Doppler-broadened lineshape of the transition we must convolve the homogenous susceptibility of the medium with the Gaussian molecular velocity distribution, as in section 2.2.

After accounting for the Doppler-broadening of the Raman linewidth, we can find the round-trip gain on the Stokes beam and compare that to the losses in the cavity. We consider only the mirror transmissivity at the Stokes wavelength and the scattering and absorptive losses of the mirrors for this calculation. The round-trip power gain, G_{rt}, in a cavity with length L and mirrors with a reflectivity R is given by equation 2.16

$$G_{rt} = RR\mathrm{e}^{2\mathfrak{Im}(X')(2L)} \tag{2.16}$$

which gives a threshold condition of

$$\mathfrak{Im}\left[X'\right](2L) = \ln\left(\frac{1}{R}\right) \tag{2.17}$$

Using this equation, we can calculate an estimate for the lasing threshold of a vibrational Stokes beam on the $|\nu = 0, J = 0\rangle \rightarrow |\nu = 1, J = 0\rangle$ transition in D_2 gas. This calculation uses all the experimental parameters (cavity length, mirror properties, temperature, etc) described in chapter 5. It also assumes a two photon detuning, $\Delta\omega$, of zero, a pressure of 0.1 atm, and takes into account the

statistical distribution of molecules across the lower rotational states. Assuming a mirror transmissivity of 38 ppm and mirror scattering/absorption of 100 ppm at the vibrational Stokes wavelength we find the laser threshold to occur when 9 mW of pump power is transmitted through the cavity, corresponding to a peak intra-cavity pump intensity of $248 \, \mathrm{kW/cm^2}$. Increasing the pressure to 0.5 atm reduces this threshold to 2.1 mW of pump power transmitted through the cavity, corresponding to a peak intensity of $57 \, \mathrm{kW/cm^2}$. Referring to figure 5.5, this estimate proves to be on the same order of magnitude, but significantly less than the experimental threshold we observe. The most probable sources of discrepancy between the measured threshold and that calculated above are 1) imperfect overlap of the cavity mode with the peak of the Raman linewidth, 2) differences between the reflectivities of each individual cavity mirror and small frequency dependent variations in the reflectivity, and 3) degradation of the cavity coupling due to thermal focusing effects.

Chapter 3

Cavity Locking

As described in chapter 2, very large pump and Stokes intensities are required to generate any appreciable coherence between vibrational or rotational states of the molecular ensemble. To achieve these intensities in the continuous-wave domain we use a resonant cavity. Our cavity has a frequency linewidth on the order of 10 kHz, which means that in order for a laser beam to remain resonant with the cavity, the cavity length and wavelength of the light must match to within 10^{-10} m, which is on the order of the width of an atom, on average. Thermal drifts, the smallest of vibrations, and the variations in wavelength from the laser diode itself clearly make this impossible without the careful design of an active feedback system.

To maintain resonance with the cavity we use the Pound-Drever-Hall locking technique [47, 48]. In our scheme, feedback is split into two branches. Feedback is sent to the laser diode itself to compensate for "fast" variations in the laser wavelength and narrow the linewidth of the laser. A signal is also sent to the cavity (or laser) piezo to correct for "slow" variations from mechanical vibrations or thermal effects.

In this chapter we give a detailed description of the feedback system we use to maintain very high intra-cavity intensities.

3.1   Origin of the error signal

The key to the Pound-Drever-Hall locking technique is the generation of the error signal used to lock the laser to the cavity. This error signal is produced by modulating the frequency of the input beam and detecting the signal reflected from the optical cavity. The error signal is generated
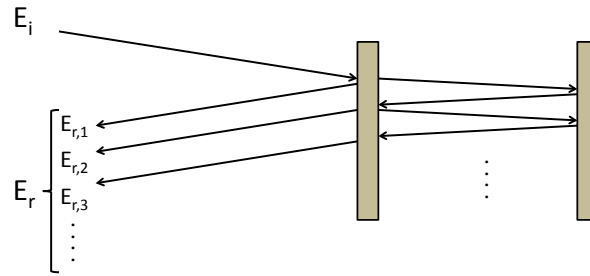
Figure 3.1 The total reflected wave from the cavity is a combination of waves which are leaked from the cavity after a number of round trips through the cavity.

from interference between the frequency sidebands on the laser and the multiple components that make up the total reflected wave from the cavity. Figure 3.1 shows the total reflected wave, E_r, from a simple optical resonator is a combination of the reflection of the incident beam, E_i, from the surface of the mirror and the waves leaked from the cavity after subsequent round trips. If the mirrors are lossless with a reflectivity r, an amplitude transmission coefficient of t, and are spaced a distance l from one another, the reflected field for an incident field with angular frequency ω is

$$E_r = \left[r + ttr\mathrm{e}^{-i\delta}(1 + r^2\mathrm{e}^{-i\delta} + r^4\mathrm{e}^{-i2\delta} + \cdots) \right] E_i \tag{3.1}$$

where $\delta = \frac{2\omega l}{c}$ [49]. Here we take mirrors to have the same reflectivity regardless of the direction of propagation of the incident field. Equation 3.1 is a geometric series which can be expressed as follows

$$
\begin{aligned}
E_r &= \frac{\left(1 - \mathrm{e}^{-i\delta}\right)\sqrt{R}}{1 - R\mathrm{e}^{-i\delta}} E_i \\
E_r &= F(\omega) E_i
\end{aligned}
\tag{3.2}
$$

where $R = r^2$.

To see the effect of beam modulation on the reflected field we define the incident and reflected fields as follows.

$$E_i = E_0 \mathrm{e}^{i\omega t}$$

$$E_r = E_1 \mathrm{e}^{i\omega t}$$

Modulation of the input beam at some frequency Ω and amplitude β gives

$$E_i = E_0 e^{i(\omega t + \beta \sin(\Omega t))} \tag{3.3}$$

Using the Jacobi-Anger expansion (eq. 3.4) we can express the modulated input beam in terms of Bessel functions.

$$e^{iz\sin(\theta)} = J_0(z) + 2 \sum_{n=1}^{\infty} i^n J_n(z) \cos(n\theta) \tag{3.4}$$

In practice the input beam is modulated such that only the first frequency sideband need be considered as the others have negligible power. Using 3.4 and throwing out terms that correspond to higher order frequency sidebands we have

$$
\begin{aligned}
E_i &= E_0 e^{i\omega t} \left[J_0(\beta) + 2i J_1(\beta) \sin(\Omega t) \right] \\
&= E_0 \left[J_0(\beta) e^{i\omega t} + J_1(\beta) e^{i(\omega + \Omega)t} - J_1(\beta) e^{i(\omega - \Omega)t} \right]
\end{aligned} \tag{3.5}
$$

Taking this as the incident beam we can now find an expression for the reflected power from the cavity $P_r = E_r^* E_r$

$$
\begin{aligned}
P_r &= E_r^* E_r \\
&= |E_0|^2 J_0^2(\beta) |F(\omega)|^2 + |E_0|^2 J_1^2(\beta) \left[|F(\omega + \Omega)|^2 + |F(\omega + \Omega)|^2 \right] \\
&+ \left[F(\omega) F^*(\omega + \Omega) J_0(\beta) J_1(\beta) - F(\omega - \Omega) F^*(\omega) J_1(\beta) J_0(\beta) \right] e^{-i\Omega t} |E_0|^2 \\
&+ \left[F^*(\omega) F(\omega + \Omega) J_0(\beta) J_1(\beta) - F^*(\omega - \Omega) F(\omega) J_1(\beta) J_0(\beta) \right] e^{i\Omega t} |E_0|^2 \\
&+ \mathcal{O}(2\Omega)
\end{aligned} \tag{3.6}
$$

The power of the reflected beam is necessarily a real quantity. This means that the product of the real and imaginary components of the exponential terms and their coefficients in equation 3.6 must be purely real. Throwing out terms oscillating at 2Ω this gives the following expression which matches real and imaginary terms to give a real result.

$$
\begin{aligned}
P_r &= E_r^* E_r \\
&= |E_0|^2\, J_0^2(\beta)\, |F(\omega)|^2 + |E_0|^2\, J_1^2(\beta)\, \big[|F(\omega+\Omega)|^2 + |F(\omega-\Omega)|^2\big] \\
&\quad - 2\sqrt{|E_0|^4\, J_0^2(\beta)J_1^2(\beta)}\, \big[\mathfrak{Re}\,(F(\omega)F^*(\omega+\Omega) - F^*(\omega)F(\omega-\Omega))\cos(\Omega t) \\
&\quad + \mathfrak{Im}\,(F(\omega)F^*(\omega+\Omega) - F^*(\omega)F(\omega-\Omega))\sin(\Omega t)\big]
\end{aligned}
\tag{3.7}
$$

Equation 3.7 shows that the reflected signal is made up of a non-time-varying signal and a signal oscillating at the modulation frequency Ω; the error signal is in the oscillating component of the reflected signal. In our case, the finesse of the cavity is sufficiently high that the cavity linewidth is much narrower than the modulation frequency. This means that the carrier and sidebands cannot both be resonant with the cavity. If this is the case, then when the carrier is nearly resonant with the cavity $F(\omega \pm \Omega) \approx -1$ and

$$
F(\omega)F^*(\omega+\Omega) - F^*(\omega)F(\omega-\Omega) \rightarrow F^*(\omega) - F(\omega) = -2i\,\mathfrak{Im}(F(\omega))
\tag{3.8}
$$

Because $F(\omega)F^*(\omega+\Omega) - F^*(\omega)F(\omega-\Omega)$ becomes purely imaginary, the cosine term in 3.7 can be neglected and the reflected signal is given by

$$
P_{ref} \approx 2P_s - 4\sqrt{P_c P_s}\,\mathfrak{Im}(F(\omega))\sin(\Omega t)
\tag{3.9}
$$

where

$$
P_c = |E_0|^2\, J_0^2(\beta)
$$

$$
P_s = |E_0|^2\, J_1^2(\beta)
$$

are the powers in the carrier and sidebands. The error signal is the amplitude of the reflected power component oscillating at the modulation frequency Ω. Figure 3.2 shows the amplitude of this term $(\mathfrak{Im}(F(\omega)))$ as a function of $\delta = \frac{2\omega l}{c}$.

Figure 3.2 shows that, near the cavity resonance, the error signal varies linearly with frequency deviations from the cavity resonance $(\delta\omega)$. This linearity is very important because it allows us to
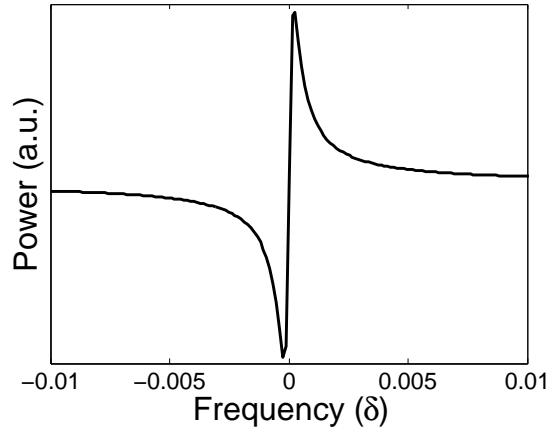
Figure 3.2 Error signal near cavity resonance for cavity with linewidth much smaller than the modulation frequency ($\sim \mathfrak{Im}(F(\omega))$). If the deviation of the laser frequency from the cavity resonant frequency is within the cavity's frequency linewidth the error signal is linear, allowing us to use conventional feedback and control techniques to lock to the cavity.

use standard techniques of feedback and control to control the system. The linear approximation is good as long as $\delta\omega \ll \delta\nu$ where $\delta\nu$ is the linewidth of the cavity. In this linear regime the error signal is given by

$$\epsilon = -\frac{8\sqrt{P_c P_s}}{\delta\nu}\delta f \tag{3.10}$$

where δf is the deviation of the real frequency of the laser from the cavity resonance.

3.2   Implementation

This section discusses how the error signal described in section 3.1 is actually used for locking and covers most of the important considerations when designing the system.

3.2.1   Details of the optical cavity

The cavity used in our experiment consists of ultra-low loss, highly-reflective dielectric coated mirrors. The measured transmittance through these mirrors at the resonant wavelengths is on the order of 50 parts per million (ppm) and scattering and absorptive losses are on the order of 100

ppm, as quoted by the manufacturer; this gives a mirror reflectivity, R, of $\sim 99.98\%$. With this reflectivity, the finesse can be calculated (using eq. 3.11) to be 15,700.

$$\mathcal{F} = \frac{\pi\sqrt{R}}{1 - R} \tag{3.11}$$

The frequency linewidth, $\Delta\nu_{1/2}$, of the cavity depends on the cavity length, l, as well as the reflectivity of the mirrors [46]. We have used two different cavity lengths in our experiments, 75 cm and 27 cm. Using equation 3.12 we find the cavity linewidth to be ~ 13 kHz for a 75 cm cavity and ~ 38 kHz for a 27 cm cavity.

$$\Delta\nu_{1/2} = \frac{c}{2\mathcal{F}l} \tag{3.12}$$

In our 27 cm cavity experiments, we work with mirrors with a radius of curvature of 50 cm. Because the cavity length is sub-confocal, we are able to discriminate between spatial modes of the cavity and couple light exclusively into the TEM_{00} mode. For our 75 cm cavity length, we use mirrors with a radius of curvature of 100 cm. Theoretically, mirrors with $R = 50$ cm should form a stable resonator for this cavity length; in fact this would be preferable in our experiment because the beam waist inside the cavity, for 1064 nm light, would be ~ 240 μm, rather than ~ 400 μm for the 100 cm mirrors, giving us higher peak beam intensities. In an effort to empirically mode-match the beam we remove the experimental chamber and place one extra cavity mirror on the table in the location of the input mirror of the experimental cavity. We measure the beam profile transmitted through the mirror as a function of distance from the mirror and make adjustments to the input beam to try to match the location and size of the theoretical cavity waist. Unfortunately, we were unsuccessful in our efforts to couple to the 75 cm cavity with mirrors of $R = 50$ cm. We then replaced the $R = 50$ cm mirrors with $R = 100$ cm mirrors, followed the same procedure for mode matching and were easily able to couple the light to the cavity. The intra-cavity beam waist is increased for this choice of mirrors, reducing our peak attainable intensity, but we benefit greatly from the ease of coupling and resonator stability.

3.2.2 Producing the error signal

A basic schematic for our locking scheme is shown in figure 3.3. The focus of this diagram is on the RF electronics used to manipulate the error signal and create a useable feedback signal, so many of the optics details (such as fiber amplifiers and measurement schemes) are omitted.
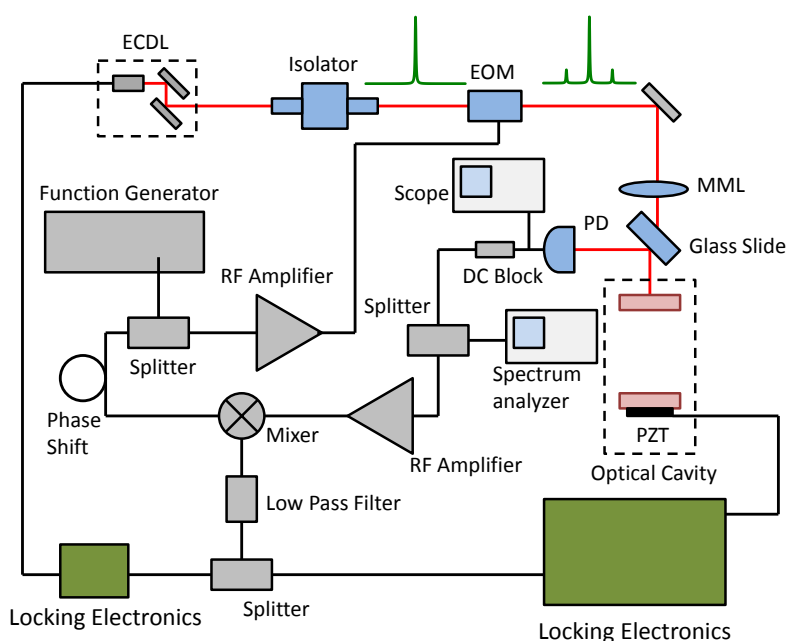
Figure 3.3 Basic schematic for our Pound-Drever-Hall locking scheme

In order to perfectly lock a laser to an optical cavity the laser linewidth must be the same as the cavity linewidth. For this reason it is important to begin with a stable laser with as narrow a linewidth as possible. We begin with an inexpensive AR coated laser diode which we temperature tune to be centered at the desired wavelength. We use a diffraction grating-based external cavity to narrow the free running diode laser linewidth and tune the frequency [50, 51]. The linewidth of our external cavity diode laser (ECDL) is ~ 500 kHz. As stated in section 3.2.1, our cavity linewidth is on the order of 10 kHz, so, in order to effectively couple to the optical cavity, we will need to actively narrow the linewidth of the laser further still, as we will see in section 3.2.5.

When the light is mode-matched to the optical cavity, the full power of the beam is reflected directly back on itself, except for when the beam is resonant with the cavity. In experiments

where circularly polarized light is used we are able to divert most of this back reflection with a combination of a $\lambda/4$ plate and a beam cube. In our experiments which require linear polarization, we must use a Faraday isolator to prevent back reflections from damaging the fiber amplifier. Even in low power Pound-Drever-Hall setups, where there is no danger of damage, back reflections that reach the laser diode are detrimental to the stability of the laser; isolation is a very important consideration in cavity locking.

As we discussed in section 3.1, the error signal is produced through the interference of frequency sidebands on the carrier as the input beam is reflected from the optical cavity. The first step to locking the cavity is to impart these sidebands on a carrier beam. We choose to use an electro-optic modulator (EOM) for this task. In all our experiments the modulation frequency (Ω) is in the 10's of MHz, well outside the response time of the cavity. In our earlier experiments we used $LiNbO_3$-based modulators. These modulators were unsatisfactory because the amount of residual amplitude modulation (AM) on the beam was strongly coupled to the temperature of the crystal. Our locking electronics are susceptible to problems stemming from slow AM drifts so this drift proves to be problematic. Our current experimental setup uses KDP as the nonlinear crystal. In addition to having a higher optical damage threshold, this crystal has proven to be much more reliable and more resistant to thermal noise.

After frequency sidebands are imparted on the laser, it is mode-matched to the cavity with a mode-matching lens (MML). The procedure we use to ensure our beam matches the theoretical cavity mode is described in section 3.2.1. The reflected signal is picked off either with a glass slide or a beam cube. As described in section 3.1, the error signal is contained in the reflected signal, but it is at the modulation frequency, Ω; in order to produce a useable signal we must use RF electronics to mix the signal down to DC. The first step in this procedure is to use a DC block after the photodiode to filter out the unimportant DC components of the reflected signal. After this filter, only the component at the frequency Ω survives. This signal is then mixed with the properly phase-adjusted RF signal that drives the EOM. The ouput of the frequency mixer has components at DC and at 2Ω. A low pass filter blocks the 2Ω component and what remains is the locking signal. As mentioned before, for a cavity of our finesse, we must narrow the laser linewidth in addition to

controlling the cavity length to maintain resonance. For this reason the error signal is split and sent to a high-speed feedback circuit (which feeds back to the diode) and a low-speed feedback circuit (which controls the cavity or laser piezo).

Before discussing the feedback branches in more detail, it is worthwhile to discuss some of the details of the RF filtering system. One component which is helpful, although not fundamentally necessary, is an RF amplifier immediately after the DC block on the photodiode. The RF mixer used in our setup operates most efficiently when the RF input is close to the local oscillator (LO) power, which, for our mixer, should be +7dBm. The component of the reflected signal oscillating at Ω is well below this power, so a +20 dB amplifier on this signal can help improve the signal from the mixer and the overall error signal.

One other important detail of the mixing process is making sure the LO phase matches with the error signal input such that mixer produces the appropriate error signal. Figure 3.4 shows the simulated output DC signal for different LO phases. In these plots, features at the carrier and sideband frequencies are clearly visible. Phase lags of $\pi/2$ and $3\pi/2$ produce a pronounced feature at the carrier wavelength which can be used for locking. It is important to note that only one of the $\pi/2$ and $3\pi/2$ error signals can be used as they are reflections of one another (see figure 3.4). One of the error signals will tend to lock the carrier and the other will prevent the carrier from being resonant with the cavity and tend to lock the sidebands. By scanning one of the cavity mirrors with the piezo and measuring the output of the RF electronics we can see the shape of the error signal; we adjust the phase of the LO until the error signal we measure has the proper shape.

The method for adjusting the LO phase is quite simple. LO phase adjustments are performed simply by adding or subtracting lengths of cable between the RF source and the mixer. For a modulation frequency 50 MHz, one wavelength in electrical cable is ~ 4 m, so by adding or subtracting 30 cm lengths of cable we have relatively fine control over the LO phase. The total cable length before the LO input of the mixer is modified until the error signal takes the form it should. In order to determine whether the error signal is oriented properly we can activate the high-speed feedback to see if the feedback system tries to lock the sidebands or the carrier to the
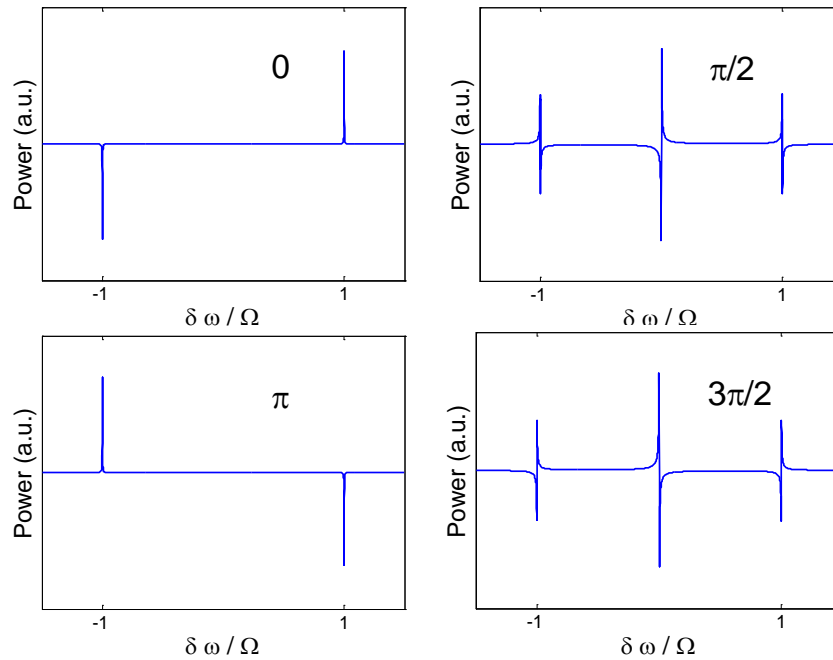
Figure 3.4 Output of the mixer as the phase of the local oscillator is changed. The phase lag is shown within each figure.

cavity. If the feedback system is clearly trying to lock to the sidebands rather than the carrier, an additional $180°$ phase flip is required on the local oscillator.

3.2.3 Feedback electronics design

Once the error signal is produced, the next task is to design the feedback electronics necessary to lock the laser to the cavity. There are several considerations that go into the design of the electronics; generally the goal of the electronics is to put as much gain on the signal as possible while preventing positive feedback noise on the system. For example, when designing the PZT feedback electronics one must consider the PZT resonance near 1 kHz; high gain on the error signal at frequencies below this resonance will ensure a robust lock, but the gain on the error signal must be well below unity at the resonant frequency, otherwise the feedback signal will actually contribute to system instability. Striking this balance is one of the most important and difficult aspects of the Pound-Drever-Hall technique.

3.2.4 Piezo feedback (slow feedback)

The circuit used in our setup is shown in figure 3.5.

Figure 3.5 Circuit diagram for piezo feedback electronics.

In a feedback electronics context, the piezo can be viewed as capacitor and, when modeling the system, we treat it as such. The cavity piezo, which we use for locking, has a capacitance (quoted by manufacturer) of $C_{piezo} = 5$ μF. The piezo and piezo driver system can be viewed as a low pass filter whose bandwidth is primarily determined by the piezo capacitance. Taking the output impedance of our piezo driver ($R_{out} = 150$ Ω, $C_{out} = .047$ μF) into account we can calculate a rough bandwidth of 210 Hz, using equation 3.13.

$$\text{bandwidth} = \frac{1}{2\pi R_{out}(C_{out} + C_{piezo})} \tag{3.13}$$

It is important to note that piezos have strong resonances typically in the kHz frequency range. This resonance is the main limiting factor on the piezo feedback bandwidth. This resonant frequency is unique to each piezo and also depends on the piezo load, in this case the cavity mirror and optics adapter. In addition to the bandwidth calculation above, we must find the frequency at which this resonance occurs. In order to find this resonance, we couple our beam to the cavity and scan the laser piezo, allowing us to see laser power transmitted through the cavity at the cavity resonances. We then send a small sinusoidal voltage to the cavity piezo driver and observe the oscillations of the transmitted peak. We increase the frequency of the driving voltage until we observe the amplitude of oscillation of the resonant peak increase dramatically and suddenly. We observe this behavior at a frequency of 4.5 kHz.

With a good idea of the upper limit of the piezo feedback bandwidth we can now design the feedback circuit. The circuit shown in figure 3.5 is designed to, in conjunction with the piezo and piezo driver system, have as much gain as possible at low frequencies while falling well below unity at the piezo resonance. The circuit has two gain stages, A and B. The first (A) provides a factor of 10 voltage gain and rolls off near 40 Hz. This low bandwidth is required to avoid gain at $\sim$ 1 kHz. After the 40 Hz 3 dB point of this stage, the gain falls with a slope of 20 dB/decade and the signal phase lags the input by $90°$.

In order to get more gain at DC levels we add another gain stage (B). One must be cautious when adding additional gain stages so as not to make the circuit unstable. For example, another RC inverted OPAMP gain stage with the same bandwidth as the first would have the overall effect of doubling the slope of the gain roll-off above 40 Hz, 20 dB/decade $\rightarrow$ 40 dB/decade, and pushing the phase lag to $180°$ above 40 Hz, which would cause positive feedback making any type of lock impossible. The gain stage B avoids this problem by including a resistor in the capacitor branch of the feedback. This has the effect of producing very high gain with no phase lag (V $\times$ 100) at low frequencies and unity gain with no phase lag above 40 Hz. The phase lag dips to $90°$ as the circuit makes the transition from high gain to unity gain around 40 Hz, but comes back to zero above this frequency and remains at zero all the way out to the unity-gain bandwidth of the OPAMP at 4 MHz.
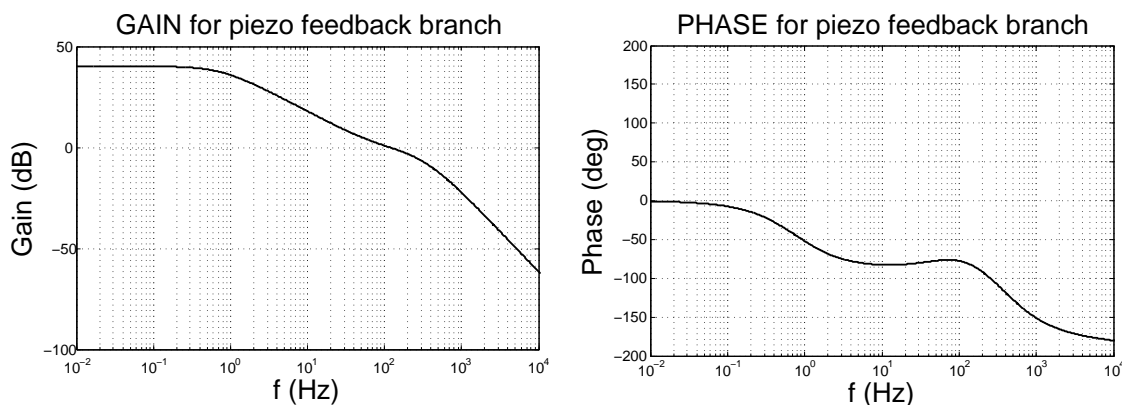
Figure 3.6 Frequency response of the piezo feedback at maximum gain. This includes the bandwidth of the piezo and piezo driver.

The Bode plot for the piezo feedback, including the effects of the piezo and piezo driver, is shown in figure 3.6. The gain shown in the Bode plot corresponds to the gain from the feedback electronics and the phase corresponds to the phase lag between the output and the input. The feedback circuit crosses the unity gain point at 100 Hz; at this point the phase margin ($180° - |\phi|$) is over $90°$, which is well above the minimum phase margin required for stable operation. As a rule of thumb, a phase margin of $45°$ ($135°$ phase lag) is the point at which the gain must be below unity [52, 53]. The gain is -20 dB at 1 kHz, where the phase margin is $\sim 45°$ and where the piezo resonance would introduce instabilities to the system. When looking at the reflected signal immediately after the DC block on the photodiode (see figure 3.3) on a spectrum analyzer we see features 3 kHz from the modulation frequency of 50 MHz when the cavity is locked, but these are not the sharp spikes characteristic of positive feedback instabilities [53]. This suggests the piezo feedback is working within a comfortable phase margin.

Residual AM from the EOM will also be present in the error signal and will manifest itself as a DC offset to the locking signal. The trim pot across the zener diodes shown in the circuit diagram (figure 3.5) serves to eliminate this AM offset. As mentioned previously, in section 3.2.2, AM drift from the EOM can be problematic because it constitutes a drift of the zero of our locking signal. With our original $LiNbO_3$ EOM, it was not uncommon to see drifts on the order of the error signal peaks themselves. In our current setup, which uses a KDP crystal, the DC drifts from thermally

induced AM are much smaller than the error signal itself allowing us to maintain a lock for 10's of minutes to an hour.

3.2.5   Laser feedback (high-speed feedback)

Locking to a cavity with a finesse of $\sim 20,000$ requires a large servo bandwidth. Because the feedback to the cavity piezo is ultimately limited by the piezo resonance at the kHz level, an additional feedback branch to the laser is required. The laser feedback in our system operates from 100 Hz to nearly 1 MHz. Because the error signal is linear within the linewidth of the laser we can use the signal to narrow the linewidth of the laser itself. The narrowing of the linewidth can be seen in figure 3.7 which shows the power transmitted through the cavity as the cavity piezo is scanned. The left peak shows the cavity transmission when there is no feedback on the laser, the right peak shows the same peak at the same scan rate when the high-speed feedback is activated. As the cavity piezo scans through the resonance, the high-speed feedback attempts to lock the laser to the cavity. The transmitted power increases significantly when the feedback is on due to the fact that the laser linewidth is narrowed and more of the input beam is able to "fit" into the cavity.
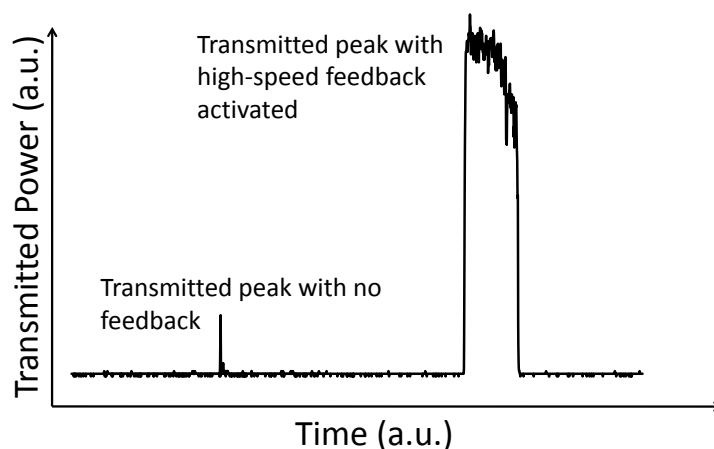
Figure 3.7 Comparison of the power transmitted through the scanning cavity with high-speed feedback off and on. The increase in power transmitted through the cavity is due to the narrowing of the laser linewidth.

The limiting factor for the bandwidth of this branch is the response of the laser. Diode lasers typically do not have "well-behaved" frequency roll-offs; the accumulation of phase-lag can be sharp and is difficult to model with a simple RC filter. For this reason it is good to have the feedback gain be very low at the laser bandwidth frequency to prevent unpredictable problems with positive feedback. To roughly characterize the frequency response of the laser, we put an oscillating current on top of the DC laser diode current and measure the phase difference between the input wave and the resulting power fluctuations on the beam. We find that the laser power variations remain in phase with the driving current up to roughly 500 kHz and then begin to lag sharply, becoming roughly $60°$ out of phase at 5 MHz

The optical cavity has a frequency response that must be accounted for as well. In section 3.1 we discussed the importance of having the modulation frequency be larger than the linewidth of the cavity; the reason for this is that the cavity response (given by the cavity linewidth of ~ 30 kHz) is too slow to for the sidebands (~ 10 MHz) to build up inside the cavity. The sidebands do not couple to the cavity; they interfere with the fields leaking from the cavity. Frequencies on the carrier that are less than the cavity linewidth will couple to the cavity. We can seek to characterize the response of the cavity by finding the decay time of the intra-cavity fields. To roughly measure the frequency response of the cavity we quickly scan the cavity piezo across a resonance. The ringdown is clearly visible on the tail of the transmitted power spike (see figure 3.8). We fit a curve to the ringdown and find the decay time constant (τ). Averaging over several measurements taken on our 27 cm length cavity we find $\tau \sim 8.16~\mu$s.

After measuring the time response to an impulse, we have enough information to characterize the frequency response of the system. The cavity linewidth is related to the decay time by $\Delta\nu_{1/2} = 1/(2\pi\tau)$ [49]; a ringdown time of $8.16~\mu$s gives a cavity linewidth of 14 kHz, which is in reasonable agreement with our cavity linewidth calculation based only on the reflectivity of the mirrors and the length of the cavity (38 kHz). The Laplace transform of an impulse is unity, so the time response of the cavity to an impulse gives us the transfer function of the cavity. The inverse of the time
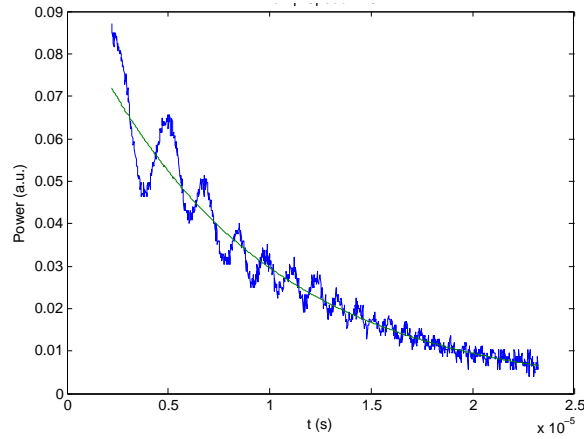
Figure 3.8 Transmitted power through the cavity as piezo is quickly scanned across resonance. Only the ringdown tail is analyzed so the plot begins at the peak of the transmission spike.

constant is a pole, p, of the transfer function $P(s)$.

$$P(s) \propto \frac{1}{p + s} \qquad (3.14)$$

By plotting the magnitude and phase of $P(i\omega)$ we can see what the frequency response of the optical cavity is (figure 3.9). The 3 dB point of the 27 cm optical cavity is located at $\sim$ 140 kHz.
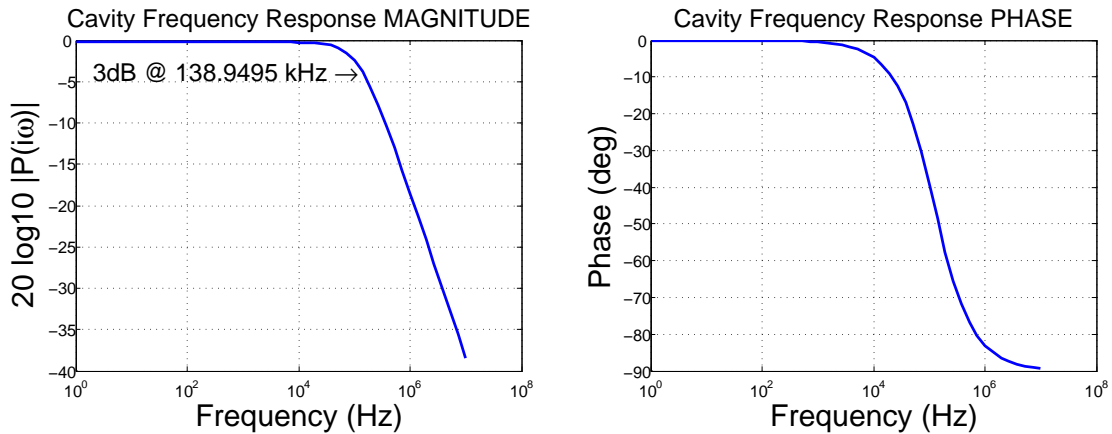
Figure 3.9 Frequency response of the 27 cm length optical cavity. The 3dB point for this system is at 140 kHz

The bandwidth limitations of the cavity and laser are both taken into account when designing the high-speed feedback circuit shown in figure 3.10. When working with feedback systems it

is important to make sure that when the phase lag of the feedback nears $180°$, the gain on the feedback signal is below unity; if this is not the case the feedback electronics will put positive feedback noise onto the system. In previous versions of our high-speed electronics this positive feedback was clearly visible and manifested itself as sidebands at the positive feedback frequency (typically about 5 MHz). When looking at the reflected signal after a DC block on a spectrum analyzer, sharp spikes 5 MHz above and below the modulation frequency were visible as well. In order to extend the bandwidth of our feedback we add a phase lead at 200 kHz. This pushes the phase margin higher and allows us a higher bandwidth.
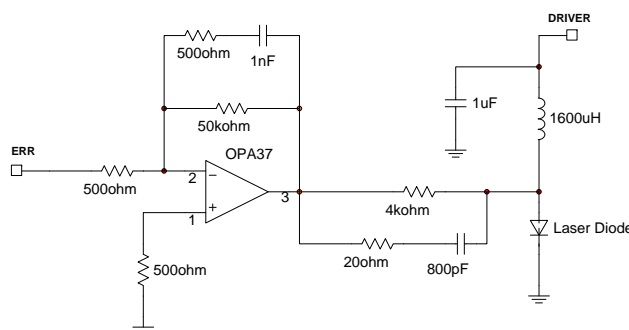
Figure 3.10 High-speed laser diode feedback circuit

By introducing this phase lead we increase the bandwidth at the expense of gain at lower frequencies. In order to ensure robust locking we include an low noise amplifier in the circuit to boost the signal at lower frequencies. Standard compensated OPAMPS have a gain-bandwidth product of $\sim$ 5 MHz. In this case, a voltage gain of 10 at lower frequencies would limit the bandwidth of the amplifier to 500 kHz and the OPAMP roll-off would work against the phase lead we introduced. To overcome this limitation we use an uncompensated OPAMP with a gain-bandwidth product of 80 MHz. This allows the phase lead to function without competing with the phase lag introduced by the amplifier. Figure 3.11 compares the response of the system with just a phase lead and with a phase lead / amplifier combination. The Bode plot 3.11 clearly shows how we are able to substantially increase the gain at lower frequencies while still converging on the comfortable phase margin required to prevent positive feedback instabilities.
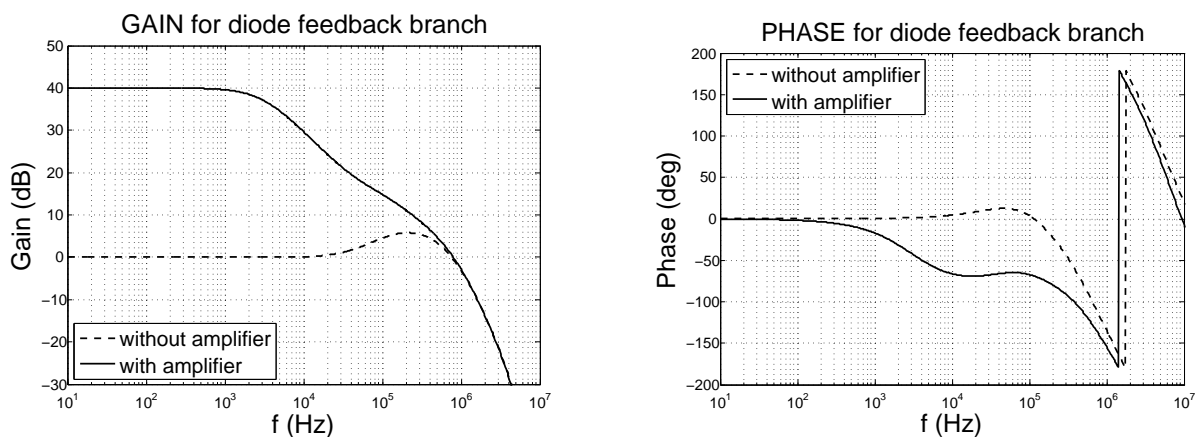
Figure 3.11 Bode plots for high-speed feedback. These plots account for amplifier, cavity, laser bandwidths.

In an effort to minimize noise on the feedback signal and ensure that no additional phase lag is introduced by standard DIN sockets and wiring we connect the laser driver and feedback directly to the diode through an SMA cable. The cable is cut and the core and shielding are soldered directly to the laser diode pins. The high-speed circuitry is soldered directly to SMA connections as well. An inductor and capacitor are included between the laser driver and the feedback system; this is to isolate the driver from the feedback signal and to minimize noise from the driver itself.

In the case of both the high-speed feedback to the laser diode and the slow feedback to the cavity piezo, additional adjustments must be made to the input error signal in order to optimize the lock. Attenuators must be added after the final splitter before the feedback circuits in figure 3.3. Without these attenuators, the signal back to the diode or piezo may be too great, increasing the overall signal to the component and possibly causing positive feedback problems. We begin by optimizing the high-speed feedback by activating it while ramping the cavity piezo. We look at the height and width of the transmitted peaks and adjust the optical signal to the initial photodiode with a $\lambda/2$ plate and beam cube; by adjusting the input signal we get a clue as to whether more or less signal is required for optimal feedback. In this way we try to maximize the height of the transmitted peaks. After the high-speed signal is optimized, we add or subtract attenuators to the

piezo feedback branch and empirically find the best level of attenuation by repeatedly locking the laser with different attenuation values.

Chapter 4

Rotational Raman Generation in D_2 at Room Temperature

In this chapter we discuss rotational Raman generation in a high-finesse cavity at room temperature. In this experiment we use a pump laser at 1.5 μm to drive the rotational transition $\nu'' = 0$, $J'' = 1 \rightarrow \nu' = 0$, $J' = 3$ and generate a Stokes beam at 1.63μm. We are able to generate over 300 mW of continuous-wave rotational Stokes power, the most ever generated using a cavity-based Raman generation scheme [40].

4.1   Experimental Setup

The experimental setup is shown in figure 4.1 and described in this section. We begin with an external-cavity diode laser (ECDL) tuned to 1.55μm. The laser has a linewidth of ~ 500 kHz and an optical power of ~ 20 mW. This beam is then modulated by an electro-optic modulator (EOM) at 20 MHz; this modulation is used to produce the locking signal as described in chapter 3. The modulated beam is then amplified by an IPG Photonics erbium-doped fiber amplifier. This amplifier produces up to 30 W of continuous-wave output power from 5 mW seed power. The output beam is emitted via a single-mode polarization maintaining optical fiber with an integrated isolator attached; this allows for a pure Gaussian spatial mode of the amplified beam which is ideal for coupling to the high-finesse cavity. The amplified Gaussian output beam has a measured polarization purity of 99%.

The beam goes through an additional isolator immediately after leaving the amplifier. This additional isolation stage is critical because a consequence of ideal coupling to the optical cavity is that the back reflection from the cavity overlaps the input beam. Light coupled to the amplifier

in the wrong direction can critically damage it; so we must take care that the full back-reflected 30 W cannot reach the amplifier.

After the isolator, the beam is coupled to the TEM_{00} mode of the high-finesse cavity by using a mode-matching lens. To achieve optimal coupling to the cavity we treat the cavity mirrors themselves as diverging lenses (with a focal length depending on the mirror material and radius of curvature of the mirror surfaces), measure the beam profile and radius of curvature of the input beam, and use the complex ABCD matrix formalism to calculate the ideal focal length and position of the mode-matching lens.

Immediately before the cavity we convert the horizontal polarization of the input light to circular polarization with a $\lambda/4$ plate. We use circular polarization to maximize the rotational generation in the cavity. The back-reflected beam will have opposite circular polarization; upon passing again through the $\lambda/4$ plate, the back-reflected radiation has vertical polarization and can be diverted with a beam cube to the reflected signal photodiode. It is this signal that is used to produce the locking signal.

The high-finesse cavity consists of two custom-made mirrors from Precision Photonics. The mirrors have a radius of curvature of 50 cm and are separated by 27 cm. This sub-confocal separation allows us to discriminate between the cavity modes and couple the light only to the TEM_{00} mode. This configuration gives a free spectral range of 555 MHz. One of the mirrors is mounted on a piezo allowing us the flexibility to scan and lock with the cavity mirrors, rather than the piezo on the ECDL. The measured transmittance of the cavity mirrors is 38 ppm at the pump wavelength and 277 ppm at the Stokes wavelength. The losses (both absorptive and scattering) are around 100 ppm according to the manufacturer. From these reflectivities we calculate a cavity finesse of 22,764 at the pump wavelength and 8332 at the Stokes wavelength.

The high-finesse cavity is placed in a chamber filled with .1 atm of D_2 gas. The amplified pump beam is then locked to the cavity via the Pound-Drever-Hall technique [47] described in chapter 3.
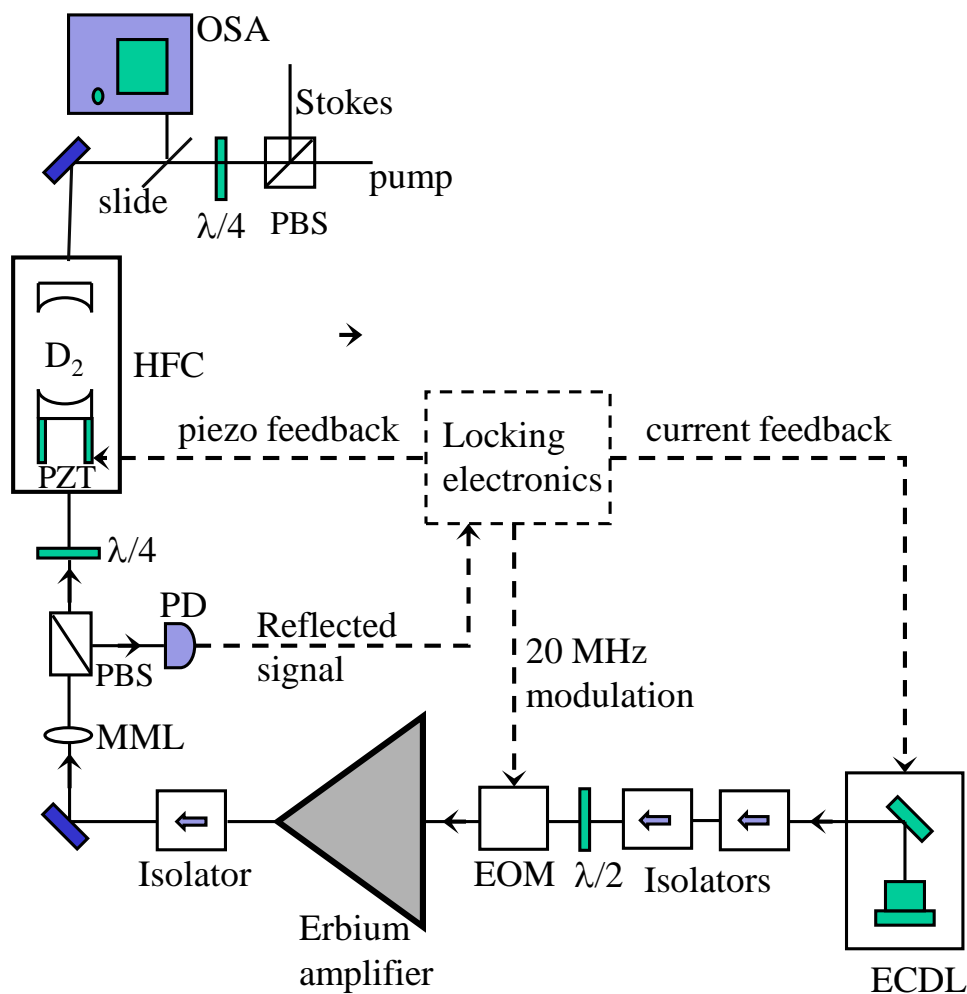
Figure 4.1 Experimental setup for the room temperature rotational Raman generation experiment. An external cavity diode laser centered at 1.5 μm is modulated at 20 MHz by an electro-optic modulator and amplified to up to 30 W by an Erbium-doped fiber amplifier. This amplified beam is then converted to circular polarization and locked to a D_2-filled high-finesse cavity. After the cavity, the pump and generated Stokes beams (which are opposite circular polarization) are separated and measured. ECDL, external-cavity diode laser; $\lambda/2$: half-wave plate; EOM, electro-optic modulator; MML, mode-matching lens; PBS, polarizing beam splitter; $\lambda/4$, quarter-wave plate; HFC, high-finesse cavity; PZT, piezoelectric transducer; PD, photodiode; OSA, optical spectrum analyzer.

4.2 Cavity Performance

Figure 4.2 shows the transmitted power of the pump beam when locked to the evacuated high-finesse-cavity. For an incident pump power of 25.4 W we find that 929 mW is transmitted. Clearly the transmitted power is significantly lower than the incident power. This is due in part to the fact that the absorptive/scattering losses of the cavity are greater than the transmittance of the mirrors at the pump wavelength. The spatial mode matching is imperfect as well. We took care to model the system when choosing the lens focal length and distance from the cavity, but our knowledge of the characteristics of the physical input beam and optical elements is limited, which prevents our achieving perfect mode matching. In addition to these factors, the locking electronics bandwidth is ultimately limited by the laser diode/optical cavity bandwidth. This bandwidth limitation results in imperfect spectral narrowing of the ECDL.

By measuring the output power of the cavity we can calculate the peak intensity of the light inside the cavity with our knowledge of the mirror transmittance and the calculated waist of the cavity mode. We use the formula

$$w_0 = \frac{L\lambda}{\pi}\sqrt{\frac{1+g}{4\left(1-g\right)}} \tag{4.1}$$

where

$$g = 1 - \frac{L}{R} \tag{4.2}$$

to calculate the waist of the cavity mode given the length of the cavity, L, and the radius of curvature of the cavity mirrors, R [46]; we find the waist for our parameters to be 331 μm. With this information we find the peak intensity of the intra-cavity field to be 14.1 $\mathrm{MW/cm^2}$.

4.3 Raman Generation Inside the Cavity

Figure 4.3 shows the energy level diagram for the process discussed in this chapter. The Stokes beams are generated from different rotational states in the same vibrational state of the molecule. In
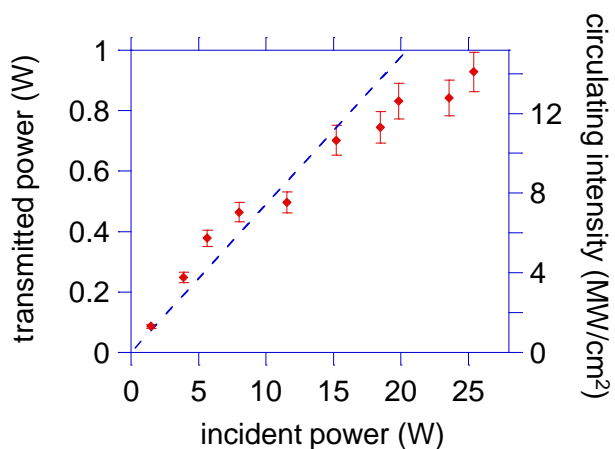
Figure 4.2 Transmission of pump beam through high-finesse cavity (without D_2) The dashed line is a linear fit the the first six data points. For an input power of 25.4 W (measured immediately in front of the cavity) we calculate a peak intra-cavity intensity of 14.1 MW/cm^2 using the known parameters of our experiment.

a homonuclear molecule (such as D_2), Raman transitions with $\Delta J = \pm 1$ are forbidden; rotational Raman transitions are allowed with the condition $\Delta J = \pm 2$ [54].
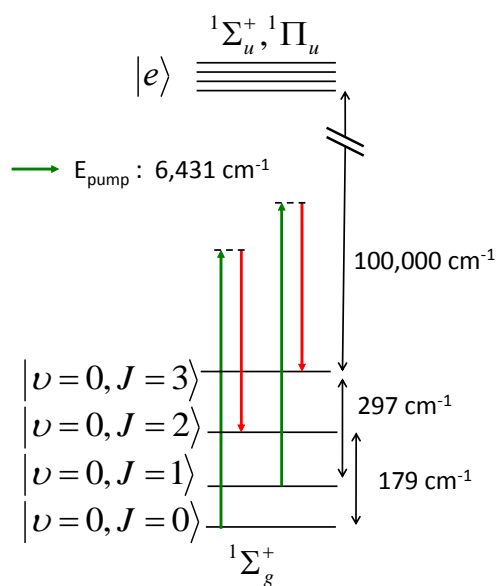
Figure 4.3 Energy level diagram for rotational stokes transitions in Deuterium gas.

Because the input pump light is circularly polarized, the generated Stokes light has opposite circular polarization. As the pump beam propagates through the medium, a Stokes photon is generated from noise. The cavity mirrors are highly reflective at the Stokes wavelength as well as the pump so a Stokes photon emitted into the cavity mode will experience a large degree of optical feedback and the Stokes field will build in the cavity. When the gain on the Stokes beam equals the losses due to the cavity mirrors the Stokes beam will lase, as discussed in section 2.3, and all the excess pump photons will be converted into Stokes photons. This is clear in figure 4.6 where the pump power plateaus as the Stokes power begins to increase linearly with input power.

We are able to generate rotational Raman Stokes beams on both the $|\nu = 0, J = 1\rangle \to |\nu = 0, J = 3\rangle$ and $|\nu = 0, J = 0\rangle \to |\nu = 0, J = 2\rangle$ transitions. These rotational transitions are 297 cm^{-1} (8.9 THz) and 179 cm^{-1} (5.3 MHz) respectively. Figure 4.4 shows an example of a typical optical spectrum analyzer scan for this experiment; this shows the $J = 1 \to J = 3$ transition.
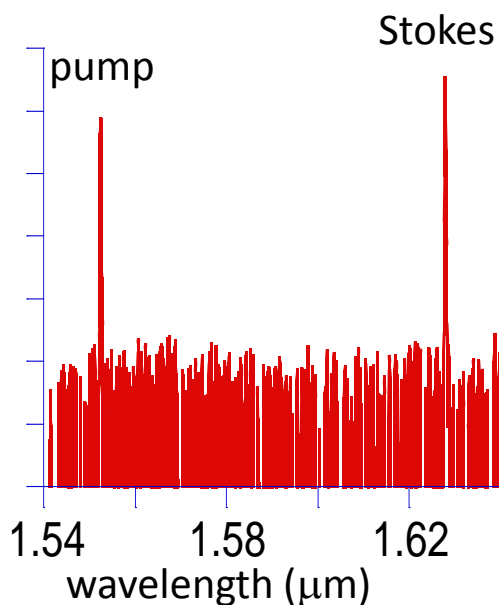
Figure 4.4 Typical optical spectrum analyzer output showing the clear generation of a Stokes beam at the $J = 1 \to J = 3$ transition.

We control which transition we drive by changing the cavity length with the cavity mirror piezo. As discussed in chapter 2, a Stokes beam will tend to dominate when the resonant frequency of the

cavity matches with the Raman transition frequency to within the Raman linewidth. By adjusting the cavity piezo we change the cavity's resonant frequency such that either the $J = 1 \rightarrow J = 3$ transition or the $J = 0 \rightarrow J = 2$ transition is favored.
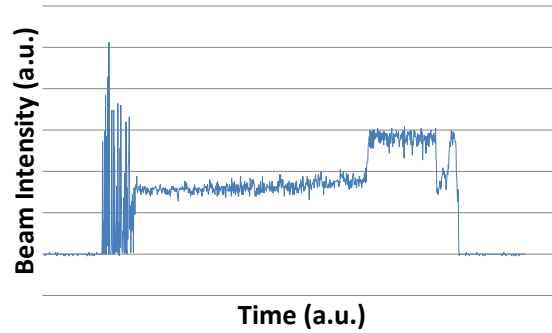
Figure 4.5 Scanning the cavity piezo across the cavity resonance we can see the two different channels for Raman generation competing. This figure shows the measured power transmitted through the output cavity mirror with time as we scan through a resonance. The higher measured power corresponds to the $J = 1 \rightarrow J = 3$ transition while the lower corresponds to $J = 0 \rightarrow J = 2$.

For some cavity lengths we see competition between these modes or lasing in both transitions simultaneously. Figure 4.5 shows the signal that is transmitted through the cavity as a function of time as we scan the cavity piezo with the feedback to the laser diode active. The upper level of the transmitted signal is the $|\nu = 0, J = 1\rangle \rightarrow |\nu = 0, J = 3\rangle$ transition while the lower level is $|\nu = 0, J = 0\rangle \rightarrow |\nu = 0, J = 2\rangle$. By gaining familiarity with the shape of the transmitted signal as we scan the piezo we can quickly find the desired rotational transition to lock to.

As mentioned above, we are able to achieve Raman generation at two rotational transitions. Figure 4.6 showing the generated Stokes beam power as a function of input power for each transition. The $J = 1 \rightarrow J = 3$ transition is has a greater conversion efficiency and higher overall generated Stokes power than the $J = 0 \rightarrow J = 2$ transition. This is due to the fact that, at room temperature, the majority of the molecules (31 %) are in the $|\nu = 0, J = 1\rangle$ state while only 14 % are in the $|\nu = 0, J = 0\rangle$ state.

Using the method described in section 2.3, we estimate a Raman laser threshold of 223 mW of incident pump power. Experimentally we observe a threshold of 1.1 W for the $J = 1 \rightarrow J = 3$

transition, as can be seen in figure 4.6. One possible explanation for this discrepancy includes imperfect frequency overlap of the cavity mode of the generate Stokes beam with the Raman gain peak. We also suspect that the intensity measurements made with vacuum in the high-finesse cavity are not valid when gas is introduced. Thermal effects caused by the introduction of the deuterium gas in the system degrade the lock and decrease the optical power coupled into the cavity. For this reason higher input powers may be required to achieve the intensities show in figure 4.2.
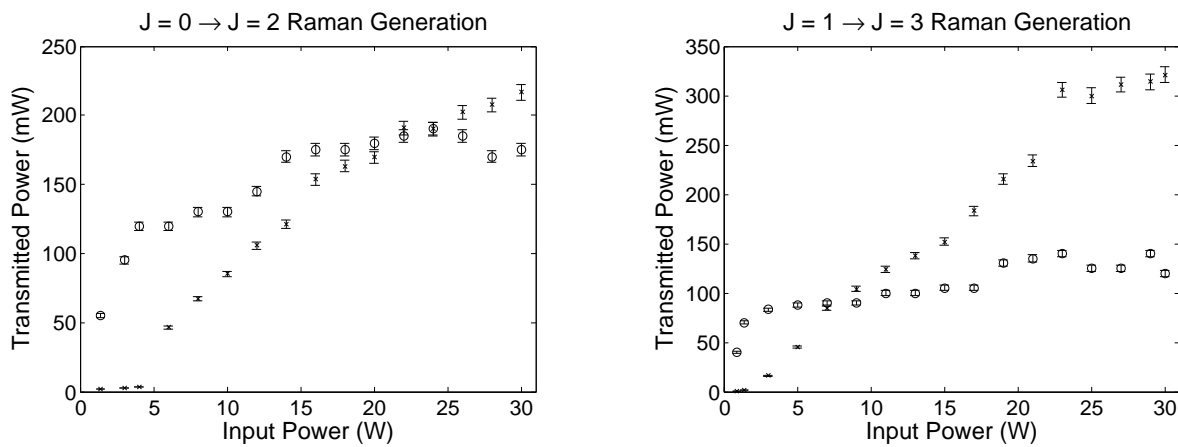
Figure 4.6 Stokes laser output measured after output mirror of the high-finesse cavity. Pump power → ∘, Stokes power → ×. One laser uses the $J = 0 \rightarrow J = 2$ transition while the other uses the $J = 1 \rightarrow J = 3$. The conversion efficiency and overall generated Stokes power is greater for the $J = 1 \rightarrow J = 3$ case because of the greater initial population in the $J = 1$ state.

Using the scheme described in this chapter we were able to produce the highest ever generated Stokes power using cavity-based gas-phase Raman generation. This generation was achieved using two orders of magnitude lower Deuterium pressure than previous work [55]. While this experiment makes significant strides in cavity-based Raman generation there is still room for improvement; one of the most straightforward ways to improve the efficiency of the Raman generation within the cavity is to cool the gas to liquid Nitrogen temperatures. This motivation for cooling the deuterium gas and preliminary results of cooled-cavity Raman lasing are described in detail in chapter 7.

One important aspect of our particular cavity-based scheme is the lower pressures we require to produce stimulated Raman scattering. In each of our experiments we work with pressures nearly 2 orders of magnitude lower than previous experiments [55, 20], and, in the case of the cooled

experiment described in chapter 7, almost 3 orders of magnitude lower. By working at lower pressures we minimize nonlinear thermal effects which degrade cavity coupling. Thermal lensing in optical cavities was studied extensively by the Carlsten group [25, 24]. Because emission from the metastable higher vibrational or rotational state is dipole forbidden, transitions to the ground state will be primarily due to molecular collisions. The energy lost by the decay is not lost as radiation, but as translational kinetic energy of the molecule. This kinetic energy distribution modifies the refractive index of the medium, shifting the resonant frequency of the beam in the cavity and possibly deforming the beam shape as well. The rate at which the collisions occur increases with pressure so by operating at lower pressures we can minimize the rate of collisions and these thermal effects. By working with lower pressures we are also able to attain a much higher coherence than previous experiments. The rotational Raman linewidth (which essentially the collisional broadened linewidth) is significantly narrower due to fewer molecular collisions at a lower density, which allows higher peak coherence.

Chapter 5

Vibrational Raman Generation in D_2 at Room Temperature

In chapter 4 we discussed Raman scattering in D_2 gas using rotational Raman transitions. In D_2, the frequency difference between the pump and Stokes beams is 9 THz, for $J = 1 \rightarrow 3$ transitions. One of the main motivations for exploring vibrational Raman transitions is the fact that this frequency difference is approximately 90 THz. This allows us to produce coherent light at frequencies very far from our monochromatic pump. We have experimentally demonstrated the generation of coherent Raman sidebands spanning from 807 nm to 1.5 μm [56]. By producing coherent beams that span this range of frequencies we can infer the production of near-single-cycle pulses.

5.1   Experimental Setup

These vibrational experiments are carried out at room temperature in the same cavity with the same cavity mirrors as our previous room temperature rotational Raman experiments (see chapter 4). This means, once again, the cavity length is 27 cm, which corresponds to a free spectral range of 555 MHz. The cavity mirrors have a radius of curvature of 50 cm so the cavity is sub-confocal, allowing us to discriminate between the spatial cavity modes and couple to only the TEM_{00} mode.

To have efficient cavity-based continuous-wave Raman generation it is critical to have the cavity mirrors highly reflective at the pump and Stokes wavelengths. The mirrors used in our experiments are coated to be highly reflective at 1064 nm and 1550 nm; the scattering, absorption, and transmission losses of the mirrors at each of these wavelengths is at the level of 100 ppm (parts per million). The frequency difference between these center wavelengths is the same as the frequency

of the Raman transition. This means that a pump beam at 1064 nm will be able to resonate with the cavity and produce a vibrational Stokes laser resonating near 1550 nm as well.
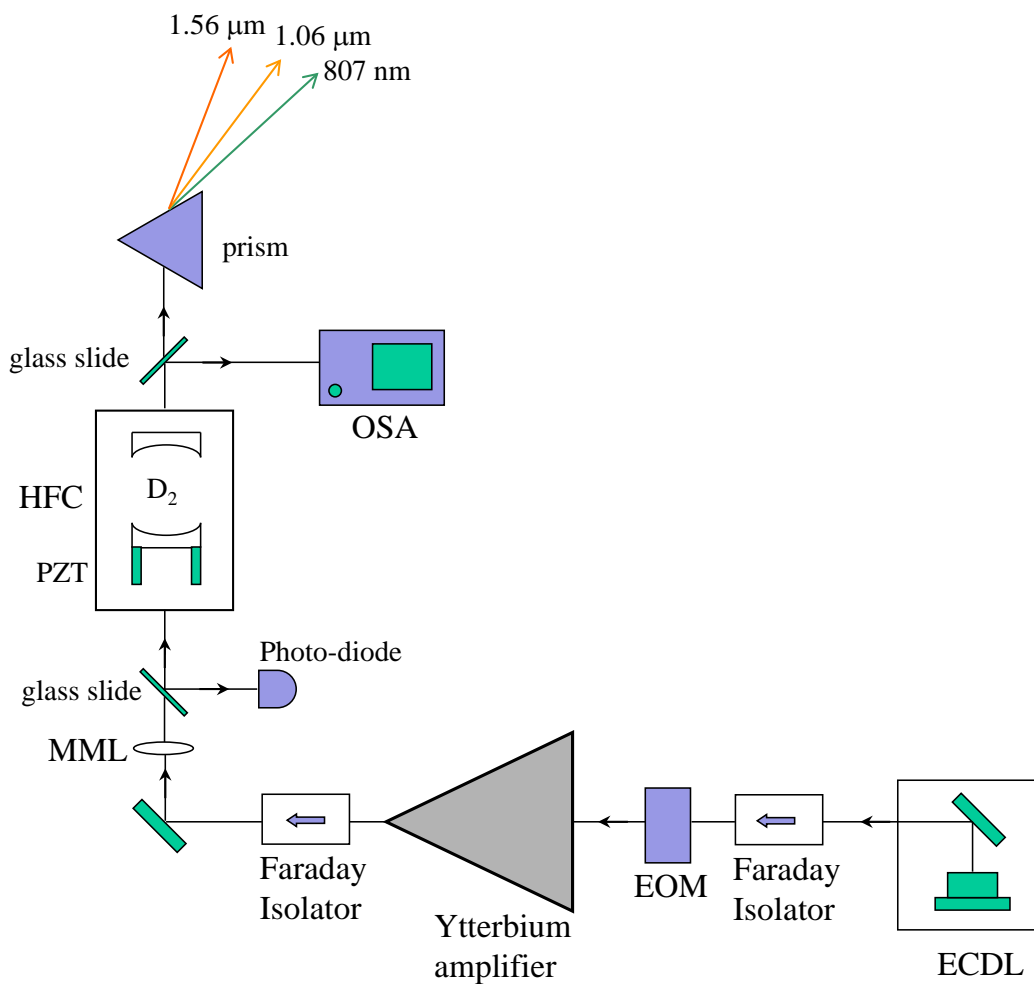
Figure 5.1 The experiment begins with an external cavity diode laser at 1064 nm. This beam is modulated by an electro-optic modulator and amplified to up to 20 W by an Ytterbium-doped fiber amplifier. This linearly polarized light is then locked to a high-finesse cavity filled with .1 atm of D_2 gas. Raman sidebands are generated on the pump beam at 807 nm and 1560 nm. These sidebands are then separated and measured by a prism after the cavity. ECDL: external cavity diode laser, EOM: electro-optic modulator, MML: mode matching lens, HFC: high-finesse cavity, PZT: piezo-electric transducer, OSA: optical spectrum analyzer.

The experiment (figure 5.1) begins with a home-built external cavity diode laser (ECDL) tuned to our selected pump wavelength of 1064 nm. This laser system has an optical power of roughly

20 mW and a linewidth of $\sim$ .5 MHz. After a Faraday isolator, the beam is phase-modulated by an electro-optic modulator (EOM) at 50 MHz; this modulation is required for the generation of the cavity locking signal.

This continuous-wave modulated signal is then amplified to up to 20 W by an Ytterbium-doped fiber amplifier from IPG photonics. Because we are working with linear polarization in this case we cannot rely on a $\lambda/4$ plate, polarizing beam cube pair to divert the back-reflected power from the cavity; when not locked to the cavity, all the incident light is reflected back on itself. To protect the amplifier from this direct and powerful back-reflection we add an additional isolator after the amplifier. In order to minimize the peak optical intensities in the isolator's crystal we take great care in maximizing the beam size through the isolator while avoiding clipping. Even with these careful beam size considerations, at full power (30 W continuous-wave emission) the isolator is dangerously close to its damage threshold. To avoid failure of the isolator and possible damage to the amplifier we choose to run the amplifier at just 2/3 its maximum power.

The 1064 nm pump beam is locked to the cavity via the Pound-Drever-Hall locking technique. A small portion of the reflected beam from the cavity is reflected by the face of a glass slide and collected on a photodiode. This signal is sent to the locking electronics. The pump and generated Raman beams are separated after the cavity by a SF11 prism to be measured.

5.2   Stokes Generation

When the difference between the pump frequency and resonant frequency of the cavity at the Stokes wavelength falls within the Raman linewidth of the transition (see figure 5.3) the Stokes beam will experience optical feedback and build up in the cavity, just as in the case of rotational Raman generation discussed previously. At room temperature the linewidth of the Raman transition is primarily the Doppler-broadened linewidth of 530 MHz. For comparison, the free spectral range of the cavity (27 cm length) is 555 MHz. The overlap between the emission of the Stokes beam and the cavity modes into which the Stokes beam emits is roughly depicted in figure 5.3. The calculated linewidth of the cavity is near 40 kHz while the Raman linewidth is 550 MHz; therefore
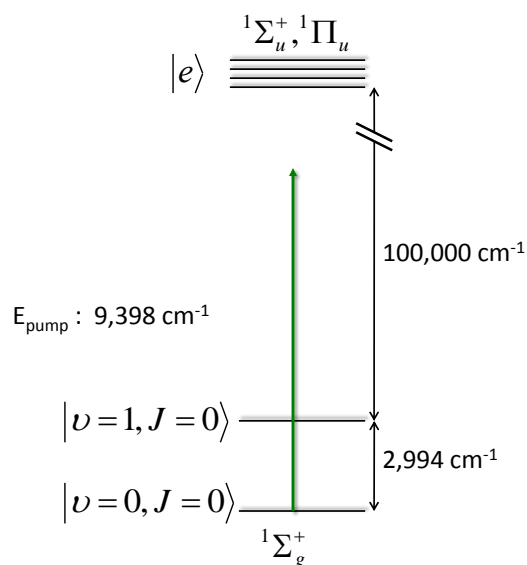
Figure 5.2 Energy level diagram for the vibrational Raman transition. The difference between the ground and first vibrational states of D_2 is 2,994 cm^{-1} (89 THz). The pump laser is very far detuned from the upper electronic states with a frequency only 10% that of the electronic transition frequencies.

the role of the cavity is to confine the Stokes radiation to a small sliver of the overall Raman gain curve.

When the cavity length is not matched with the possible vibrational Stokes generation frequencies either no Stokes generation will occur or we will see rotational Raman generation. Once again, we are required to tune the cavity length by adjusting the position of a piezo on one of the cavity mirrors to find the appropriate cavity length for the Raman transition we are interested in. By becoming familiar with the shape of the peaks transmitted through the cavity while scanning we can see which transitions are desired and lock there. Once locked to a vibrational transition we make fine adjustments to the laser frequency by adjusting the position of the piezo-mounted diffraction grating in our extended cavity diode laser setup. We adjust this frequency in an effort to match the emitted Stokes frequency to the peak of the Raman linewidth to maximize the efficiency of the Raman process.

The pump and Stokes power as a function of input power exhibit the same laser-like behavior as in the rotational Raman laser case. When the intra-cavity pump intensity is high enough, the
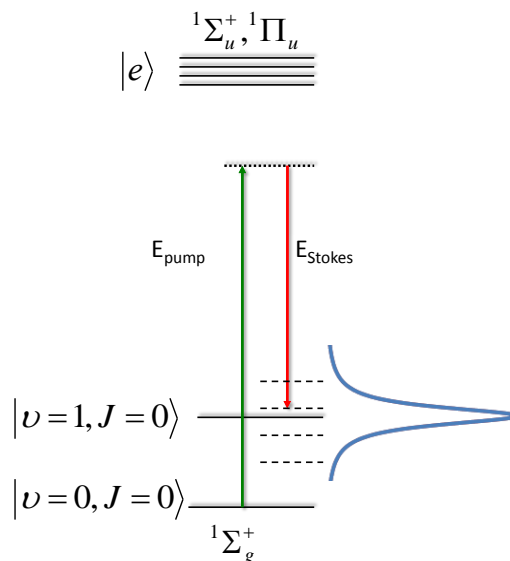
Figure 5.3 The Stokes beam will lase when the resonant frequency of the cavity matches with the difference between the pump frequency and first vibrational state transition frequency to within the Raman linewidth. At room temperature, the Raman transition has a linewidth of 530 MHz (shown in blue) and the cavity resonances (shown by dashed lines) have a linewidth of approximately 40 kHz and are separated by the free spectral range of 550 MHz. These cavity resonances can be tuned to the peak of the Raman linewidth by adjusting the laser frequency with the piezo in the extended cavity laser setup.

gain on the generated Stokes beam overcomes the cavity loses and the Stokes beam begins to lase. After this laser threshold the excess pump photons are converted into Stokes photons. This is clearly visible in figure 5.5; as the Stokes power begins to increase linearly with input power the pump power levels off.

Figure 5.5 shows the pump and Stokes powers as a function of input power for .1 atm and .5 atm. We observe a lasing threshold of 3 W and .6 W respectively, higher than what was predicted in section 2.3. In the case of the higher pressure, the lasing threshold is reduced and the conversion from pump to Stokes is more efficient, as is shown by the lower steady state pump power. This is to be expected at higher densities. Despite the lower threshold and lower steady state pump power, the peak generated Stokes power is not higher than the lower pressure case. One reason for this may be other density related effects; as density increases, other nonlinear effects begin degrade the coupling to the cavity and, therefore, the peak intensities we can achieve in the cavity. This

is visible when locking the laser as the drop in the reflected power level is significantly less when the cavity is filled with gas than when at vacuum. When the cavity is in vacuum, dips 25% to 35% are not unreasonable when locking. With gas present these drop to 5% or 10%. The fact that .1 atm is less disruptive to cavity coupling and the lock may explain why we actually achieve higher Stokes generation at a lower pressure. In light of the thermal effects of molecular collisions on the refractive index of the medium briefly discussed in section 4.3 and investigated extensively in [25, 24], lower pressures are also desirable to reduce thermo-optic variations in the refractive index.

The results shown in figure 5.5 and discussed throughout this chapter involve Stokes generation on the Raman transition between $|\nu = 0, J = 0\rangle \rightarrow |\nu = 1, J = 0\rangle$. It is important to note that we do see lasing on the $|\nu = 0, J = 1\rangle \rightarrow |\nu = 1, J = 1\rangle$ transition as well. These results are shown in figure 5.6. We chose to focus on the transitions with $J = 0$ somewhat arbitrarily; it was mostly based on familiarity and reliability experimentally when locking to these transitions in addition to the fact that the anti-Stokes beam tended to be slightly stronger for the $J = 0$ case.

5.3 Anti-Stokes Generation

As we have already discussed extensively, our system is a Stokes laser. The Stokes beam is generated from noise and experiences optical feedback from the highly reflective cavity mirrors and gain from the effective population inversion rooted in the fact that at room temperature the vast majority of the molecules are in the ground vibrational state as opposed to the first vibrational state. As the intra-cavity Stokes intensity increases another third-order nonlinear process occurs generating an anti-Stokes beam (807 nm) which is shifted up in frequency from the pump by the vibrational transition frequency.

The relevant energy level diagram for the Stokes/anti-Stokes generation process is shown in figure 5.4. From the propagation equations for light in a Raman medium (see Appendix A for definitions of the constants b, $\Delta\omega$, A, and D) we see that the anti-Stokes beam is generated from the pump beam through the coherence of the ground (0) and first (1) vibrational levels of the gas (ρ_{01}).
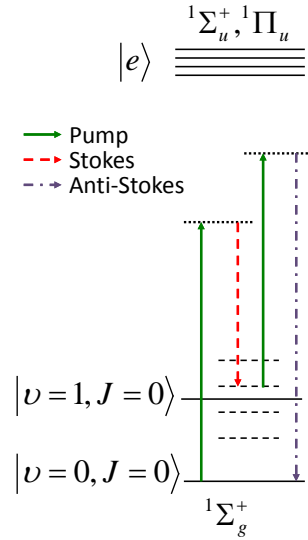
Figure 5.4 Four wave mixing process for anti-Stokes generation in the Raman medium. The Stokes beam is generated from noise and is constrained by the cavity length. The anti-Stokes beam is generated purely from the coherence between the vibrational levels and is determined only by the frequency of the pump and Stokes beams as shown above.

$$\frac{\partial E_{anti-Stokes}}{\partial z} \propto -i2\eta\hbar\omega kNb^*\rho_{01}E_{pump} \tag{5.1}$$

where b is defined in appendix A, N is the gas density, ω and k are the angular frequency and wavenumber of the anti-Stokes beam respectively, and

$$\rho_{01} = \frac{bE_{pump}E_{Stokes}}{A - D + 2\Delta\omega + i\gamma} \tag{5.2}$$

where A, D, $\Delta\omega$, and γ are defined in appendix A. From equation 5.2, it is clear that the coherence between the vibrational states is established through the pump and Stokes beams. The pump and Stokes intensities couple one vibrational state to the other, so, by increasing the pump and Stokes intensities, we increase the coherence between the states. A look at figure 5.5 will show that at .1 atm we generate a higher coherence between the vibrational states simply due to the fact that the circulating power of the pump and Stokes beams is larger. For the powers shown in 5.5 we calculate a peak coherence of 3×10^{-4}.

As the pump and Stokes powers increase as a function of input power in figure 5.5, the anti-Stokes beam is generated as well through the mixing of these waves. The maximum generated anti-Stokes power is approximately 40 μW. While the high-finesse cavity is reflective and resonant at the pump and Stokes wavelengths, the cavity mirrors are not reflective at the anti-Stokes wavelength and the anti-Stokes beam is generated in a single pass through the 27 cm cavity.
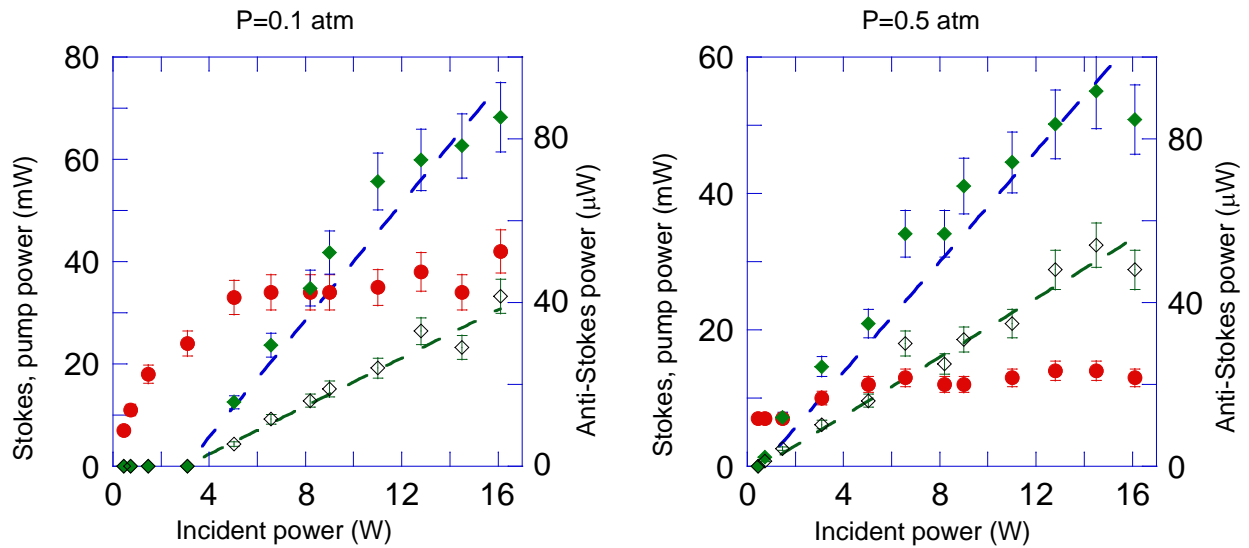
Figure 5.5 Measured power of the pump, Stokes, and anti-Stokes beams after being split by the prism at two different pressures of D_2. Filled green diamonds: Stokes power, filled red circles: pump power, empty diamonds: anti-Stokes power which is meant to be read on right vertical axis.

Figure 5.7 shows a combination of typical optical spectrum analyzer scans. The generated 807 nm and 1.56 μm sidebands are clearly defined and each 90 THz from the single input beam at 1064 nm.

Because the coherence between the states $|\nu = 0, J = 0\rangle$ and $|\nu = 1, J = 0\rangle$ is sufficient to produce an anti-Stokes beam at 807 nm we have reason to believe that we are generating a second Stokes beam at 3 μm with power comparable to that of the anti-Stokes beam. This wavelength is absorbed in many optical materials so we took care to use only optical elements, such as fused silica, that were not absorptive at 3 μm. Detection of 3 μm light is also more difficult than at other NIR and optical wavelengths. Despite using a special detector and the optical material considerations, we were not able to conclusively observe this weak 3 μm component.
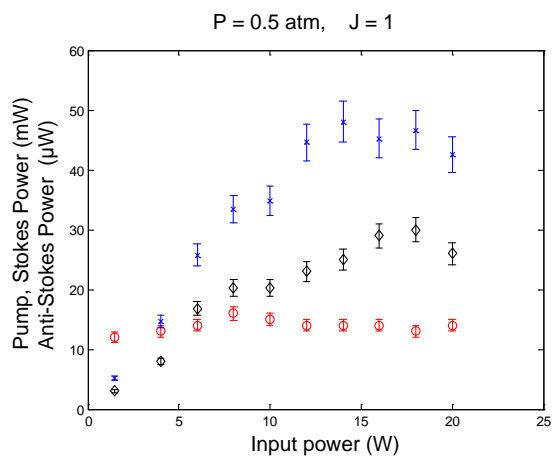
Figure 5.6 Measured power of the pump, Stokes, and anti-Stokes beams after being split by the prism with 0.5 atm of D_2 in the cavity. This power curve shows the results of using the $J = 1$ rotational state instead of the $J = 0$ state as in 5.5. Note that the vertical axis is in mW for pump and Stokes powers and μW for the anti-Stokes power. Blue x: Stokes power, red circles: pump power, black diamonds: anti-Stokes power.
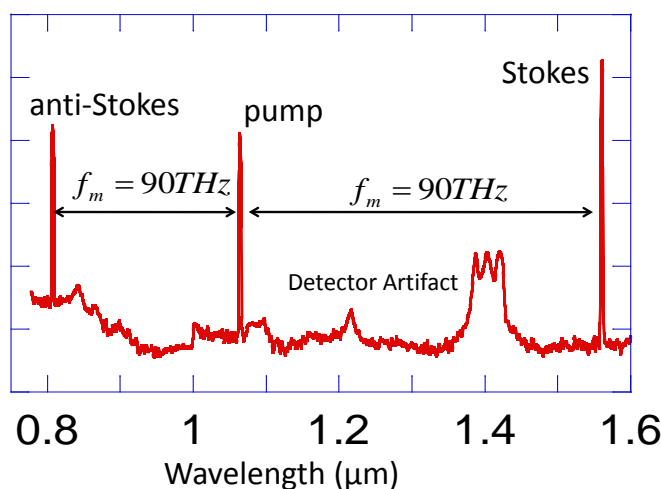
Figure 5.7 Combination of optical spectrum analyzer scans (not to scale) showing the measured wavelengths transmitted from the cavity. Two 90 THz sidebands on the 1064 nm pump are clearly visible.

5.4 Coherence of the beams

While we are able to generate sidebands that span nearly an octave from one monochromatic input beam we must also be sure that these beams have a high degree of coherence. The coherence

of the beams is critical if the sidebands are to be used to modulate the carrier or to form temporal waveforms. To check the coherence of the beams, we investigate nonlinear processes driven by the three overlapped beams in a nonlinear crystal. The nonlinear process we use to investigate the coherence is shown in figure 5.8. Colinearly propagating radiation at 807 nm, 1064 nm, and 1560 nm will generate 532 nm light in a nonlinear crystal. As seen in figure 5.8, this light is generated through two channels: 532 nm is frequency doubled 1064 nm light and the sum of the frequencies of the 807 nm and 1560 nm light. The generation of 532 nm (E_{532}) light can be described by equation

$$\frac{\mathrm{d}E_{532}}{\mathrm{d}z} = id_{eff}\frac{\omega^2}{kc^2}\left|E_{1064}\right|^2\mathrm{e}^{i\Delta k_{harm}z} + \mathrm{e}^{i\phi}2id_{eff}\frac{\omega^2}{kc^2}E_{807}E_{1560}\mathrm{e}^{i\Delta k_{sum}z} \tag{5.3}$$

where k and ω are the wavenumber and angular frequency of the 532 light, respectively. k depends on the refractive index of the medium which is wavelength dependent and is determined by using the Sellmeier equations for the nonlinear crystal being used. d_{eff} is related to the second order susceptibility, $\chi^{(2)}$, of the crystal. The phase mismatch terms in equation 5.3 are

$$\Delta k_{sum} = k_{1560} + k_{807} - k_{532}$$
$$\Delta k_{harm} = 2k_{1064} - k_{532}$$

From equation 5.3 we can see that the two terms on the right hand side of the equation interfere through the phase ϕ. This phase can be controlled by controlling the phase of one of the sidebands. By adjusting the phase of either the 807 nm or 1560 nm sideband we can control whether these nonlinear generation channels interfere constructively or destructively. By adjusting this phase we can measure the interference fringes and see the degree to which our light deviates from the case of perfect coherence.

Figure 5.9 shows our experimental setup for measuring the coherence of the beams. The output radiation of the cavity consists of the pump and two sidebands propagating colinearly. These beams are split by a prism allowing us to control the amplitude (with ND filters) and phase of the sidebands. Phase control is added to the Stokes beam (1560 nm). The phase control consists of
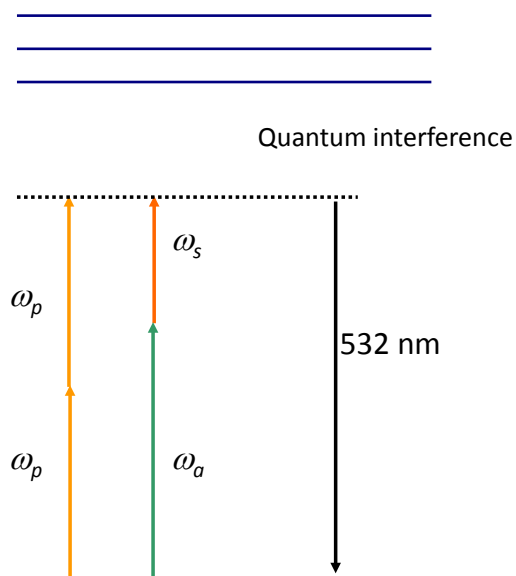
Figure 5.8 Two channels through which 532 nm radiation can be generated by our experiment's output. 532 nm light is generated through second harmonic generation and sum frequency generation. As we adjust the phase of one of the sidebands these processes will interfere and reveal the level of coherence between the three wavelengths involved in the nonlinear process.

a glass slide which can be rotated with an actuator, changing the beam path length of the sideband. The Stokes beam was chosen for the phase control because it is significantly more powerful than the anti-Stokes beam. After the appropriate phase and amplitude adjustments, the beams are reflected and recombined by the same prism.

The beams are then focused by an achromatic lens onto a Beta-Barium-Borate (BBO) crystal. The beams are focused to a 70 μm spot size and great care is taken to ensure that they all overlap at the crystal position. In order to avoid phase mismatch as the beams propagate through the nonlinear crystal we use an ultra-thin crystal with a thickness of 10 μm. At the BBO crystal we measure the powers of the beams to be 39.4 mW (Stokes), 5.61 mW (pump), and 38 μW (anti-Stokes) and the waists to be $W_{\text{Stokes}} = 36\mu$m, $W_{\text{pump}} = 33\mu$m, and $W_{\text{anti-Stokes}} = 30\mu$m.

In order to make the two interfering nonlinear channels comparable we attenuate the pump by 60 % while leaving the Stokes and anti-Stokes beams alone. It is important to note that we do not attenuate the Stokes beam to make its power more comparable to the anti-Stokes power. Because
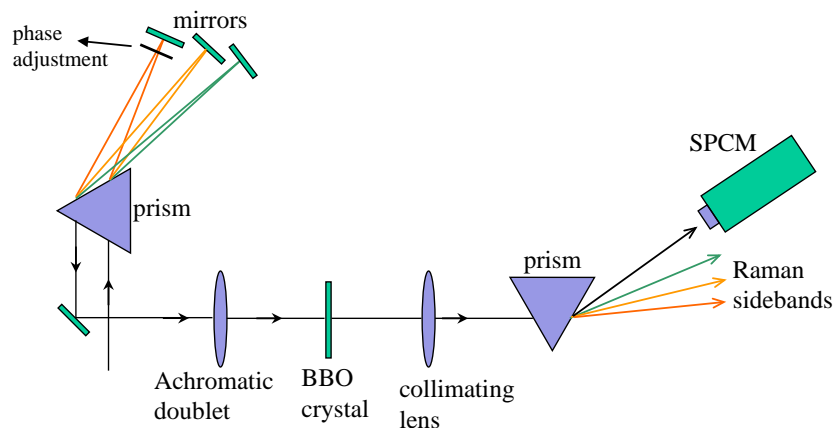
Figure 5.9 Experimental setup for measuring the beam coherence. The input radiation is straight from the D_2-filled cavity.

the interference is based on the electric fields of the beams, see eqn. 5.3, we can still see large

contrast even given a significant power imbalance.
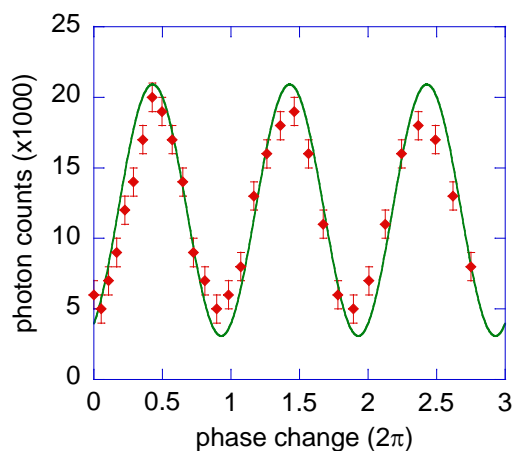
Figure 5.10 The number of 532 nm photons per second detected at the single photon counting moudle as a function of the introduced phase change. We observe sinusoidal variation with a large contrast. The solid line is a numerical calculation based on the measured power values and the beam sizes of the three Raman beams. The contrast of the theoretical curve is calculated without any adjustable parameters.

After the crystal, the beams are once again split by a prism. All the generated beams are

blocked and we measure the light at 532 nm with a single photon counting module. The results of

our measurements are shown in figure 5.10. The number of photon counts per second is shown as a

function of the phase shift of the Stokes beam. The solid line in figure 5.10 is a theoretical calculation based on the process described in equation 5.3 and the measured beam sizes and powers. Only the initial relative phase and absolute vertical scaling are adjusted in this plot; the contrast between these interference fringes is calculated without any adjustable parameters. Clearly our data agrees very well with the theoretical case, which shows almost perfect mutual phase coherence.
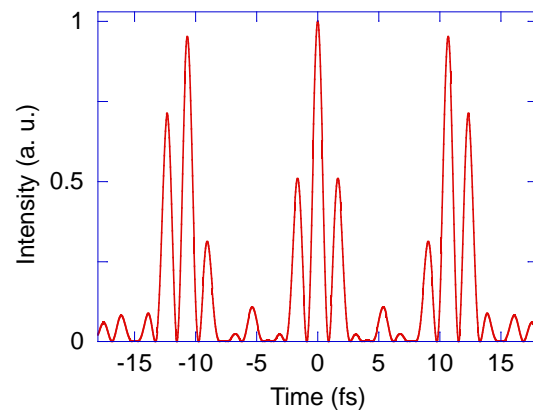
Figure 5.11 The intensity of the inferred synthesized temporal waveform when the spectrum is phase-locked and the amplitudes of the three beams are adjusted to be equal. A near single-cycle optical waveform with a repetition period of 11 femtoseconds is formed. Since the absolute frequencies of the beams are not a multiple of their frequency difference the carrier-envelope phase changes at every period. Since the waveform is synthesized by three kHz-level-linewidth CW beams, it maintains its structure without significant change for about 100 μs.

We have shown that we have very good phase coherence between the beams and the ability to control the amplitude and relative phase of the sidebands. This allows us to infer the ability to synthesize any waveform within the capabilities of the spectrum. For example, proper phase adjustment of the sidebands allows us to modulate the phase or amplitude of the 1064 nm pump beam at 90 THz, nearly 3 orders of magnitude faster than state-of-the-art electro-optic modulators. By setting all the amplitudes equal to one another and phase locking the beams we would be able to generate a near single-cycle pulse with a repetition period of 11 femtoseconds (see figure 5.11). The three frequencies that create this time waveform have an absolute linewidth that is determined by the high-finesse cavity, which is on the 10 kHz level. The very narrow linewidth of the spectral

components allows this temporal waveform to maintain its structure without significant change for about 100 μs.

Chapter 6

Cooling the chamber

Much of the previous work in stimulated Raman scattering has been done with pulsed pump and Stokes lasers. In these pulsed laser experiments, an important step in generating near maximum coherence between the molecular states is cooling the D_2 to 77 K with liquid nitrogen [57, 7]. Cooling the molecules significantly increases the efficiency of the Raman process, as will be discussed in section 6.1. In a pulsed laser experimental setup, the gas-filled chamber is significantly less complicated; it is essentially a steel tube with windows and an input port for D_2. This allows cooling to be straightforward with minimal modification to the gas chamber. In optical cavity-based schemes, however, the D_2-filled chamber also houses the cavity mirrors which are extremely sensitive to misalignment. We have successfully designed an experimental chamber which can be cooled to liquid N_2 temperatures while still allowing for a stable cavity lock. The design considerations and procedures for locking the cavity are described in section 6.2.

6.1   Deuterium at 77 K

Cooling the D_2 is useful for our experiments for multiple reasons. One of the main improvements comes from the redistribution of the molecular population in the rovibrational states. The energy difference between the lowest vibrational states of D_2 is 90 THz. Such a large energy difference means that even at room temperature the fractional population of molecules in the $\nu = 1$ level is 6×10^{-7}. Cooling the gas changes this fractional population to 5.2×10^{-25}, but because the population was so small to begin with this doesn't have much of an effect the Raman process. The redistribution of population in the rotational states, however, does have a significant effect.
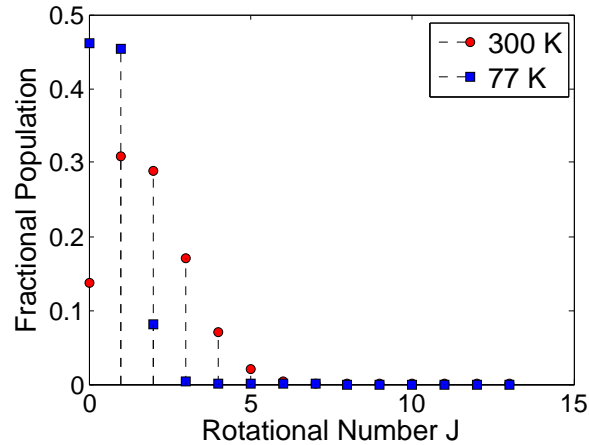
Figure 6.1 Comparison of the distribution of molecules in the rotational states of the $\nu = 0$ vibrational state of deuterium

Figure 6.1 shows the statistical distribution of molecules at room temperature and at liquid N_2 temperature in the zeroth vibrational state. At room temperature the population is relatively evenly spread among the four lowest rotational states. By cooling the deuterium we push most of the population into the two lowest rotational states. This is beneficial because it increases the number of molecules in the Raman process. For instance, experiments using $|\nu = 0, J = 0\rangle$ as the initial state will see a factor of 3 improvement in the effect because of the increase in population in the initial state.

Cooling the deuterium has additional benefits for vibrational Raman experiments. The Raman linewidth for $|\nu = 0, J = 0\rangle \to |\nu = 1, J = 0\rangle$ transitions is determined primarily by the Doppler linewidth ($\Delta\omega_{1/2}$) given by equation 6.1 [58].

$$\Delta\omega_{1/2} = \sqrt{\frac{8\ln(2)\kappa T}{mc^2}}(\omega_{\nu=1} - \omega_{\nu=0}) \tag{6.1}$$

At room temperature, the Doppler linewidth is 532 MHz. Cooling the deuterium decreases that linewidth to 260 MHz. Looking at figure 6.2, the benefit of this is clear. By picturing the Raman linewidth as the gain profile for a Stokes laser we can see that halving the Raman linewidth increases the peak Raman gain by a factor of 2. This, coupled with redistribution of the molecular

population should give a factor of 6 increase in efficiency for a purely vibrational process on the $|\nu = 0, J = 0\rangle \rightarrow |\nu = 1, J = 0\rangle$ transition.
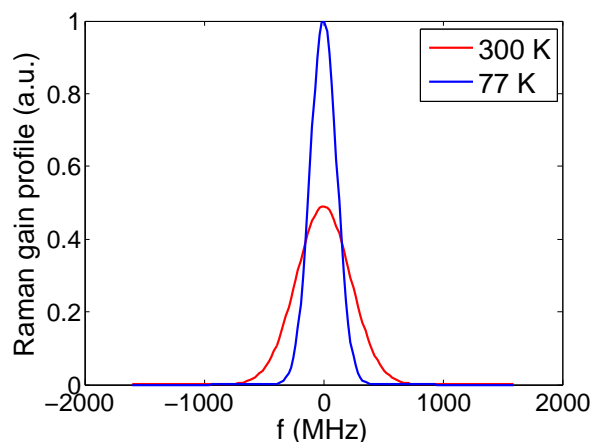
Figure 6.2 Cooling the chamber slows the molecules. This halves the Doppler linewidth and increases the peak Raman gain by a factor of 2.

6.2 Chamber design

Figure 6.3 shows schematic of our experimental cryogenic D_2 chamber. The entire chamber is stainless steel; stainless steel was chosen because of its durability and low thermal conductivity. The D_2 chamber consists of a 75 cm long, 5 cm inner diameter tube with NW50 KF flanges welded to each end. A D_2 input tube and an electrical feedthrough port are welded to the chamber and also use standard KF connections. KF connections are used in all parts of this chamber to allow as much flexibility as possible and to make connections quick, easy, and reliable down to 10^{-8} torr. In our current setup, swagelock connections outside the cavity itself prevent us from dropping the pressure past 100 mtorr; the swagelock can be replaced with higher quality connections should we need to improve the cavity evacuation.

A 45 cm long N_2 reservoir is welded to the central region of the D_2 tube. This reservoir has an input tube and a venting tube. The input tube is sufficiently wide that one can simply pour liquid N_2 into the reservoir from a dewar. After the N_2 is poured, the input tube is capped off and the N_2 vents through a long foam tube attached to the venting tube; the foam tube allows the N_2 vapor to
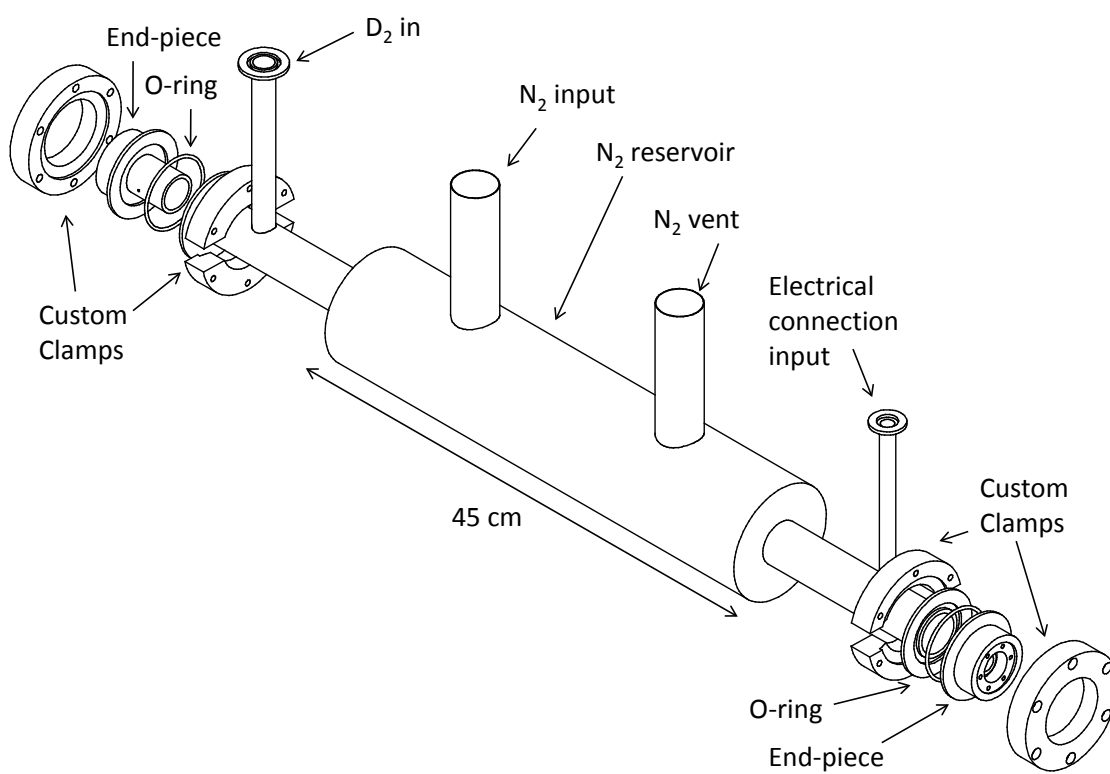
Figure 6.3 General layout of cryogenic experimental chamber (to scale).

Retaining Ring

Window

Mirror

O-rings
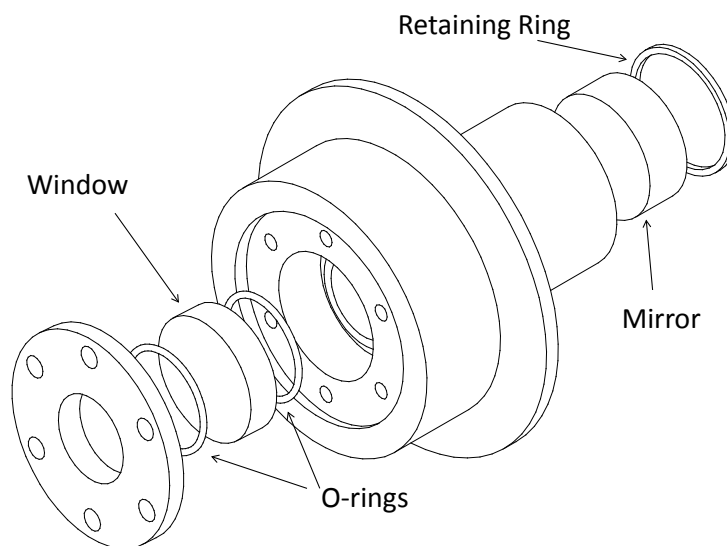
Figure 6.4 Closer view of the endpiece that houses the mirrors and windows.

escape far from the cavity and optical table. The reservoir is insulated with a roughly 2 cm thick layer of aerogel, which has a thermal conductivity of $0.0098 \frac{W}{m \cdot K}$ at liquid nitrogen temperatures.

The cavity mirrors and input windows are held in stainless steel end-pieces which are machined to mate with NW50 KF flanges (see figure 6.4). Because this connection is compatible with KF sized components we have the flexibility to use a range of seals (viton, indium, aluminum, etc.) and clamps. The flexibility at this interface was very important as we were developing methods to overcome cavity warping from rapid cooling of the cavity. A piezo is epoxied to one end-piece and holds one cavity mirror while the other mirror is held by a retaining ring in a recessed, threaded bore. AR coated windows seated on viton o-rings form the final seal of the cavity. In order to ensure that there are no pockets of air within the vacuum chamber, we drill small holes in the mirror holders between the mirrors and the chamber windows.

Many factors must be considered when designing such a chamber. Preventing condensation, minimizing N_2 boil off to prevent disruptive vibrations, and compensating for thermal contraction and warping as the cavity is cooled are some of the main technical hurdles in the chamber development.

The first step to designing the cavity is to eliminate any condensation on the input windows of the cavity. We approach this problem by careful numerical simulations of heat transfer through stainless steel in air. To model this system we use a finite difference technique. We analyze the section of the cavity from the N_2 reservoir to the NW50 flange and model the cavity as an evacuated stainless steel tube with one end held at 77 K. One section of the tube is insulated (corresponding to the aerogel insulation) and the other is heated by convection from the room temperature air around the cylinder. We calculate the convection coefficient to be $8\frac{W}{m^2K}$ using the Nusselt number given by the following expression (6.2), appropriate for horizontal cylindrical systems [59].

$$Nu = \left(0.6 + \frac{0.387Ra^{1/6}}{\left[1 + \left(\frac{0.559}{Pr}\right)^{9/16}\right]^{8/27}}\right)^2 \tag{6.2}$$

In this expression Pr is the Prandtl number, which depends on the thermal properties of the steel and air, and Ra is the Rayleigh number, which characterizes the degree to which the air at the metal surface is laminar or turbulent. Given this convection coefficient, the results of our simulations are shown in figure 6.5.
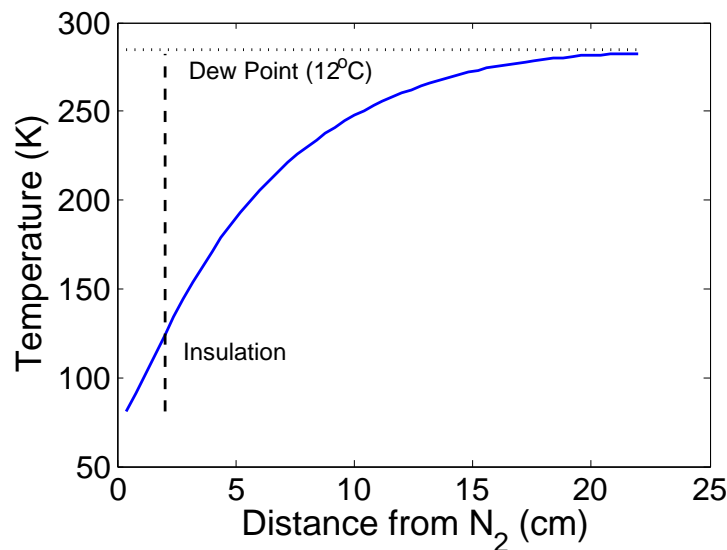
Figure 6.5 Temperature distribution on cylinder held at liquid nitrogen temperature at one end with 2 cm of insulation.

Given the calculated temperature distribution we decided that the tube had to extend at least 16 cm from the N_2 reservoir wall. Although this distance is shown to be below the dew point in figure 6.5 there will be additional heat transferred to the tube through the aluminum clamps that secure the cavity to the optical table. There is also ample space to add heating elements to the tube, should the condensation be worse than expected. In practice we see frost extend to the aluminum clamp and not beyond; there is no need for any heating elements and the NW50 flange face is at room temperature, allowing us to use viton o-rings.

While the cavity design prevents problems due to condensation, mirror misalignment due to thermal contraction of the steel when adding liquid N_2 significantly complicates coupling to the optical cavity. Mirror misalignment of even 10 mrad can severely disrupt the cavity coupling so it is necessary to have some form of control over the pitch of the cavity mirrors after the cavity cools to its steady state. We gain this control using custom aluminum KF clamps. The clamps are machined to fit to an NW50 flange and have 6 concentric 1/4-20 screw holes (see figure 6.3). By tightening or loosening the screws on these clamps we control the pitch of the endpiece and, therefore, the cavity mirror. To ensure that we can consistently orient the mirrors in the same way we reflect a 1064 nm laser beam from the back surface of each mirror and propagate the beam over 6 m to a target. Each time we cool the cavity from room temperature we adjust the pitch of the cavity mirrors with the custom clamps such that the beams hit the target. This method allows us to get ~ 1 mrad precision when moving the mirrors and allows us to very consistently repeat the coupling to the cavity day after day.

Chapter 7

Multiple-Order Rotational Raman generation at 77 K

After cooling the deuterium, we notice a significant improvement in stimulated Stokes generation. In our room temperature rotational Raman generation experiments we were only able to generate one Stokes beam from pressures of .1 atm up to 1 atm. After cooling the cavity we are able to generate up to 5 Stokes beams on the $|\nu = 0, J = 0\rangle \rightarrow |\nu = 0, J = 2\rangle$ transition and a strong (~ 1 mW) anti-Stokes beam as well. In addition to generating exclusively $|\nu = 0, J = 0\rangle \rightarrow |\nu = 0, J = 2\rangle$ Stokes beams, we are able to generate a mixture of $|\nu = 0, J = 0\rangle \rightarrow |\nu = 0, J = 2\rangle$ and $|\nu = 0, J = 1\rangle \rightarrow |\nu = 0, J = 3\rangle$ Stokes and anti-Stokes beams as well, giving us up to ~ 12 generated beams from our single pump at 1064 nm.

7.1 Experimental Setup

The experimental setup is virtually the same as that in our vibrational Raman generation experiments; we use a linearly polarized 1064 nm pump beam that reaches CW powers of 20 W. The key difference is the new, liquid N_2-cooled cavity. The cavity length is extended to 75 cm, from 27 cm in our previous vibrational experiments, and the $R = 50$ cm cavity mirrors are replaced with $R = 100$ cm cavity mirrors.

7.2 Results

One of the main motivations for cooling the cavity is to increase the coherence between the ground and first vibrational states of deuterium. We are especially interested in this transition due to its large transition frequency of 90 THz. We are able to produce vibrational Stokes and anti-Stokes

beams, see figure 7.1, but thus far we have been unable to generate powers comparable to our room temperature vibrational Raman experiments because much of the power goes simultaneously into the rotational Raman transitions, which is also visible in figure 7.1. The highest vibrational anti-Stokes power we were able to generate in our initial experiments was $\sim 40\ \mu$W at 0.3 atm measured at room temperature. At room temperature we did not observe this strong tendency toward simultaneous lasing between rotational and vibrational states. This allowed all the excess pump power to be transferred to the vibrational Stokes beam.
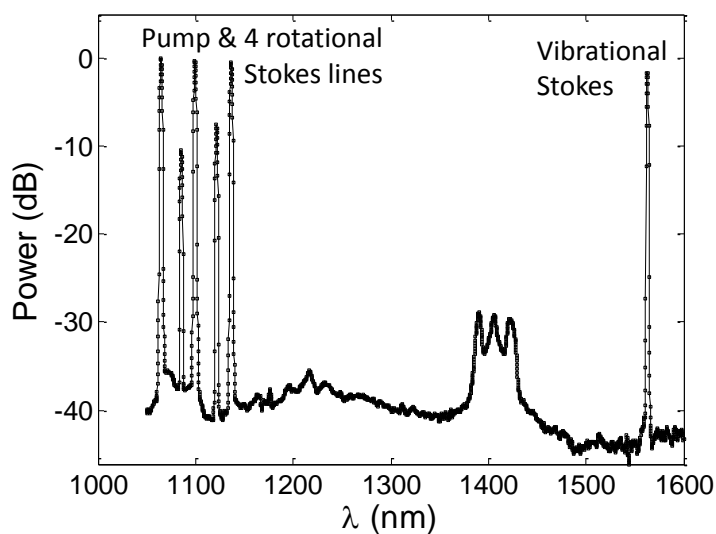
Figure 7.1 Generated spectrum with .3 atm of D_2 (measured at room temperature) and 10 W of input 1064 nm pump power. The vibrational Stokes beam is clearly visible at 1560 nm, but much of the input power is diverted into 4 rotational Raman Stokes beams from 1080 nm to 1140 nm.

While the overall vibrational anti-Stokes power is not particularly higher than in our room temperature experiments, at this point, we do see some initial signs of vibrational coherence in the gas. When generating a vibrational sideband in addition to multiple rotational sidebands, as shown in figure 7.1, close observation reveals multiple beams clustered near 807 nm, the vibrational anti-Stokes wavelength (figure 7.2). These beams can be explained by the vibrational coherence, established by the original pump beam at 1064 nm and the vibrational sideband at 1560 nm. The vibrational coherence established by the pump and vibrational Stokes is imparts 90 THz sidebands on all the rotational Stokes components. The sidebands near 1560 nm are not visible because the
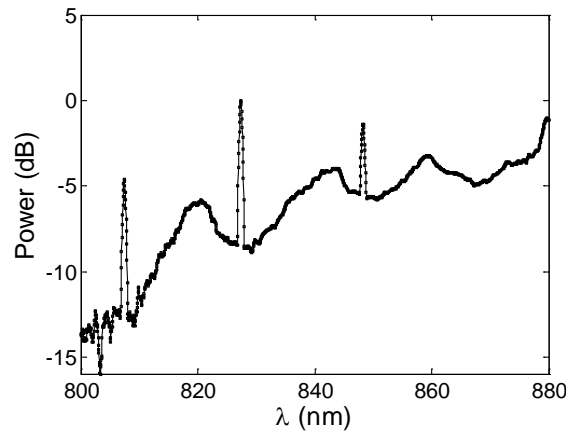
Figure 7.2 Vibrational sidebands generated on rotational Stokes beams. The peak at 807 is the original anti-Stokes beam generated from the coherence and the pump beam. The other two peaks are sidebands on $J = 1 \rightarrow 3$ Stokes beams. It is important to note that they are modulated via coherence that is established between the pump beam at 1064 nm and the vibrational Stokes beam at 1560 nm.

cavity mirrors are highly reflective at those wavelengths, while there is low mirror reflectivity near 807 nm; because these sidebands are generated through a four-wave-mixing process, the sidebands near 1560 nm are not emitted into a cavity mode and therefore the cavity mirrors serve only to attenuate these beams. In figure 7.2 it is the $J = 1 \rightarrow 3$ Stokes beams which are modulated by the vibrational coherence.

Despite our initial lack of success driving the vibrational transition in deuterium at 77 K we have made progress in multiple-order rotational Raman generation. At a pressure of .04 atm (measured at room temperature), more than two orders of magnitude lower than previous cavity-based stimulated Raman scattering experiments, we were able to generate five Stokes beams and two anti-Stokes beams with a combined output power of over 50 mW. For comparison, at a significantly higher pressure, ~ 9.8 atm, Imasaka and colleagues were able to produce two Stokes beams at room temperature [21]. Cooling the cavity dramatically enhances the stimulated Raman scattering process. Figure 7.3 shows the generation at input powers of .31 W and 20 W. This figure shows generation on the $|\nu = 0, J = 0\rangle \rightarrow |\nu = 0, J = 2\rangle$ transition with a transition frequency of 179

cm^{-1} (5.4 THz). We see lasing at a lower threshold than our previous room temperature rotational Raman experiments.

Figure 7.3 Generated beams at a D$_2$ pressure of .04 atm (at room temperature). The left scan shows generation with .31 W input power and the right shows generation with 20 W input power. The pump in both cases is located at 1064 nm. These scans are normalized such that the peak power is located at 0 dBm.

Because the generated Stokes beams are emitted into cavity modes we predict that the Stokes beams are generated through a cascade stimulated Raman scattering process, as observed by Imasaka [21]. This means that the second Stokes beam (at $\sim$ 1107 nm) is not generated through a pure four-wave-mixing process; it is instead a result of the first Stokes beam (at $\sim$ 1080 nm) acting as a new pump beam and generating another Stokes from the rotational state population difference and cavity optical feedback. We believe this to be the case because of the high mirror reflectivities at these wavelengths; a Stokes beam generated from rotational coherence would be independent of the cavity resonance and suffer severe attenuation from cavity mirrors. Because the first four higher order Stokes beams fall within the reflectivity of the mirrors and have power comparable to or greater than the pump we believe each to be resonant with the cavity and therefore generated through a cascade effect. The fifth generated Stokes beam falls outside the reflectivity of the mirrors and, because of the lack of optical feedback, has a power $\sim$ 20 dB lower than the previous Stokes component.
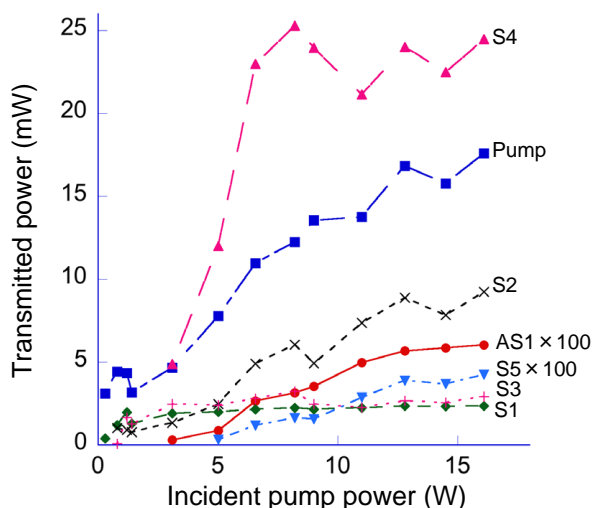
Figure 7.4 Sideband output power as a function of 1064 nm input power at a D_2 pressure of .04 atm. The error bars are omitted to avoid cluttering the figure, we estimate the error to be $\pm$ 15 % primarily due to systematic difficulties in day to day replication of the cavity mirror alignment.

The generated anti-Stokes beams are generated purely from the mixing of the pump and the molecular coherence. There is no rotational state population difference to put gain on the anti-Stokes beam so it will not exhibit the same laser-like behavior of the Stokes wavelengths. The mirrors are reflective at the anti-Stokes wavelength, so the transmitted power, which is 60 μW at 20 W input and a pressure of .04 atm, is only a fraction of the total generated anti-Stokes power inside the cavity.

Figure 7.4 shows the output power of the sidebands at .04 atm, measured at room temperature. The error bars are omitted from this plot to avoid cluttering it. In our experiments we suffer primarily from systematic error due to day to day misalignment of the cavity mirrors. Even very small changes to the pitch of the cavity mirrors can have a large effect on the power generated in the Stokes and anti-Stokes beams and on the spatial profile of the generated beams as well. Small changes to the laser piezo and cavity piezo positions also play a role in the amount of generated sideband power. While in one experimental run the values are consistent, it is more difficult to repeat the results exactly after heating and cooling the cavity again. In light of these systematic difficulties we estimate the error to be roughly $\pm$ 15 %.

By increasing the pressure from .04 atm to .3 atm we see significantly improved anti-Stokes generation. For input powers of 20 W we generate nearly 1 mW of anti-Stokes power on the $J = 0 \rightarrow 2$ transition. The overall total output power is lower than in the lower pressure experiment; we attribute this lower power to degraded cavity coupling due to nonlinear effects from the gas.
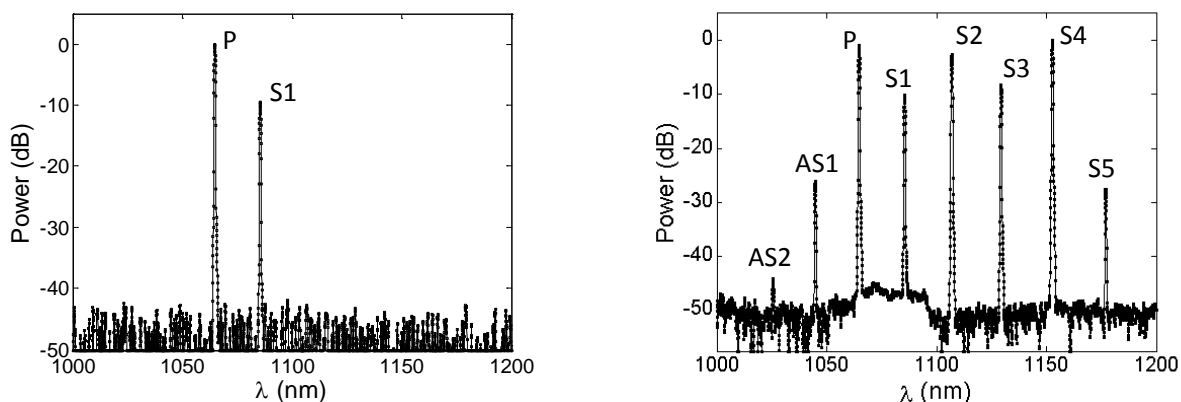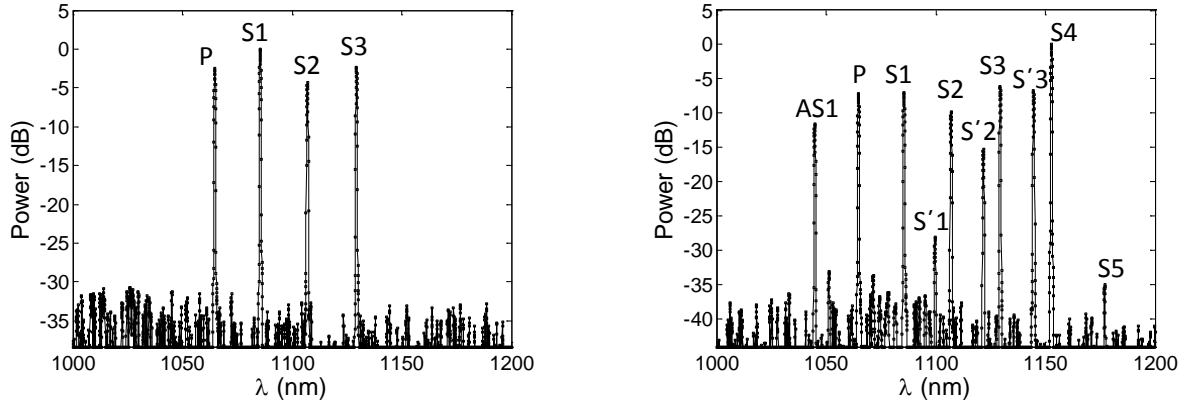

Figure 7.5 Generated beams at a D_2 pressure of .3 atm. The left scan shows generation with .83 W input power and the right shows generation with 20 W input power. The pump in both cases is located at 1064 nm. These scans are normalized such that the peak power is located at 0 dBm. The primed peaks come from the $|\nu = 0, J = 1\rangle \rightarrow |\nu = 0, J = 3\rangle$ process.

At a D_2 pressure of .3 atm, we notice that the $|\nu = 0, J = 1\rangle \rightarrow |\nu = 0, J = 3\rangle$ transition begins to compete with the $|\nu = 0, J = 0\rangle \rightarrow |\nu = 0, J = 2\rangle$ process. The primed peaks in figure 7.5 show this competition. The peak labeled $S'1$ is the first Stokes beam generated from the pump on the $|\nu = 0, J = 1\rangle \rightarrow |\nu = 0, J = 3\rangle$ transition. This Stokes beam then acts as a pump for subsequent $|\nu = 0, J = 0\rangle \rightarrow |\nu = 0, J = 2\rangle$ Stokes beams and anti-Stokes beams; note that after the generation of the first $J = 1 \rightarrow 3$ Stokes, the subsequent primed Stokes beams have the same spacing as those generated from the $J = 0 \rightarrow J = 2$ Stokes. Increasing the pressure from .3 atm has not yielded success as of yet. While we are able to couple light to the cavity, the lock suffers from noise which we believe to be a result of non-linear interactions with the higher gas density in the optical cavity.

Because of the high sensitivity to mirror alignment and position we do have the opportunity to see a wide variety of interesting spatial modes and spectral components of the output. Although

difficult to quantify, we have seen interesting phenomena which may be the subject of future investigation. One such phenomenon is the tendency for the higher order Stokes beams to emit into higher order spatial modes of the cavity causing higher order Stokes beams to have intricate and exotic spatial profiles. Stimulated Raman scattering is maximized when the pump and Stokes beams are both Gaussian because of the overlap of the intensity peaks inside the cavity. To ensure we are coupling the Stokes radiation to the TEM_{00} mode of the cavity we scan the cavity piezo over several transmitted peaks with the high speed feedback activated. This flashes several cavity resonances. We observe the spatial profile of the Stokes beams with an infra-red viewer and make small adjustments to the screws on the custom clamps of the cavity (see section 6.2), changing the orientation of the cavity mirrors. When the Stokes beams are clearly Gaussian and we observe the generation of several Stokes beams we stop adjusting the mirror and re-optimize the coupling to the cavity.
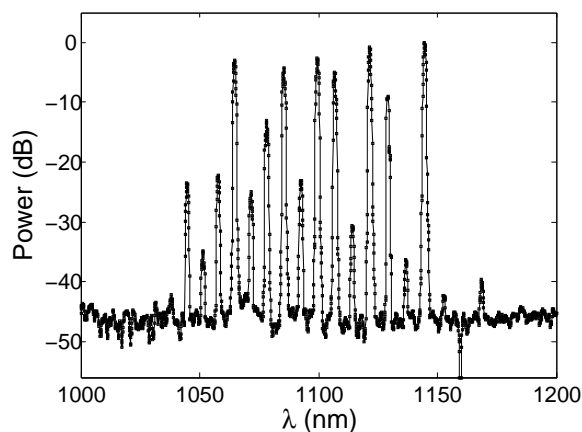
Figure 7.6 Example of rich spectral properties of the output.

Figure 7.6 shows the variety of frequencies that can be generated using this cavity based method (this was taken at .08 atm pressure measured at room temperature and 10 W input). This spectral profile shows several $J = 0 \rightarrow 2$ Stokes beams and $J = 1 \rightarrow 3$ Stokes beams interleaved between them. Several anti-Stokes beams are visible and careful observation of figure 7.6 shows a peak at 1072 nm, which corresponds to the $|\nu = 0, J = 0\rangle \rightarrow |\nu = 0, J = 1\rangle$, which is a forbidden Raman transition for a homonuclear molecule and will certainly be the subject of future study.

Chapter 8

Conclusions

In this thesis we describe the first steps in developing a continuous-wave molecular modulator. The basis of our modulation scheme is to drive a Raman transition in D_2 gas with two intense continuous-wave optical fields that are resonant with the cavity. In each experiment we lock a single pump laser, with upper powers between 20 W and 30 W, to a cavity with a finesse of $\sim$ 20,000. The Stokes field (the second field required to drive the Raman transition) is generated from noise within the cavity after the pump is locked. The molecular coherence established by these beams drives a four-wave-mixing process that produces anti-Stokes radiation.

We have investigated both rotational and vibrational Raman modulation at room temperature and at 77 K. In the case of rotational Raman generation at room temperature, we have generated over 300 mW of Stokes power at low D_2 pressures ($\sim$ 0.1 atm). To our knowledge this is the most Stokes power ever generated in a cavity-based stimulated Raman scattering experiment.

In another room temperature experiment we drive a vibrational Raman transition in D_2 gas, again at pressures less than one atmosphere, and generate coherent sidebands on a 1064 nm pump beam at 807 nm and 1560 nm. Having full control over the relative phase of these spectral components, we achieve 90 THz modulation on the pump beam and can infer the capability to produce temporal waveforms with 1.5 cycle features.

We have, for the first time, carried out cavity-based stimulated Raman scattering experiments at liquid nitrogen temperatures. By designing a cryogenic chamber to house the optical cavity, we are able to significantly improve the efficiency of the nonlinear process under investigation. This improvement is clear as we are able to generate 5 Stokes and 2 anti-Stokes beams (the most ever

for a cavity-based scheme) on a rotational transition in .04 atm of D_2, almost 3 orders of magnitude lower pressure than any other cavity-based experiments.

This thesis also discussed many of the technical details involved in the experiments. One of the main hurdles for an optical cavity-based stimulated Raman scheme is developing a robust locking system to maintain resonance with the cavity for several minutes despite nonlinear effects from the medium, heating of the mirrors, and mechanical vibrations on the optical table. The branches of the feedback have been described in detail and important bandwidth-related considerations discussed as well. Overcoming technical obstacles related to quickly cooling the cavity to liquid nitrogen temperatures have also been explored and many of the considerations that go into the design of a cryogenic cavity have been discussed.
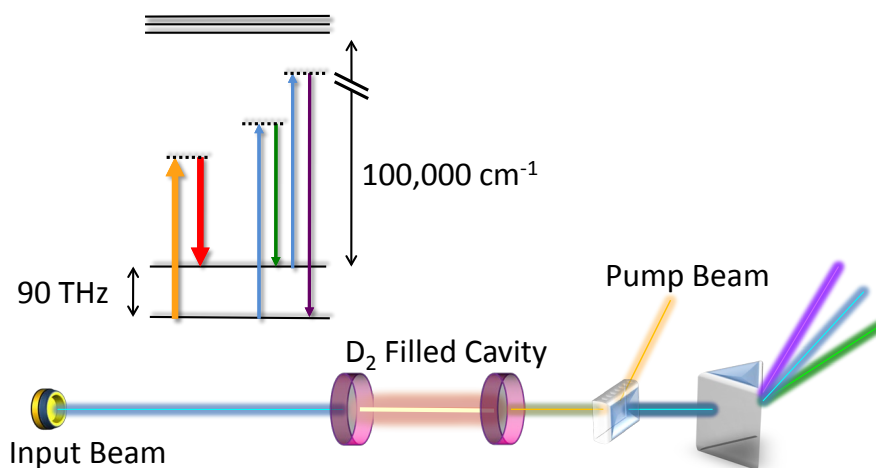
Figure 8.1 Arbitrary input beam is modulated at 90 THz. The pump beam (orange) generates a Stokes beam (red) from noise which then builds up in the cavity. The pump and Stokes beams produce a large molecular coherence, which in turn imparts sidebands on the blue input beam.

Moving forward, there are a number of things to investigate. Ultimately the goal of this project is to produce a continuous wave molecular modulator. Such a modulator can be used to impart 90 THz sidebands on an arbitrary optical field passing through the cavity. The modulator would modulate any wavelength from 10 μm to 100 nm with similar efficiency. Figure 8.1 shows the basic idea for such a modulator. The pump laser (orange) is locked to the optical cavity and a powerful Stokes field builds up from noise (red). These two intense fields produce a large molecular

coherence. A carrier beam at an arbitrary frequency within the frequency window given above will be modulated by the coherence of the molecules.

Applying such a modulator to the output of a Ti:Sapphire laser is depicted in figure 8.2. The 90 THz modulator will significantly broaden the Ti:Sapphire spectrum in a coherent manner. This spectral broadening will allow for the production of much shorter pulses and is the ultimate goal of this molecular modulator project.
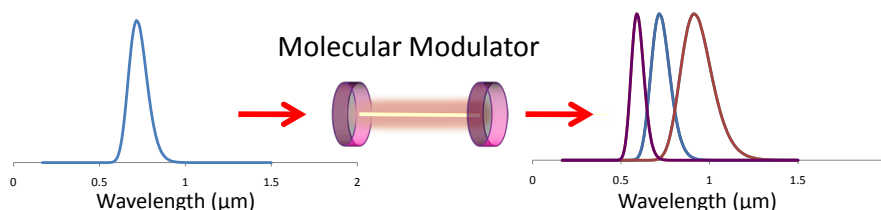
Figure 8.2 A Ti:Sapphire spectrum would be broadened by a 90 THz molecular modulator. The modulator would have the effect of shifting the a portion of the spectrum $\pm$ 90 THz from the unbroadened profile.

In order to create such an efficient modulator we must improve the molecular coherence we are able to achieve. The first step to generating a higher coherence is cooling the deuterium gas, which is currently being investigated. We are interested in increasing the coherence between vibrational states due to the 90 THz modulation frequency associated with it. Our preliminary tests have shown that much of the pump power is diverted into rotational Raman generation rather than vibrational. By experimenting with different D_2 pressures and possibly introducing a buffer gas to allow fine tuning of the two-photon detuning we hope to be able to generate a higher coherence than in our room temperature vibrational experiments.

One other route to achieving higher vibrational coherence is to introduce an additional laser at the Stokes wavelength. Simultaneously locking a 30 W 1555 nm beam and a 30 W 1060 nm beam (both of which we have experimental experience with) to the high finesse cavity filled with very low pressure D_2 could be helpful in driving the molecules appropriately. By lowering the D_2 pressure to the point that the Raman lasing threshold is very high (higher intra-cavity pump power at the expense of generated Stokes power) and locking an additional beam at the Stokes frequency

to make up for the lack of generated Stokes power, we could have both a very high intensity pump and Stokes beam driving the molecules. This higher intensity would generate a larger coherence, but at the expense of gas density. Finding the optimum balance between generated coherence and molecular density will be the subject of future research.

In addition to efforts to increase the vibrational coherence, there are a number of other interesting effects to investigate. For example, developing a framework to explain mode competition in multiple-order Raman generation and its susceptibility to mirror misalignment could be an instructive and useful endeavor. One such investigation may include the exploration of the exotic spatial structure of the higher order Stokes beams.

Investigating rotational anti-Stokes generation by systematically changing the pump laser frequency or, possibly, introducing a buffer gas for dispersion-based tuning would also help characterize the rotational coherence of the molecules; because the rotational anti-Stokes line falls within the high-reflectivity region of the cavity, changing the frequency of the anti-Stokes beam or the dispersion of the medium could allow us tune the anti-Stokes beam across resonances with the cavity and much more effectively characterize the rotational coherence of the molecules and the role played by the optical cavity in anti-Stokes generation.

The frequency range spanned by the multiple rotational Raman sidebands shown in figure 7.3 has the capacity to produce pulses with a 20 fs duration. Because these sidebands are generated through a cascade process, the frequencies are not equally spaced, as they would be had they been generated purely through four-wave-mixing; their frequencies can vary by as much as a free spectral range which, in this case, is 200 MHz. To synthesize a pulse from these spectral components each beam would require some form of frequency tuning element in its path. While this complication is a severe drawback to this type of pulse generation it is a possible avenue through which to extend the work presented in this thesis.

While the focus of future research will be on increasing the vibrational coherence of the molecules and improving the efficiency of the four-wave-mixing process with the end goal of producing ultrashort optical pulses, the capacity to lock high power continuous-wave lasers to a

cryogenic gas-filled optical cavity provides a foundation for a wide range of interesting investigations and applications in its own right.

LIST OF REFERENCES

[1] L. Meng, J. Brasseur, and D. Neumann, Opt. Express **13**, 10085 (2005).

[2] P. Moulton, JOSA B **3**, 125 (1986).

[3] A. Stingl, M. Lenzner, C. Spielmann, F. Krausz, and R. Szipöcs, Opt. Lett. **20**, 602 (1995).

[4] R. Ell *et al.*, Opt. Lett. **26**, 373 (2001).

[5] A. Weiner, *Ultrafast Optics* (John Wiley & Sons, Inc., 2009).

[6] P. Brumer and M. Shapiro, Annual Review of Physical Chemistry **43**, 257 (1992).

[7] M. Y. Shverdin, D. R. Walker, D. D. Yavuz, G. Y. Yin, and S. E. Harris, Phys. Rev. Lett. **94**, 033904 (2005).

[8] T. Imasaka, S. Yamanishi, S. Kawasaki, and N. Ishibashi, App. Opt. **32**, 6633 (1993).

[9] A. E. Kaplan, Phys. Rev. Lett. **73**, 1243 (1994).

[10] N. Zhavoronkov and G. Korn, Phys. Rev. Lett. **88**, 203901 (2002).

[11] H. Kawano, Y. Hirakawa, and T. Imasaka, IEEE J. Quantum Electon. **34**, 260 (1998).

[12] J. Q. Liang, M. Katsuragawa, F. Kien, and K. Hakuta, Phys. Rev. Lett. **85**, 2474 (2000).

[13] A. V. Sokolov, D. R. Walker, D. D. Yavuz, G. Y. Yin, and S. E. Harris, Phys. Rev. Lett. **85**, 562 (2000).

[14] D. Yavuz, *A Raman approach for generating ultrashort pulses*, PhD thesis, Stanford University, 2003.

[15] W. Chen *et al.*, Phys. Rev. Lett. **100**, 163906 (2008).

[16] Z.-M. Hsieh *et al.*, Phys. Rev. Lett. **102**, 213902 (2009).

[17] D. Yavuz, D. Walker, G. Yin, and S. Harris, Opt. Lett. **27**, 769 (2002).

[18] D. D. Yavuz, Phys. Rev. A **76**, 011805(R) (2007).

[19] K. Ihara *et al.*, App. Phys. Lett. **88**, 074101 (2006).

[20] K. Shinzen, Y. Hirakawa, and T. Imasaka, Phys. Rev. Lett. **87**, 223901 (2001).

[21] S.-i. Zaitsu, H. Izaki, and T. Imasaka, Phys. Rev. Lett. **100**, 073901 (2008).

[22] K. S. Repasky, J. K. Brasseur, L. Meng, and J. L. Carlsten, J. Opt. Soc. Am. B **15**, 1667 (1998).

[23] J. K. Brasseur, P. A. Roos, L. S. Meng, and J. L. Carlsten, J. Opt. Soc. Am. B **17**, 1229 (2000).

[24] J. C. Bienfang, W. Rudolph, P. A. Roos, L. S. Meng, and J. L. Carlsten, J. Opt. Soc. Am. B **19**, 1318 (2002).

[25] P. A. Roos, J. K. Brasseur, and J. L. Carlsten, J. Opt. Soc. Am. B **17**, 758 (2000).

[26] P. A. Roos, L. S. Meng, S. K. Murphy, and J. L. Carlsten, J. Opt. Soc. Am. B **21**, 357 (2004).

[27] P. A. Roos, L. S. Meng, and J. L. Carlsten, J. Opt. Soc. Am. B **19**, 1310 (2002).

[28] Y. Xiong, S. Murphy, J. L. Carlsten, and K. Repasky, J. Opt. Soc. Am. B **24**, 2055 (2007).

[29] F. Benabid, G. Bouwmans, J. Knight, and P. Russel, Phys. Rev. Lett. **93**, 123903 (2004).

[30] F. Benabid, G. Antonopoulos, J. Knight, and P.St.J.Russel, Phys. Rev. Lett. **95**, 213903 (2007).

[31] F. Couny, F. Benabid, and P. S. Light, Phys. Rev. Lett. **99**, 143903 (2007).

[32] Y. Wang, C. Wu, F. Couny, M. Raymer, and F. Benabid, Phys. Rev. Lett. **105**, 123603 (2010).

[33] B. Unks, N. Proite, and D. Yavuz, Rev. Sci. Instum. **78**, 083108 (2007).

[34] S. Harris and A. Sokolov, Phys. Rev. Lett. **81**, 2894 (1998).

[35] S. Huang, W. Chen, and A. Kung, Phys. Rev. A **74**, 063825 (2006).

[36] R. Boyd, *Nonlinear Optics* (Elsevier, Inc., 2008).

[37] K. S. Repasky, L. Meng, J. K. Brasseur, J. L. Carlsten, and R. C. Swanson, J. Opt. Soc. Am. B **16**, 717 (1999).

[38] S. Harris, Opt. Lett. **19**, 2018 (1994).

[39] J. Sakurai, *Modern Quantum Mechanics* (Addison-Wesley Publishing Inc., 1994).

[40] J. T. Green, D. E. Sikes, and D. D. Yavuz, Opt. Lett. **34**, 2563 (2009).

[41] J. K. Brasseur, P. A. Roos, K. S. Repasky, and J. L. Carlsten, J. Opt. Soc. Am. B **17**, 1223 (2000).

[42] N. Proite, B. Unks, J. Green, and D. Yavuz, Phys. Rev. A **77**, 023819 (2008).

[43] D. Yavuz, Phys. Rev. A **75**, 041802(R) (2007).

[44] H. Edwards, D. Long, and G. Sherwood, J. Raman Spect. **22**, 607 (1991).

[45] D. Russel and W. Roh, J. Mol. Spect. **124**, 240 (1987).

[46] A. Siegman, *Lasers* (University Science Books, 1986).

[47] R. Drever *et al.*, Appl. Phys. B **31** (1983).

[48] E. Black, Am. J. Phys. **69**, 79 (2001).

[49] A. Yariv and P. Yeh, *Photonics: Optical Electronics in Modern Communications, 6th Ed.* (Oxford University Press, 2007).

[50] A. Arnold, J. Wilson, and M. Boshier, Rev. Sci. Instrum. **69**, 1236 (1998).

[51] C. Hawthorn, K. Weber, and R. Scholten, Rev. Sci. Instrum. **72**, 4477 (2001).

[52] J. DiStefano, A. Stubberud, and I. Williams, *Feedback and Control Systems, 2nd Ed.* (McGraw-Hill, 1995).

[53] R. Fox, C. Oates, and L. Hollberg, Experimental methods in the physical sciences, chap. Cavity-Enhanced Spectroscopies, Elsevier Science, 2002.

[54] G. Herzberg, *Molecular Spectra and Molecular Structure I. Spectra of Diatomic Molecules* (D. Van Nostrand Company, Inc., 1950).

[55] J. Brasseur *et al.*, Appl. Opt. **43**, 1162 (2004).

[56] J. T. Green, J. J. Weber, and D. D. Yavuz, Phys. Rev. A **82**, 011805 (2010).

[57] T. Suzuki, M. Hirai, and M. Katsuragawa, Phys. Rev. Lett. **101**, 243602 (2008).

[58] H. Metcalf and P. van der Straten, *Laser Cooling and Trapping* (Springer, 1999).

[59] F. Incropera and D. DeWitt, *Fundamentals of Heat and Mass Transfer, 3rd Ed.* (John Wiley and Sons, 1990).

[60] A. Allison and A. Dalgarno, Atomic Data **1**, 289 (1970).

[61] A. Sokolov, D. Yavuz, and S. Harris, Opt. Lett. **24**, 557 (1999).

Appendix A: Effective Hamiltonian and Propagation Equations

A.1   Effective Hamiltonian

The Hamiltonian that describes the Raman system is a 2×2 matrix. To derive this effective Hamiltonian (H_{eff}) we begin with the full Hamiltonian of the system. $|a\rangle$ corresponds to the ground state, $|b\rangle$ corresponds to an excited metastable state, and $|i\rangle$ are an arbitrary number of upper states from which the lasers are very far detuned.

Only dipole transitions are allowed in this derivation. In the system we consider, transitions between a and b are dipole forbidden, but transitions from either state up to an i state are allowed.

$$\hat{H} = \hat{H}_0 + \hat{H}_{interaction} \tag{A.1}$$

where

$$\hat{H}_0 = \hbar\omega_a |a\rangle \langle a| + \hbar\omega_b |b\rangle \langle b| + \sum_i \hbar\omega_i |i\rangle \langle i| \tag{A.2}$$

$$\begin{aligned} \hat{H}_{interaction} &= -E(t)\hat{P} \\ &= -E(t)\left(\sum_i \left(\mu_{ai} |a\rangle \langle i| + \mu_{bi} |b\rangle \langle i| + \mu_{ia}^\star |i\rangle \langle a| + \mu_{ib}^\star |i\rangle \langle b| \right) \right) \end{aligned} \tag{A.3}$$

This is the Hamiltonian we will use in the Schrödinger equation:

$$i\hbar \frac{\mathrm{d}}{\mathrm{d}t} |\psi\rangle = \left(\hat{H}_0 + \hat{H}_{int} \right) |\psi\rangle \tag{A.4}$$

Where $|\psi\rangle$ is the state of the atom/molecule which can be expressed in terms of energy eigenstates:

$$|\psi(t)\rangle = c_a(t)\mathrm{e}^{-i\omega_a t} |a\rangle + c_b(t)\mathrm{e}^{-i\omega_b t} |b\rangle + \sum_i c_i(t)\mathrm{e}^{-i\omega_i t} |i\rangle \tag{A.5}$$

Plugging $|\psi(t)\rangle$ into the Schrödinger equation, we get differential equations for the time evolution of c_a, c_b, and c_i. Below are expressions for the right and left hand sides (RHS and LHS) of the Schrödinger equation.

RHS:

$$
\begin{aligned}
\hat{H} \, |\psi(t)\rangle \;=\;& \left(\hbar\omega_a c_a(t)\mathrm{e}^{-i\omega_a t} - E(t)\sum_i c_i(t)\mathrm{e}^{-i\omega_i t}\mu_{ai} \right) |a\rangle \\
+\;& \left(\hbar\omega_b c_b(t)\mathrm{e}^{-i\omega_b t} - E(t)\sum_i c_i(t)\mathrm{e}^{-i\omega_i t}\mu_{bi} \right) |b\rangle \\
+\;& \sum \left(\hbar\omega_i c_i(t)\mathrm{e}^{-i\omega_i t} - E(t)\left(\mu_{ai}^{\star} c_a(t)\mathrm{e}^{-i\omega_a t} + \mu_{bi}^{\star} c_b(t)\mathrm{e}^{-i\omega_b t} \right) \right) |i\rangle
\end{aligned}
$$

LHS:

$$
\begin{aligned}
i\hbar\frac{\mathrm{d}}{\mathrm{d}t}\,|\psi(t)\rangle \;=\;& i\hbar\left(\frac{\mathrm{d}c_a(t)}{\mathrm{d}t}\mathrm{e}^{-i\omega_a t} - i\omega_a c_a(t)\mathrm{e}^{-i\omega_a t} \right) |a\rangle \\
+\;& i\hbar\left(\frac{\mathrm{d}c_b(t)}{\mathrm{d}t}\mathrm{e}^{-i\omega_b t} - i\omega_b c_b(t)\mathrm{e}^{-i\omega_b t} \right) |b\rangle \\
+\;& \sum_i i\hbar\left(\frac{\mathrm{d}c_i(t)}{\mathrm{d}t}\mathrm{e}^{-i\omega_i t} - i\omega_i c_i(t)\mathrm{e}^{-i\omega_i t} \right) |i\rangle
\end{aligned}
$$

With the left and right hand sides evaluated we can match coefficients of eigenkets to form the differential equations for c_a, c_b, and c_i. In this derivation we assume a Raman linewidth of zero. In chapter 2 a decay term is added to the system phenomenologically to account for a non-zero linewidth.

$|a\rangle$:

$$
\frac{\mathrm{d}c_a(t)}{\mathrm{d}t} = E(t)\frac{i}{\hbar}\sum_i c_i\mu_{ai}\mathrm{e}^{i(\omega_a-\omega_i)t} \tag{A.6}
$$

$|b\rangle$:

$$
\frac{\mathrm{d}c_b(t)}{\mathrm{d}t} = E(t)\frac{i}{\hbar}\sum_i c_i\mu_{bi}\mathrm{e}^{i(\omega_b-\omega_i)t} \tag{A.7}
$$

$|i\rangle$:

$$\frac{\mathrm{d}c_i(t)}{\mathrm{d}t} = E(t)\frac{i}{\hbar}\left(c_a\mu_{ai}^\star\mathrm{e}^{i(\omega_i-\omega_a)t} + c_b\mu_{bi}^\star\mathrm{e}^{i(\omega_i-\omega_b)t}\right) \tag{A.8}$$

Now we can define the driving electric field $E(t)$. To begin with we express the electric field in terms of it's frequency components. The electric field will be a sum of beams with frequency components spaced by the frequency of the Raman transition.

$$E(t) = \frac{1}{2}\left(\sum_q E_q\mathrm{e}^{i(\omega_q t - k_q z)} + c.c.\right) \tag{A.9}$$

This gives us

$$\begin{aligned}\frac{\mathrm{d}c_a}{\mathrm{d}t} &= \frac{i}{2\hbar}\sum_q\sum_i E_q c_i\mu_{ai}\mathrm{e}^{i(\omega_q t - k_q z)}\mathrm{e}^{i(\omega_a-\omega_i)t} \\ &+ \frac{i}{2\hbar}\sum_q\sum_i E_q^\star c_i\mu_{ai}\mathrm{e}^{-i(\omega_q t - k_q z)}\mathrm{e}^{i(\omega_a-\omega_i)t}\end{aligned} \tag{A.10}$$

$$\begin{aligned}\frac{\mathrm{d}c_b}{\mathrm{d}t} &= \frac{i}{2\hbar}\sum_q\sum_i E_q c_i\mu_{bi}\mathrm{e}^{i(\omega_q t - k_q z)}\mathrm{e}^{i(\omega_b-\omega_i)t} \\ &+ \frac{i}{2\hbar}\sum_q\sum_i E_q^\star c_i\mu_{bi}\mathrm{e}^{-i(\omega_q t - k_q z)}\mathrm{e}^{i(\omega_b-\omega_i)t}\end{aligned} \tag{A.11}$$

and

$$\begin{aligned}\frac{\mathrm{d}c_i}{\mathrm{d}t} &= \frac{i}{2\hbar}\sum_q E_q c_a\mu_{ai}^\star\mathrm{e}^{i(\omega_q t - k_q z)}\mathrm{e}^{i(\omega_i-\omega_a)t} \\ &+ \frac{i}{2\hbar}\sum_q E_q c_b\mu_{bi}^\star\mathrm{e}^{i(\omega_q t - k_q z)}\mathrm{e}^{i(\omega_i-\omega_b)t} \\ &+ \frac{i}{2\hbar}\sum_q E_q^\star c_a\mu_{ai}^\star\mathrm{e}^{-i(\omega_q t - k_q z)}\mathrm{e}^{i(\omega_i-\omega_a)t} \\ &+ \frac{i}{2\hbar}\sum_q E_q^\star c_b\mu_{bi}^\star\mathrm{e}^{-i(\omega_q t - k_q z)}\mathrm{e}^{i(\omega_i-\omega_b)t}\end{aligned} \tag{A.12}$$

At this point we can use the slowly varying envelope approximation. This approximation is valid because the $c_i(t)$ are varying so much faster than $c_a(t)$ and $c_b(t)$. In this approximation we take $c_{a,b}(t)$ to be a constant and directly integrate the differential equation for $c_i(t)$.

$$
\begin{aligned}
\int_0^t \frac{\mathrm{d}c_i(t')}{\mathrm{d}t'}\mathrm{d}t' \quad &\rightarrow \\
c_i(t) \quad &= \quad \frac{1}{2\hbar}\sum_q \frac{E_q c_a \mu_{ai}^\star}{(\omega_i-\omega_a)+\omega_q}\mathrm{e}^{i(\omega_i-\omega_a+\omega_q)t-ik_q z} \\
&+\frac{1}{2\hbar}\sum_q \frac{E_q c_b \mu_{bi}^\star}{(\omega_i-\omega_b)+\omega_q}\mathrm{e}^{i(\omega_i-\omega_b+\omega_q)t-ik_q z} \\
&+\frac{1}{2\hbar}\sum_q \frac{E_q^\star c_a \mu_{ai}^\star}{(\omega_i-\omega_a)-\omega_q}\mathrm{e}^{i(\omega_i-\omega_a-\omega_q)t+ik_q z} \\
&+\frac{1}{2\hbar}\sum_q \frac{E_q^\star c_b \mu_{bi}^\star}{(\omega_i-\omega_b)-\omega_q}\mathrm{e}^{i(\omega_i-\omega_b-\omega_q)t+ik_q z} \qquad \text{(A.13)}
\end{aligned}
$$

Now that we have an expression for $c_i(t)$, we can plug this into the differential equations for $c_a(t)$ and $c_b(t)$. The number of terms in the ensuing expressions is quite large, but most can be ignored with some important assumptions. We will assume that second harmonic generation is negligible and we will only consider terms that vary in time as follows:

$$
\Delta\omega = (\omega_b-\omega_a)-(\omega_q-\omega_{q-1}) \qquad \text{(A.14)}
$$

Terms varying faster than that are negligible. In light of these approximations, recognizing that $\Delta\omega$ is small compared to $\omega_q, \omega_{q-1}, \omega_a, \omega_b$, and defining $k_m = k_q - k_{q-1}$,

$$
\begin{aligned}
\frac{\mathrm{d}c_a}{\mathrm{d}t} \quad = \quad &\frac{i}{4\hbar^2}\sum_i \sum_q \left[\frac{|E_q|^2|\mu_{ai}|^2}{(\omega_i-\omega_a)-\omega_q}c_a + \frac{|E_q|^2|\mu_{ai}|^2}{(\omega_i-\omega_a)+\omega_q}c_a \right. \\
&+\frac{E_q E_{q-1}^\star \mu_{ai}\mu_{bi}^\star}{(\omega_i-\omega_b)+\omega_q}c_b \mathrm{e}^{-i\Delta\omega t-ik_m z} \\
&\left.+\frac{E_q E_{q-1}^\star \mu_{ai}\mu_{bi}^\star}{(\omega_i-\omega_a)-\omega_q}c_b \mathrm{e}^{-i\Delta\omega t-ik_m z} \right]
\end{aligned}
$$

$$\begin{aligned}
\frac{dc_b}{dt} &= \frac{i}{4\hbar^2} \sum_i \sum_q \left[\frac{|E_q|^2 |\mu_{bi}|^2}{(\omega_i - \omega_b) - \omega_q} c_b + \frac{|E_q|^2 |\mu_{bi}|^2}{(\omega_i - \omega_b) + \omega_q} c_b \right. \\
&\quad + \frac{E_q^\star E_{q-1} \mu_{ai}^\star \mu_{bi}}{(\omega_i - \omega_a) - \omega_q} c_a e^{i\Delta\omega t + ik_m z} \\
&\quad + \left. \frac{E_q^\star E_{q-1} \mu_{ai}^\star \mu_{bi}}{(\omega_i - \omega_b) + \omega_q} c_a e^{i\Delta\omega t + ik_m z} \right]
\end{aligned}$$

At this point, to simplify the expressions, we will introduce a_q, d_q, and b_q:

$$a_q = \frac{1}{2\hbar^2} \sum_i \left(\frac{|\mu_{ai}|^2}{(\omega_i - \omega_a) - \omega_q} + \frac{|\mu_{ai}|^2}{(\omega_i - \omega_a) + \omega_q} \right)$$

$$d_q = \frac{1}{2\hbar^2} \sum_i \left(\frac{|\mu_{bi}|^2}{(\omega_i - \omega_b) - \omega_q} + \frac{|\mu_{bi}|^2}{(\omega_i - \omega_b) + \omega_q} \right)$$

$$b_q = \frac{1}{2\hbar^2} \sum_i \left(\frac{\mu_{ai}\mu_{bi}^\star}{(\omega_i - \omega_a) - \omega_q} + \frac{\mu_{ai}\mu_{bi}^\star}{(\omega_i - \omega_b) + \omega_q} \right)$$

Now the differential equations describing the evolution of $c_a(t)$ and $c_b(t)$ take the following form.

$$\begin{aligned}
\frac{dc_a(t)}{dt} &= \frac{i}{2} \left(\sum_q a_q c_a |E_q|^2 + \sum_q b_q c_b E_q E_{q-1}^\star e^{-i\Delta\omega t - ik_m z} \right) \\
\frac{dc_b(t)}{dt} &= \frac{i}{2} \left(\sum_q d_q c_b |E_q|^2 + \sum_q b_q^\star c_a E_q^\star E_{q-1} e^{-i\Delta\omega t - ik_m z} \right)
\end{aligned} \tag{A.15}$$

To eliminate the oscillating time dependence in the above expression we make a simple transformation:

$$\begin{aligned}
c_a &= \tilde{c}_a; \\
c_b &= \tilde{c}_b e^{i\Delta\omega t + ik_m z}
\end{aligned}$$

Applying this transformation to the differential equations above we get the following

$$\begin{aligned}
\frac{d\tilde{c}_a(t)}{dt} &= \frac{i}{2} \left(\sum_q a_q |E_q|^2 \tilde{c}_a \right) + \frac{i}{2} \left(\sum_q b_q E_q E_{q-1}^\star \tilde{c}_b \right) \\
\frac{d\tilde{c}_b(t)}{dt} &= \frac{i}{2} \left(\sum_q d_q |E_q|^2 \tilde{c}_b \right) + \frac{i}{2} \left(\sum_q b_q^\star E_q^\star E_{q-1} \tilde{c}_a \right) - i\Delta\omega \tilde{c}_b
\end{aligned}$$

From these coupled differential equations we can see that the equations of motion in matrix form is as follows.

$$\frac{\mathrm{d}}{\mathrm{d}t}\begin{bmatrix} \tilde{c}_a \\ \tilde{c}_b \end{bmatrix} = \frac{i}{2}\begin{bmatrix} \sum_q a_q |E_q|^2 & \sum_q b_q E_q E_{q-1}^\star \\ \sum_q b_q^\star E_q^\star E_{q-1} & \sum_q d_q |E_q|^2 - 2\Delta\omega \end{bmatrix}\begin{bmatrix} \tilde{c}_a \\ \tilde{c}_b \end{bmatrix} \tag{A.16}$$

Since

$$i\hbar\frac{\mathrm{d}\psi(t)}{\mathrm{d}t} = H\psi(t) \tag{A.17}$$

we can see that the effective Hamiltonian of the system is

$$H_{eff} = -\frac{\hbar}{2}\begin{bmatrix} \sum_q a_q |E_q|^2 & \sum_q b_q E_q E_{q-1}^\star \\ \sum_q b_q^\star E_q^\star E_{q-1} & \sum_q d_q |E_q|^2 - 2\Delta\omega \end{bmatrix} \tag{A.18}$$

Once again, the assumptions in deriving this H_{eff} are a large single photon detuning, interactions between the medium and the light field are strictly dipolar, and the Raman linewidth is zero.

A.2 Propagation Equations

The propagation of an optical beam through a medium is described by a driven paraxial equation. In free space this would be a homogenous differential equation, but the medium adds an inhomogeneity in the form of the polarizability of the medium:

$$\nabla_\perp^2 E_q - 2ik\frac{\partial E_q}{\partial z} = -\mu_0\omega^2 P_q \tag{A.19}$$

In order to describe the propagation of beams through a Raman medium we must find the polarizability of the medium for each frequency component. In the previous section we found the time dependence of the atomic/molecular wave function. With this information we have an expression for the polarization of the medium in the time domain:

$$P(t) = \langle\psi(t)|\,\hat{P}\,|\psi(t)\rangle \tag{A.20}$$

The general form of the wave function is given by A.5 where the time-dependent behavior of the coefficients c_i is given by A.13 and the polarization operator $\hat{P}$ is

$$\hat{P} = \sum_i \left(\mu_{ai} \ket{a}\bra{i} + \mu_{bi} \ket{b}\bra{i} + \mu_{ia}^{\star} \ket{i}\bra{a} + \mu_{ib}^{\star} \ket{i}\bra{b} \right) \tag{A.21}$$

Combining the expression for c_i with the polarization operator, A.21, we have

$$
\begin{aligned}
P(t) \ = \ & \frac{1}{2\hbar} \sum_q \sum_i E_q \frac{|\mu_{ai}|^2}{(\omega_i - \omega_a) + \omega_q} |c_a|^2 \, \mathrm{e}^{i\omega_q t - ik_q z} \\
+ \ & \frac{1}{2\hbar} \sum_q \sum_i E_q^* \frac{|\mu_{ai}|^2}{(\omega_i - \omega_a) - \omega_q} |c_a|^2 \, \mathrm{e}^{-i\omega_q t + ik_q z} \\
+ \ & \frac{1}{2\hbar} \sum_q \sum_i E_q \frac{|\mu_{bi}|^2}{(\omega_i - \omega_b) + \omega_q} |c_b|^2 \, \mathrm{e}^{i\omega_q t - ik_q z} \\
+ \ & \frac{1}{2\hbar} \sum_q \sum_i E_q^* \frac{|\mu_{bi}|^2}{(\omega_i - \omega_b) - \omega_q} |c_b|^2 \, \mathrm{e}^{-i\omega_q t + ik_q z} \\
+ \ & \frac{1}{2\hbar} \sum_q \sum_i E_q \frac{\mu_{ai}\mu_{bi}^*}{(\omega_i - \omega_b) + \omega_q} c_b c_a^* \mathrm{e}^{i(\omega_q + \omega_a - \omega_b)t - ik_q z} \\
+ \ & \frac{1}{2\hbar} \sum_q \sum_i E_q^* \frac{\mu_{ai}\mu_{bi}^*}{(\omega_i - \omega_b) - \omega_q} c_b c_a^* \mathrm{e}^{-i(\omega_q - \omega_a + \omega_b)t + ik_q z} \\
+ \ & \frac{1}{2\hbar} \sum_q \sum_i E_q \frac{\mu_{ai}^*\mu_{bi}}{(\omega_i - \omega_a) + \omega_q} c_b^* c_a \mathrm{e}^{i(\omega_q - \omega_a + \omega_b)t - ik_q z} \\
+ \ & \frac{1}{2\hbar} \sum_q \sum_i E_q^* \frac{\mu_{ai}^*\mu_{bi}}{(\omega_i - \omega_a) - \omega_q} c_b^* c_a \mathrm{e}^{-i(\omega_q + \omega_a - \omega_b)t + ik_q z} \\
+ \ & c.c.
\end{aligned} \tag{A.22}
$$

Given the definition of a_q, d_q, and b_q and using A.14 to express the exponential terms in terms of the two photon detuning, we can see, after moving some indices, that this time dependent term can be expressed as followed:

$$
\begin{aligned}
P(t) \ = \ & \hbar \sum_q \Big[|c_a|^2 a_q \left(E_q \mathrm{e}^{i\omega_q t - ik_q z} + c.c. \right) \\
+ \ & |c_b|^2 d_q \left(E_q \mathrm{e}^{i\omega_q t - ik_q z} + c.c. \right) \\
+ \ & c_b c_a^* b_{q+1} \left(E_{q+1} \mathrm{e}^{-i\Delta\omega t - ik_m z} \mathrm{e}^{i\omega_q t - ik_q z} + c.c \right) \\
+ \ & c_a c_b^* b_{q1}^* \left(E_{q-1} \mathrm{e}^{i\Delta\omega t + ik_m z} \mathrm{e}^{i\omega_q t - ik_q z} + c.c \right) \Big]
\end{aligned} \tag{A.23}
$$

With this expression for the polarization of the medium as a function of time we can now look at the coupling between frequency components of the driving electric field. Expressing $P(t)$ as follows

$$P(t) = \frac{1}{2} \sum_q \left(P_q e^{i\omega_q t - i k_q z} + c.c. \right) \tag{A.24}$$

we can see that, for a system with an atomic or molecular density, N,

$$
\begin{aligned}
P_q &= 2\hbar N \left(|c_a|^2 a_q E_q + |c_b|^2 d_q E_q \right. \\
&+ c_b c_a^* b_{q+1} E_{q+1} e^{-i\Delta\omega t - i k_m z} \\
&+ \left. c_a c_b^* b_q E_{q-1} e^{i\Delta\omega t + i k_m z} \right)
\end{aligned}
\tag{A.25}
$$

To eliminate the exponential terms in this the expression we make the following transformation

$$
\begin{aligned}
c_a &= \tilde{c}_a \\
c_b &= \tilde{c}_b e^{i\Delta\omega t + i k_m z}
\end{aligned}
\tag{A.26}
$$

and express the polarization in terms of density matrix elements.

$$\rho_{ij} = c_i c_j^* \tag{A.27}$$

Referring back to A.19, we now have a differential equation describing light propagation through a Raman medium.

$$
\begin{aligned}
\nabla_\perp^2 E_q - 2ik\frac{\partial E_q}{\partial z} &= -\mu_0 \omega^2 P_q \\
&= -2\hbar N \mu_0 \omega^2 \left(a_q \rho_{aa} E_q + d_q \rho_{bb} E_q + b_{q+1} \rho_{ab}^* E_{q+1} + b_q \rho_{ab} E_{q-1} \right)
\end{aligned}
\tag{A.28}
$$

Appendix B: Matrix Elements

To calculate the a_q, d_q, and b_q terms we must find the matrix elements coupling the Raman states of the molecules, $|a\rangle$ and $|b\rangle$, to the upper states $|i\rangle$. For deuterium we use the rovibrational states in the Lyman and Werner bands, $B^1\Sigma_u^+ - X^1\Sigma_g^+$ and $C^1\Pi_u - X^1\Sigma_g^+$ respectively as the upper states.

We use the energy level parameters for D_2 found in Herzberg [54] to construct the energy level structure of the molecules. Allison and Dalgarno [60] give the oscillator strengths for transitions to the first 52 vibrational states in the Lyman band and the first 18 vibrational states in the Werner band. With these oscillator strengths in hand we can find the reduced matrix elements for the transitions with the following equation (in atomic units)

$$\langle \chi_{\nu''}^g(R)| D(R) |\chi_{\nu'}^u(R)\rangle = \sqrt{\frac{3f_{\nu''\nu'}}{2G(E_{\nu'} - E_{\nu''})}} \tag{B.1}$$

where D(R) is the dipole moment between the states, ν'' and ν' correspond to the lower and upper vibrational states respectively, $G = 1$ for Lyman transitions and $G = 2$ for Werner transitions, and $f_{\nu''\nu'}$ is the oscillator strength tabulated in Allison and Dalgarno.

The angular portion of the matrix element depends on the polarization of the radiation and can be expressed in terms of Wigner-3j symbols [58]. Equation B.2 is simply multiplied by the reduced matrix element to give the final matrix element.

$$\mathcal{A}_{J'm',Jm} = (-1)^{J'-m'} \sqrt{\max(J, J')} \begin{pmatrix} J' & 1 & J \\ -m' & q & m \end{pmatrix} \tag{B.2}$$

In equation B.2 $q = 0$ for linearly polarized light and $q = \pm 1$ for right or left circularly polarized light. The bottom row of the matrix in B.2 must add to zero and, of course, the transition must obey dipole selection rules:

$$\Delta J = 0, \pm 1 \tag{B.3}$$

$$J = 0 \nrightarrow J = 0 \tag{B.4}$$

$$m' = m + q \tag{B.5}$$

To find the reduced matrix elements for rotational transitions in D_2 we must include Hönl-London factors in our reduced matrix element expression. The reduced matrix elements can be expressed as follows (in SI units) [61]

$$|\langle \nu'', J'' | D | \nu', J' \rangle|^2 = \frac{3}{8\pi^2} \epsilon_0 \hbar \lambda_i^3 H_{J'J'} A_{\nu'\nu''} \tag{B.6}$$

In equation B.6, $H_{J'J'}$ are the Hönl-London factors for the transition (which depend on the initial and final electronic and molecular angular momenta), $A_{\nu'\nu''}$ are the band emission transition probabilities which are tabulated in Allison and Dalgarno [60], and λ_i is the wavelength of the transition.

The Hönl-London factors are different for the P, Q, and R branches of the electronic transition ($J \to J - 1$, $J \to J$, and $J \to J + 1$, respectively). We find that the Hönl-London factors for the P,Q, and R branches are $J'' - 1$, $2J'' + 1$, and $J'' + 2$, respectively for the Lyman band and J'', 0, and $J'' + 1$ for the Werner band [61].

After finding the matrix elements it is simply a matter of summing over all the possible transitions to the Lyman and Werner bands to find the a_q, d_q, and b_q coefficients that contribute to the susceptibility for the field E_q, as shown below. When investigating multiple frequency sidebands we must find a's, d's, and b's for each of those frequencies as well.

$$a_q = \frac{1}{2\hbar^2} \sum_i \left(\frac{|\mu_{ai}|^2}{(\omega_i - \omega_a) - \omega_q} + \frac{|\mu_{ai}|^2}{(\omega_i - \omega_a) + \omega_q} \right)$$

$$d_q = \frac{1}{2\hbar^2} \sum_i \left(\frac{|\mu_{bi}|^2}{(\omega_i - \omega_b) - \omega_q} + \frac{|\mu_{bi}|^2}{(\omega_i - \omega_b) + \omega_q} \right)$$

$$b_q = \frac{1}{2\hbar^2} \sum_i \left(\frac{\mu_{ai}\mu_{bi}^\star}{(\omega_i - \omega_a) - \omega_q} + \frac{\mu_{ai}\mu_{bi}^\star}{(\omega_i - \omega_b) + \omega_q} \right)$$